University of Wollongong

# Research Online

# Simultaneous measurement for material parameters using self-mixing interferometry

Fei Xia
*University of Wollongong*

Follow this and additional works at: https://ro.uow.edu.au/theses1

## Recommended Citation

# Simultaneous measurement for material parameters using self-mixing interferometry

A thesis submitted in fulfilment of the requirements for award of the degree

**Master of Philosophy**

from

**UNIVERSITY OF WOLLONGONG**

by

**Fei Xia**

Supervised by

**A/Prof Yanguang Yu**

School of Electrical, Computer and Telecommunications Engineering

December 2018

*Dedicated to my family*

# *Declaration*

This is to certify the work reported in this thesis was carried out by the author, unless specified otherwise, and that no part of it has been submitted in a thesis to any other university or similar institution.

Fei Xia

December 2018

# *Abstract*

Material related parameters such as Young's modulus and internal friction are important for mechanical and material engineering. These parameters play key roles in the material performances. It has been a great interest to measure the value of these parameters. Traditional methods including tensile test, flexure test, and others are destructive methods often cause damages to specimen and have low accuracy. In recent years, the impulse excitation technique (IET), a non-destructive technique to determine Young's modulus and internal friction of the material has attracted great attention. The detection system used for IET is normally microphone, accelerometer and so on. Self-mixing interferometry (SMI), an emerging sensing technique, which is non-destructive, non-contact, compact structure, and low-cost has been developed for high accuracy sensing applications, such as displacement, velocity and distance measurement and so on is suitable for the material related parameters measurement. A normal SMI system consists of a laser diode (LD) and a target to form the external cavity of the LD. When a portion of the light is reflected or backscattered to the laser cavity, leading to a modulated laser power of LD. This modulated laser power is referred as SMI signal, which carries the information of vibration of the target.

In this thesis, a measurement method combining IET with SMI for material related parameters measurement is proposed. By applying wavelet transform onto the SMI signal, both resonant frequency and damping factor of the specimen vibration can be retrieved at the same time. Therefore, both Young's modulus and internal friction of the specimen can be calculated simultaneously. The optical fibre is introduced to the system. With the installation of the optical fibre, the flexibility of the measurement is greatly improved. The measurement results show the feasibility for simultaneous measurement of material related parameters. A graphical user interface is designed to improve the user experience for the measurement.

# *Acronyms*

| | |
|---|---|
| **SMI** | Self-mixing interferometry |
| **PD** | Photodiode |
| **LD** | Laser diode |
| **CWT** | Continuous wavelet transform |
| **IET** | Impulse excitation technique |

# *Acknowledgement*

I would like to extend thanks to all the people who have been involved with and generously contributed to the work presented in this thesis.

First and foremost, I would like to express my sincere gratitude and respect to my supervisor, Associate Professor Yanguang Yu, Doctor Ginu Rajan, and Professor Jiangtao Xi, for their encouragement and guidance. Without their enlightened instruction, impressive kindness and patience, I could not have completed my thesis. Their keen and vigorous academic observation enlightened me not only during this thesis but for my future study and career.

Secondly, I extend my thanks to the staff in the School of Electrical, Computer and Telecommunications Engineering (SECTE) who have helped me to develop a fundamental and essential academic competence. My sincere appreciation also goes to the teachers and students from the Signal Processing for Instrumentation and Communications Research (SPICR) Lab, who participated in this study with enthusiastic cooperation.

Last but not least, my special thanks go to my parents, my girlfriend and her family, for their generous and loving support. With their unbelievable trust and encouragement, I can finally finish this work. I dedicate this thesis to them as the most important people in my life.

# *Publications*

1.  F. Xia, Y. Ruan, Y. Yu, Q. Guo, J. Xi, and J. Tong, "Retrieve the material related parameters from a self-mixing signal using wavelet transform," *2018 IEEE International Frequency Control Symposium: Sensors and Transducers, California, USA,* May 2018.

2.  F. Xia, B. Liu, L. Cao, Y. Yu, Q. Guo, J. Xi, and J. Tong, "Experimental study on simultaneously measuring Young's modulus and internal fraction using self-mixing system," *The International Society for Optics and Photonics: Semiconductor Lasers and Applications VIII, Beijing, China,* October 2018.

# TABLE OF CONTENTS

# LIST OF FIGURES

**LIST OF TABLES**

# Chapter 1    Introduction

## 1.1    Introduction to material related parameters

Material related parameters such as Young's modulus, damping and internal friction are fundamental parameters for the engineering and application of materials. They are inherent characteristics that depend on the composition, processing, microstructure and damage suffered by the material [1, 2]. Young's modulus，named for the 18th-century physician and physicist Thomas Young, is a numerical constant which describes the elastic properties of a solid undergoing tension or compression in only one direction. It is a measure of the ability of a material to resist deformations in length when undergoing longitudinal tension or compression. It is equal to the longitudinal stress divided by the strain. For example, in Figure 1.1, $A$ is the cross-sectional area of a metal bar pulled by a force $F$ at each end. The bar stretches from its original length $L_0$ to a new length $L_n$. The stress equals to the force divided by the cross-sectional area, i.e. $F/A$. The strain or relative deformation equals to the change in length divided by the original length, i.e. $(L_n - L_0)/L_0$. Young's modulus $E$ can be stated as the stress divided by the strain, i.e.

$$E = \frac{FL_0}{A(L_n - L_0)} \tag{1.1}$$

The units of Young's modulus in the English system are pounds per square in inch (psi), and in the metric system are Newtons per square metre $N/m^2$.
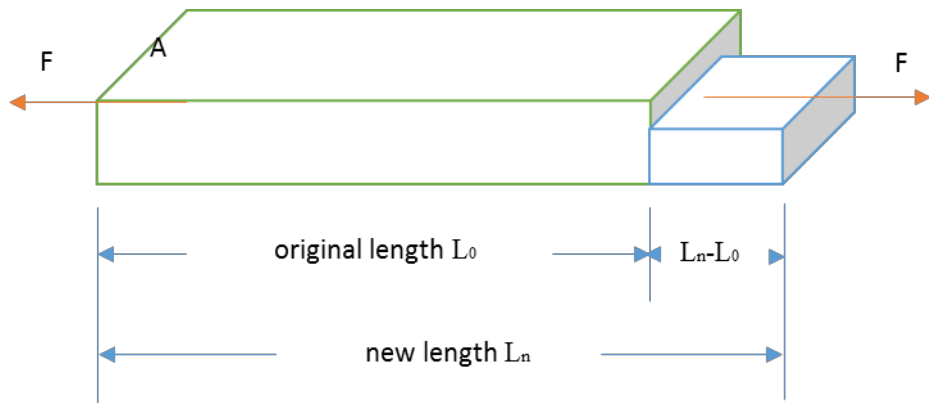
Figure 1.1. Metal bar under tension increases in length and decreases in cross sectional area [3]

Damping or internal friction is the phenomenon by which mechanical energy is dissipated in a system. It determines the vibration amplitude at resonance and the vibration persistence time after interruption of the excitation [4]. Figure 1.2 shows the vibration of a damped harmonic oscillator after interruption of the excitation.
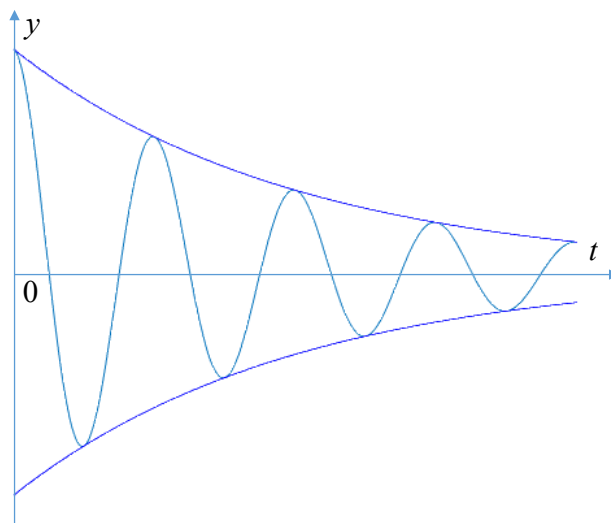


Figure 1.2. Damping vibration of a harmonic oscillator after interruption of excitation.

Both Young's modulus and damping are important parameters for analysing material performance. Many materials such as metals and alloys [5, 6], concrete and cementitious

[7, 8], and ceramics and refractories [9, 10] are subjected to forces and stresses when in service. In these situations, it is necessary to know the Young's modulus to meet the design requirements. The damping also plays a vital role in these designs, where damping is associated with defects in granularity and impurities of materials [11, 12] and thermoelastic effects caused by local gradients of temperature [13, 14]. By knowing the Young's modulus and damping, the deformation can be predicted and the cracks can be monitored, which will be significantly useful to prevent fatigue and fracture.

Knowing the values of these parameters is highly desired in the engineering field for different applications. The measurement of Young's modulus and damping has attracted of many researchers and many laboratory experiments have been conducted according to conditions of specific materials and environments.

### 1.1.1  Measurements of Young's modulus

This section reviews different measurement methods for Young's modulus. For the Young's modulus measurements, it can be categorized into two different types based on the measurement effect on the specimen: destructive methods and non-destructive methods. Destructive methods are often conducted based on the direct measurement of stresses and strains of a specimen loaded by a known force. The measurement can only be conducted once on every specimen. Non-destructive methods often investigate the materials parameters in the frequency domain, where the system is simpler than the traditional destructive methods and can achieve higher accuracy. More importantly, the non-destructive methods have much less impact on the specimen compared to the destructive methods. This is important to achieve repeatability to compare the results from the same specimen.

●   Destructive methods

Tensile test is one of the destructive methods of measuring Young's modulus [15, 16]. Figure 1.3 shows the schematic of a typical tensile test with a specimen. For the tensile test, the specimen has two shoulders with a gauge section in the middle (as shown in Figure 1.3). The test is conducted with one end of the specimen clipped by the holding

grips at the bottom and the other end held by the holding grips attached with a load cell. By moving the crosshead, a force will be applied to the specimen, and then the gauge section will be lengthened. The Young's modulus can be measured with the relation of this force and the lengthened length.
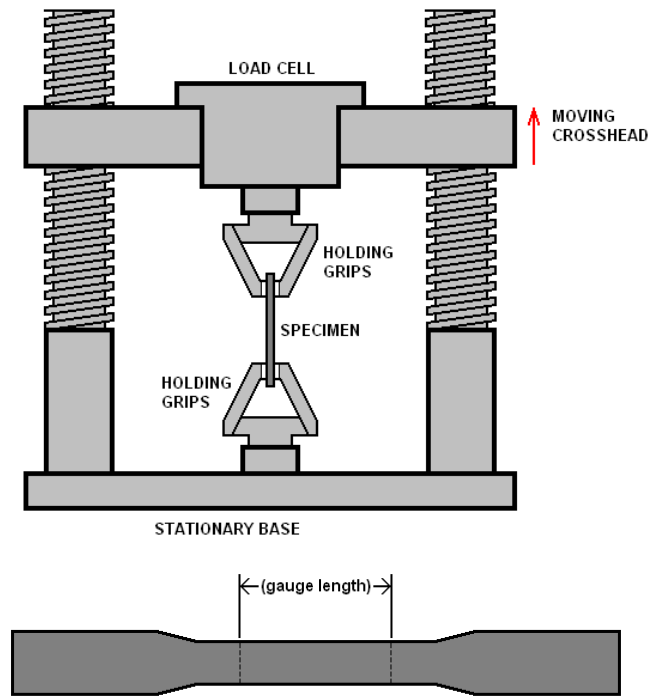


Figure 1.3. Schematic of typical tensile test and the specimen [17]

The results of tensile test come to a figure of stress-strain curve where the slope indicates the value of Young's modulus. Figure 1.4 shows the stress-strain curves of aluminium and steel materials [18]. It can be seen that the slope of stress-strain changes to a nonlinear curve at a certain point. This nonlinear curve directly influences the accuracy of Young's modulus, which may cause significant error in the measurement. In some other cases, this impact may be greater depending on the different types of materials [19].Many international standards such as ASTM international  (ASTM) and European Standard (EN) have developed a large number of standards based on tensile test. They have developed a completed tensile test system and results.

Tensile test has been accepted as a standard way to obtain Young's modulus. However, the disadvantage of tensile test is very obvious such as the design requirement of the

specimen and the low accuracy in the measurement.
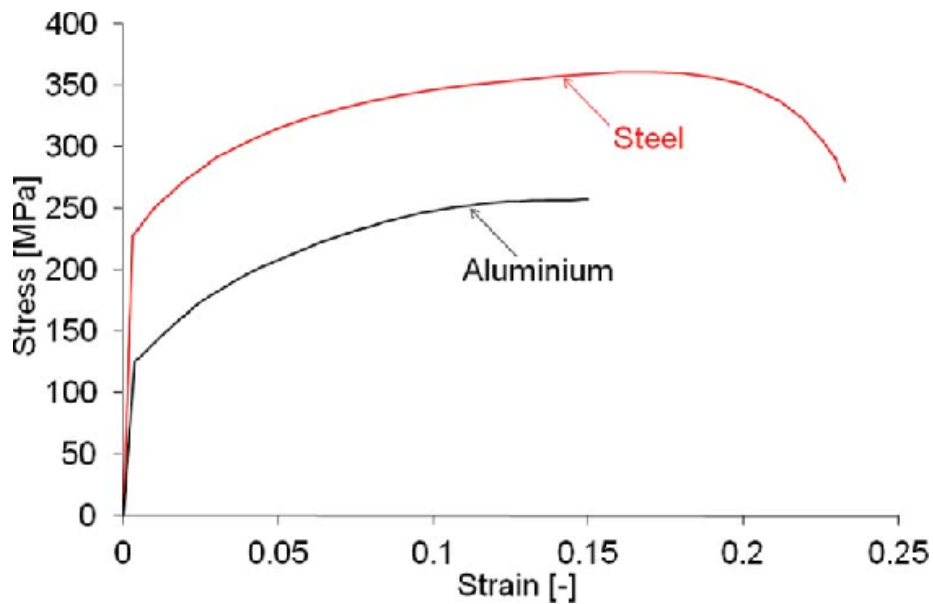


Figure 1.4. Stress-strain curves of aluminium and steel materials [18]

Apart from tensile test, there are also other destructive methods of measuring Young's modulus measurements are destructive that have been widely used by engineers and testers. One of them is flexural test also known as three-point or four-point bending flexural tests. The difference between flexural test and tensile test is the way of loading forces on the specimen. Figure 1.5 shows a schematic of a typical three-point bending flexural test. The test usually involves a specified test fixture on a universal testing machine with a specimen placed on two supporting pins a set distance apart. A force is applied on the specimen through the loading pin, and then the specimen is bent in the shape of a 'v'. The Young's modulus is determined from the slope of the stress-strain curve produced by the test. Depending on the material requirements, the flexural test can also be conducted in different ways such as biaxial flexural test for ceramics [20].

The results of flexural test not only can determine the Young's modulus but also can determine the flexural modulus, which is an advantage compared to the tensile test [21]. However, this method also has some disadvantage, as the system need to be designed properly, and the results are sensitive to specimen surface and loading geometry [22].
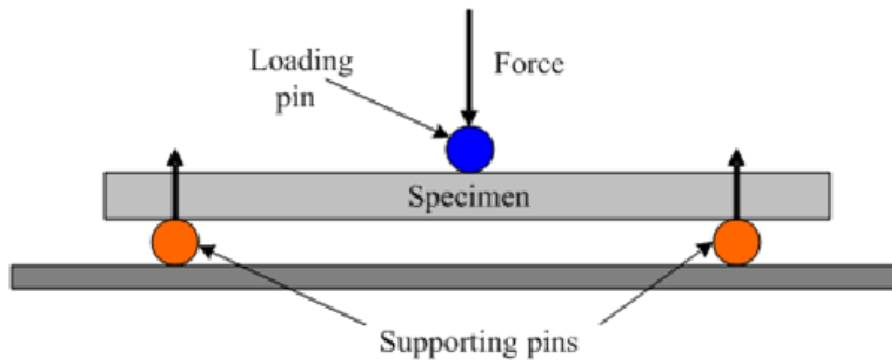
Figure 1.5. Schematic of typical three-point bending flexural test [23].

Test methods such as tensile test and flexural test are feasible for relatively large specimen, but when it comes to small specimens typically in nanoscale these methods are no longer applicable. The indentation test, another destructive method, is more suitable for these relatively small specimens [24, 25]. Figure 1.6 shows the schematic of nano-indentation test. Young's modulus is measured through the relation between the depth of penetration and the applied force from the indenter. However, the indentation test has disadvantages compared to other methods like tensile test and flexural test, where the indentation test is more time consuming and data analysis is not straightforward.
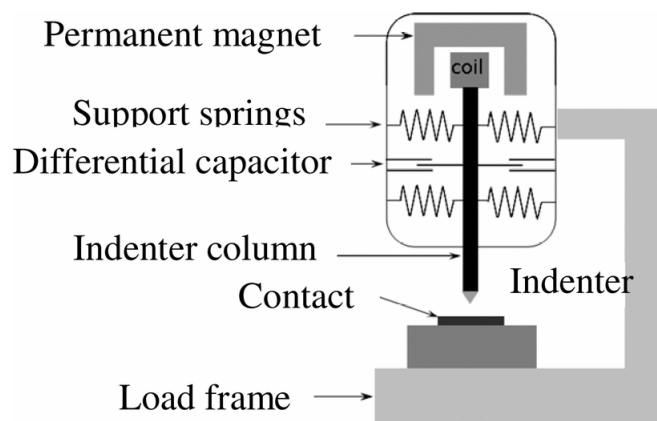


Figure 1.6. Schematic of nano-indentation system with sensing systems [26].

In summary, these destructive methods for measuring Young's modulus are well accepted by researchers. However, the disadvantages of these methods are obvious,

which include complicated system and specimen design, results with low accuracy, unsuitable with extreme environment and destructive measurements with no repeatability. There comes the drive to develop a better way for Young's modulus measurement. Non-destructive methods attract more and more researchers for Young's modulus measurement, due to their simple system design, fast implementation, and more importantly, they are non-destructive which makes the test repeatable.

- Non-destructive methods

Compared with destructive methods, non-destructive methods often show high accuracy for Young's modulus measurement due to their simple system and specimen design [27]. Unlike destructive methods, non-destructive methods do not involve stress-strain relation, and instead they measure the fundamental frequencies of the specimen through resonance or excitation. The most commonly used non-destructive methods for metals are resonance and impulse excitation techniques (IET), and other non-destructive methods such as ultrasonic, wave propagation, electronic or optical methods are also used depending on the materials used.

Resonance methods measure the fundamental resonant frequency of the specimen with a suitable geometry. Using an impulse tool to strike the specimen, the specimen is excited into vibration. An external transducer such as an accelerometer or microphone can pick up this vibration signal and transform it into an electrical signal[28]. The fundamental resonant frequency can be retrieved by analysing the signal, then with the dimensions and mass of the specimen the Young's modulus of the specimen can be calculated. The resonance method is especially suitable for materials that are elastic, homogenous and isotropic [29].

There are different ways to induce excitation for the resonance method. In 1992 L. Kiesewetter used the resonance method to measure the Young's modulus of a microcantilever thin films [30]. He applied three different excitation ways: photo-thermal excitation using laser beams, acoustic excitation using loudspeaker and mechanical excitation using a piezo-transducer. Figure 1.7 shows the three different excitation ways.
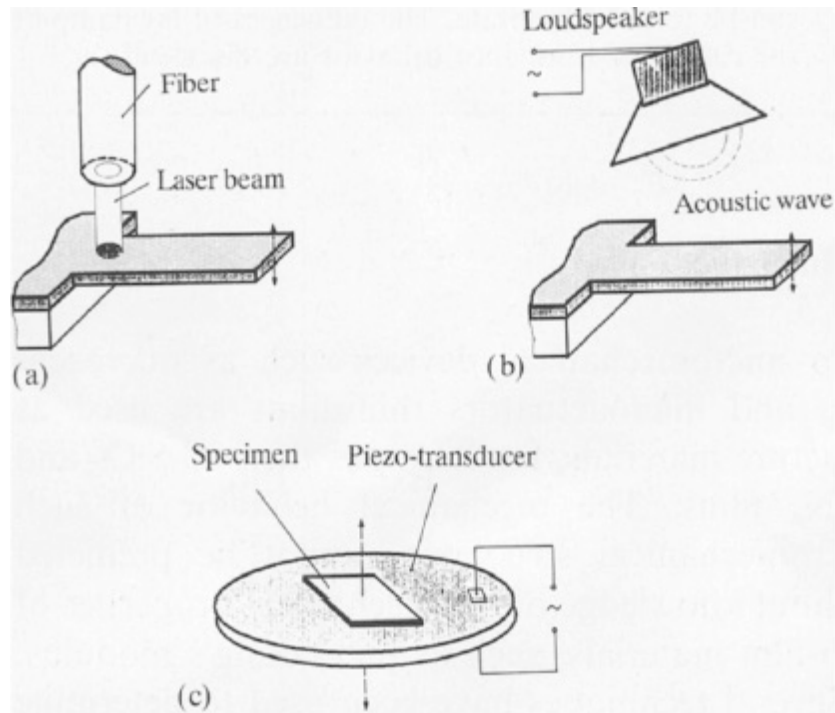
Figure 1.7. Three ways to excite microresonantors (a) photothermal, (b) acoustic, (c) mechanical [30]

For the photothermal excitation process, a laser diode is used. The laser beams travel through the fibre and then point vertically onto the cantilever. The laser beam energy is partially absorbed by the surface of the cantilever. As the thermal waves propagate, temperature differences are created, causing localized strains due to thermal expansion. A time-dependent temperature field was produced if the intensity of the laser beam is modified, so that the cantilever is driven into vibration. For acoustic excitation, a small loudspeaker is used to generate acoustic waves. The waves propagate through the air to the cantilevers, producing pressure differences around the structure and forcing the cantilever to vibrate. For mechanical excitation, a piezotransducer is used. The test thin film is carefully attached with an adhesive to the circular piezotransducer. The thin film is excited by the power of piezotransducer. The excitation ways are used by researchers can be summarized within these three ways.

a) Photothermal excitation

Ramos [31] measured the frequency response of commercial silicon nitride

microcantilevers in liquid using photothermal excitation. The exciting laser used in this setup focused on the bottom of the microcantilever where the detection laser targeted the top of the microcantilever. By using the optical beam deflection technique, the resonant frequency of the cantilever was measured. The optical beam deflection technique was also used by Pini [32], where he measured the vibration mode of silicon microcantilever excited by optical thermal effect in the air environment. Nishida [33] used laser Doppler velocimetry to measure the velocity amplitude of vibration mode to reflect flat frequency characteristics of the silicon microcantilevers. He used the exciting laser to excite the specimen in liquid environment. Yoshinaka [34] used an optomechanical heterodyne detection to analyse the vibration signal. This detection method has also been used in another thermal excitation test by Song [35] to measure the resonant frequency of semiconductor cantilevers. Bircher [36] conducted the experiment of using photothermal excitation to measure a silicon cantilever. To summarise, the thermal excitation method is currently available for micrometer scale and cantilever measurement. The detection methods mentioned in the above tests all have some limitations, such as the optical beam deflection technique. The sensitivity of optical beam deflection technique depends on several factors [37, 38], such as the difference of the optical path length introduced by the cantilever displacement, the total captured rays from various points of the cantilever and the angle of incidence. These limitations potentially affect the accuracy of the measurement. The other detection systems, such as optomechanical heterodyne detection and laser Doppler velocimetry, are relatively complicated.

b) Acoustic excitation

Reddy [39] used the acoustic excitation method to excite the sample and measure the frequency response. A viscoelastic, made from polyvinyl chloride of 1mm thickness was used as the test sample. The viscoelastic polymers exhibit high material loss factors in the frequency and temperature ranges of practical interest which can be used in damping treatment to control excessive vibration and noise in structures. In the experiment, an exponential horn producing plane sound waves, was directed on to the test sample to induce for acoustic excitation. A condenser microphone was used to record the data for

analysis. Zhang [2] calculated the Young's modulus of the boron doped silicon which is important for designing resonators and other micromechanical devices. An acoustic excitation method was used to drive the microstructural sample to vibrate where an acoustic transducer driven by PZT transducer was targeted at the silicon resonator from a few centimetres away. An optical heterodyne interferometer was used to detect the vibration. Kemps [40] measured the Young's modulus of eggshell by using resonant frequency method, which was with the dimensions of 350μm thickness, 26mm length and 10mm width. The tested eggshell was excited by a broad range loudspeaker, where the acoustic energy through air excited the eggshell into natural vibration mode. A laser vibrometer was placed above the eggshell to measure the velocity of the vibration. Ricci [41] measured the resonant frequency and Young's modulus of microscale structures by using acoustic excitation method. The test sample was microcantilever beams and microscale rotational oscillators with micrometre scale, which were excited into vibration mode by an air-couple transducer. The displacement was measured by Laser Doppler vibrometer, which was then used to calculate the resonant frequency of the test sample. Apart from normal acoustic excitation, the ultrasonic excitation has also been used for resonant frequency related measurement. Bamber [42] measured the relationship between Young's modulus and Poisson's ratio of fused silica by using the acoustic microscopy which generated the ultrasonic wave as a probe. Fatemi [43] used resonant frequency method based on ultrasound excitation to measure the Young's modulus of aluminium alloy rod. The test sample had the dimensions of 6cm length and 9mm diameter. The rod was placed in water and the ultrasound energy emitted from ultrasound-stimulated vibro-acoustic spectrography was converted into vibrational energy in the rod through water. A submerged audio hydrophone placed in the water was used as the detection device in the experiment. An innovative method of using a contact ultrasonic excitation method was used for determining the Young's modulus of drug tablet [44]. In 2017 Ma [45] used a combined resonant ultrasound spectroscopy to determine the elastic modulus of capsules.

The acoustic excitation has been used to excite small samples from a range of

millimetre scales. The specimen can also be different materials such as viscoelastic materials, eggshell, metal, drug tablets etc. It can be seen that acoustic as well as ultrasonic excitation has potential values to be used for the measurement of material related parameters.

c) Mechanical excitation

There are different forms of mechanical excitation depending on the supporting ways and exciters such as electrostatic force and electrodynamic shaker. Ye [46] applied an electrostatic force to a silicon cantilever plate, with two opposite edges clamped and other two edges are free to measure its Young's modulus. He used an incident laser beam to detect the vibration and a position-sensitive-detector to receive it. Caracciolo [47] measured the Young's modulus of viscoelastic material in different temperatures. The viscoelastic material is a mixture of polypropylene and calcium carbonate. The material was designed as a cantilever beam with the fixed end glued to the support. The support was excited by an electrodynamic shaker so the cantilever beam was excited into vibration mode. An emitter-receiver laser sensor was used to measure the displacement of the cantilever beam in order to measure the Young's modulus. Guillot [48] measured the Young's modulus of highly compliant elastomers at elevated hydrostatic pressure. The neoprene specimen was glued to a vibration-transmitting metal rod, which is glued to a ten piezoelectric ceramic discs shaker. The Laser Doppler vibrometer sensor was used to measure the vibration of the sample. The mechanical excitation has been applied to a different materials of a broad range of sizes. This is due to its ability to excite the sample by a contacting way, so even the relatively large scale of sample can be excited as well

It can be summarised that for measuring the elastic modulus of microstructures such as silicon cantilever and carbon nanotube in liquid environments, thermal excitation is better than mechanical excitation due to the merits of non-contact and non-destructive. It is noticed that in order to make the microstructure to absorb the most heat from laser a layer of gold coatings is needed. The thickness of the coating layer can be up to 9.4% [31] of the total thickness of the microstructure. Acoustic excitation is normally applied to thin film structures such as microstructures, thin viscoelastic polymers and eggshell, while

ultrasonic excitation is more suitable to larger scales. However, the accuracy can be affected by the impact from ultrasonic to the surrounding structures[43]. Although the mechanical excitation method has the intrinsic demerit of contacting, it is currently a good way for measuring the size of objects from millimetre to centimetre.

More recently, impulse excitation techniques (IET) one of the non-destructive methods for measuring material related parameters, based on the equivalent principle of resonance method, is more attractive to researchers in material engineering fields[49, 50]. Instead of driving the specimen by an external exciter, this technique uses a singular elastic strike with an impulse tool to strike the specimen and the specimen will be excited into vibration. The Young's modulus can be measured by analysing the recorded signal from sound or optical spectrum[51]. Suansuwan [5] used IET to measure the Young's modulus of metal alloys and dental porcelains. The specimens were all cast into rectangular shape. The specimen is placed on a soft foam with free-free beam mode. An impulser with a steel sphere struck on the middle of the specimen excited the sample into vibration. An acoustic microphone was used to catch the vibration signal in order to measure the Young's modulus. The IET has also been widely used for measuring Young's modulus in different materials. Tognana [50] used IET to measure the Young's modulus of epoxy matrix particulate composites in a proportion 100:90:0.7 in weight. A small polymer ball was used as the impulser to strike the specimen. A microphone was used to detect the vibration. Bahr [52] used IET to measure the Young's modulus of normal-weight siliceous concrete. The specimen was supported in two points and tapped with an automated tapping device in the antinode point. A microphone was used to capture the vibration signal and analyse it using resonance frequency and damping analyser (RFDA) software. Montecinos [53] used IET to measure the Young's modulus of CuAlBe alloys influenced by different thermal treatments. The specimen was placed on the two sharp edges support, then a small polymer ball was used to hit the centre of the specimen. A commercial microphone was used to detect the vibration of the sample in order to calculate the Young's modulus. Slim [54] applied IET by using the resonance frequency and damping analyser to measure the Young's modulus of tungsten films.

Researchers have also used other non-destructive methods such as ultrasonic, wave propagation, electronic or optical methods for Young's modulus measurement. For example, the laser-generated surface acoustic wave technology and signal collected from the surface provide information for Young's modulus calculation [55-57].

## 1.1.2 Measurement of damping and internal friction

Damping describes the decay oscillation after a disturbance in a system. In the material engineering, damping is the energy dissipation parameter of a material under cyclical stress. It converts the mechanical energy into thermal energy. The level of damping is determined by the absorbed energy per cycle in the structure [58]. A perfectly elastic material subject to cyclical stress will oscillate without loss of energy, except by external friction with its support and with the atmosphere or surrounding fluid. In reality, vibrations are dampened more rapidly than in the case of energy loss due solely to external friction. The phenomenon of damping in the material often refers to the internal friction defined as the dissipation of mechanical energy inside a gaseous, liquid or solid medium. In a solid material exposed to a time-dependent load within the elastic deformation range, internal friction usually means energy dissipation connected with derivations from Hooke's law, as manifested by some stress–strain hysteresis in the case of cyclic loading [4]. The determination of internal friction in materials is important, where the fact that the internal friction in homogenous materials is independent of the geometry of the solid. This means that internal friction is a useful parameter for evaluating material performance.

The measurement of internal friction has attracted many researchers because of its importance in engineering application. The experimental methods for internal friction can be divided into four groups: quasi-static method, sub-resonance method, resonance method and wave propagation method. The quasi-static method is the conventional testing method for internal friction measurement. It measures the changes of loops of stress-strain. Figure 1.8 shows the schematic of using strain gauges for internal friction

measurement.
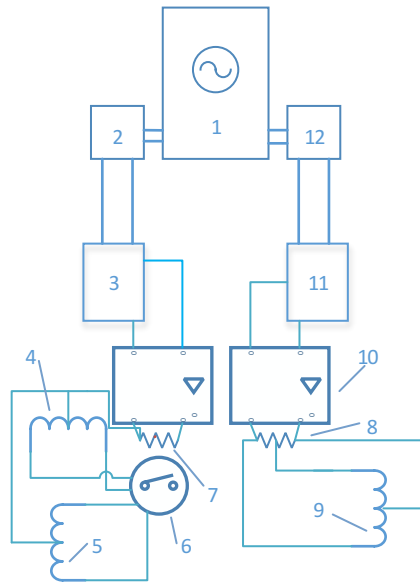


Figure 1.8. Diagram for measuring internal friction using strain gauges: 1) oscilloscope; 2,12) frequency-selective filters; 3) amplifier; 4,5,9) strain gauges; 6) switch; 7,8) resistors; 10) two-channel amplifier of strain gauge data; 11) compensator of the phase shift of the signal [59].

The principle of the measurement is that the sensor 4 is attached to the specimen and sensors 5 and 9 are attached to the dynamometer. The deformation of the specimen is measured from the proportional relationship with the signal from sensor 4. The signal from sensor 9 passes through the strain gauge is proportional to the stress. The beam of the electrons on the screen of the oscilloscope describes the loop in the stress-strain coordinate. This method can measure the material with internal friction larger than 0.001 with the error no greater than 10%. The accuracy of this measurement system very much depends on the effective connection of the amplifier, which subtract the elastic strain from the total strain of the specimen to increase the sensitivity of the system.

The sub-resonance method is often performed by the forced torsion pendulum system. This system is suitable for low-frequency range and shows high efficiency depending on the stain amplitude and temperature.  The torsional pendulum system has many different

versions. Figure 1.9 shows the typical torsional pendulum system [60, 61]. The internal friction is measured with a detector. The torque is generated by the effect of the magnetic field of coils from the permanent magnet. This measurement method shows good results compare to the strain gauge system.
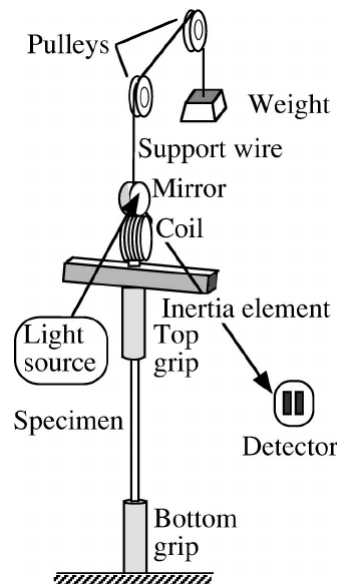


Figure 1.9. Torsional pendulum system. The magnetic field from the permanent magnet upon the coil generates the torque on the specimen [61]

Resonance method is most widely used compare to other methods. Internal friction can be determined from resonance method in different ways. One way is to determine the elastic stored energy in one cycle and the corresponding energy absorption during that cycle by a careful analysis of the relative magnitude of the input and output signals of the stationary resonance vibration. This usually needs high stabilisation and calibration effort. The resonant bandwidth method and free decay method (logarithmic decrement method) are more often used [62, 63]. The resonant bandwidth method is based in the magnitude curve of the frequency-response function by using forced vibrations with constant excitation. The bandwidth is defined as the width of the frequency response magnitude curve when the magnitude is $1/\sqrt{2}$ times the peak value. The damping ratio can be

determined from the bandwidth [64]. The free decay method is simply to measure the rate of decay of free vibration after removing the excitation. There are different ways of determining the rate of decay depending on the damping level of the sample, the quality of the signal and the data processing. The internal friction can be calculated when the rate of decay is determined.

The wave propagation method is based on the pulsed excitation. The pulse from the high frequency generator with frequency corresponding to the resonance frequency of a plate on the transducer induces vibration in the specimen. The vibration is transferred through a thin transition layer to the specimen forms a moving ultrasound wave. The ultrasound wave will be reflected many times between the two sides of the specimen until the complete attenuation of the vibration. The transducer is used to determine the time of the attenuation. The internal friction is determined by analysing the amplitude of the echo signals synchronised on the oscilloscope [59]. To meet the measurement requirement for some special specimen, there are also other combined techniques such as acoustic coupling [65], miniaturised resonators [66]and complex-shaped oscillators [67]have been explored by researchers.

A short summary of different measurement methods for Young's modulus and internal friction is shown in Table 1.1. Researchers and engineers have been continuously improving the measurement methods for Young's modulus and internal friction. Developed from static or quasi-static methods to dynamic methods such as resonance and wave-propagation method. These improvements solve the problems with traditional methods such as the high requirement of specimen design, inadequate testing environment and destructed specimen in the measurement. For the high efficiency of measurement of material related parameters, it comes to mind that to develop a measurement system to measure both Young's modulus and internal friction at the same time.

Table 1.1. Brief summary of Young's modulus and internal friction measurement

| Material parameters | Classification | | Methods | Principle |
|---|---|---|---|---|
| **Young's modulus** | Destructive | | Tensile test [15, 16] | Strain-stress curve |
| | | | Flexural test [20] | |
| | | | Indentation test [24, 25] | |
| | Non-destructive | Resonance | Photothermal excitation [31] | Resonant frequency |
| | | | Acoustic excitation [39] | |
| | | | Mechanical excitation [46] | |
| | | IET | Impulse excitation [50] | |
| **Internal friction** | Quasi-static | | Strain gauge test [59] | Strain energy scattering |
| | Sub-resonance | | Torsional pendulum test [60] | |
| | Resonance | | Forced vibration [62] | Half bandwidth or Logarithmic decrement |
| | Wave-propagation | | High frequency pulse excitation [67] | Wave attenuation |

Numerous researches have been conducted on measuring Young's modulus and internal friction separately. It drives researchers' attention for measuring both Young's modulus and internal friction at the same time. The measurement methods need to be chosen wisely. For example, the destructive methods for Young's modulus measurement are not suitable for internal friction measurement. The non-destructive method, which is based on the resonant frequency, is a good option for measuring both Young's modulus and internal friction. Based on the different mechanism, the supporting system can also categorised as cantilever or free-free typesBarmatz [68] measured the Young's modulus and internal friction with the cantilever beam with the temperature range from 1.5K to 300K. Teruaki [69] measured Young's modulus and internal friction of wood for musical instruments by a flexural vibration from free-free beam mode. The Young's modulus is calculated from the resonant frequency and the internal friction is calculated from the damping of the vibration. The frequency range of measurements is restricted within 250Hz and 700Hz. Zheng [70] utilised the cantilever beam mode to measure the Young's modulus and damping ratio of wood-based composites. Owning to the non-destructive, fast and easy set-up features, IET have been adopted by researchers for both Young's modulus and internal friction measurement. Research companies and groups such as Sonelastic, BuzzMac International and KU Leuven have been using IET to measure both the Young's modulus and internal friction. Besides the convenience of using IET, the detection of the vibrating signal plays a key role for the measurement. Without proper detection of the signal, it is impossible to retrieve the information related to the Young's modulus and internal friction. The detection tool such as microphone, which in some situations causes variations on the results. For IET based methods, one of the key points is to detect the vibration signal from the specimen. In this thesis, a detection method of using self-mixing interferometry technique is proposed.

## 1.2 Introduction to self-mixing interferometry

Laser self-mixing interferometry (SMI) is an emerging technique in recent decades. A

normal SMI consists of a laser diode (LD) and a target to form the external cavity of the LD. When a beam of laser light is focused on a remote moving target through a collimating lens, a portion of the light is reflected or backscattered to the laser cavity and detected by an integrated photodiode (PD) at the rear of the LD [71]. The reflected or backscattered light, also known as the optical feedback, leads to a modulation in both the amplitude and the frequency of the lasing field. This phenomenon is called the self-mixing effect, from which SMI was developed. Initially, this optical feedback or effect was treated as disturbance, while currently owing to the non-contact feature of this physical phenomenon, low-cost commercial LD have been designed for high accuracy sensing applications such as displacement measurement [72-74], absolute distance [75-77], velocity [78-80], vibration [81-83] as well as laser related parameters [84-87] and so on. A typical schematic diagram of SMI system is shown in Figure 1.10.
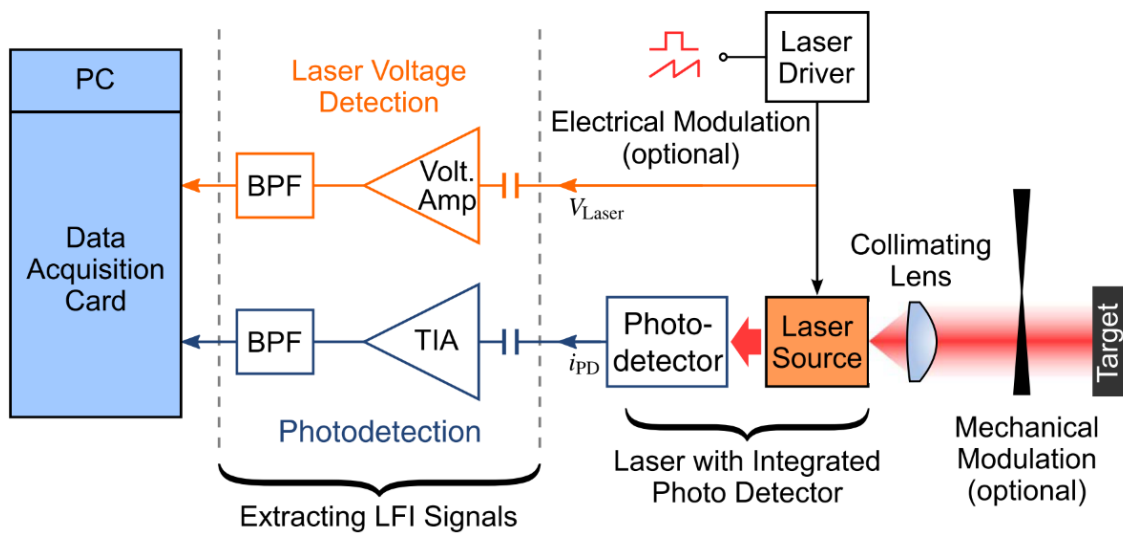


Figure 1.10. Schematic diagram of the basic SMI system. The laser driver controls the laser current through electrical modulation. A portion of light reflected from the target passes through the mechanical modulation. Interferometric signals are acquired using a data acquisition card (DAQ) connected to a computer (PC) through PD together with a trans-impedance amplifier (TIA), followed by a bandpass filter (BPF) [88]

A conventional SMI system configuration is shown in Figure 1.11. It is equivalent to the

three-mirror cavity model, where $P_r = P_0/A$ is the power back-reflected by the remote target. $P_0$ is the original emitted power and $A > 1$ as the attenuation of the external cavity.
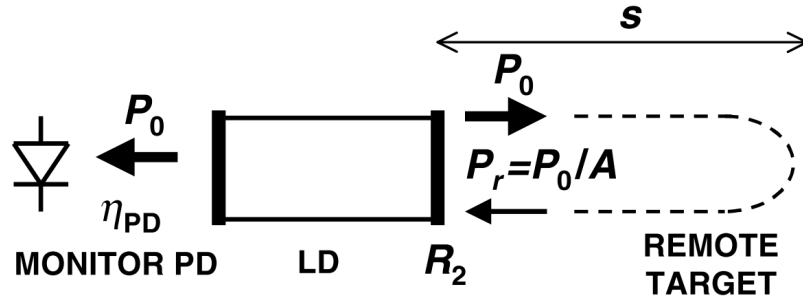


Figure 1.11. Conventional SMI system using a LD [73].

The injection-detection can be interpreted as following [89]: the small back-reflected field phasor $E_r$ re-enters the laser cavity and it adds to the lasing field phasor $E_0$. The phase of $E_r$ is $\phi(t) = 2ks(t)$, where $k = 2\pi/\lambda$ ($\lambda$ is the wavelength of the laser) and $s(t)$ is the distance of the remote target. Hence, the lasing field amplitude and frequency are modulated by the term $\phi = 2ks$. Thus the amplitude modulation is $\sin(2ks)$ and the amplitude modulation is $\cos(2ks)$. The detection scheme very closely resembles the well-known homodying radio frequencies. From the quadrature signals, the interferometric phase $\phi = 2ks$ can be retrieved without ambiguity which makes it possible for target displacement measurement [90].

As it is mentioned, SMI technique has been applied for high accuracy sensing application. Perhaps the simplest application for external-cavity-related measurement is the displacement measurement. It is conducted by changing the external cavity length. This application has been used for measuring defect detection and profilometry [91, 92], more recently it is developed for high-resolution micro-displacement measurement [93]. Figure 1.12 shows experimental external target displacement and the corresponding SMI signals with different feedback level $C$. The displacement measurement method first developed

in 1995 [74], a fringe counting method. It is based on the fact that each fringe on an SMI signal corresponds to a half-wavelength shift of the external target. This fringe counting method is simple but with low resolution. Other methods such as phase unwrapping method [106] Fourier transform method [72], linear interpolation method [94] *etc.*, are developed to improve the measurement accuracy [95].
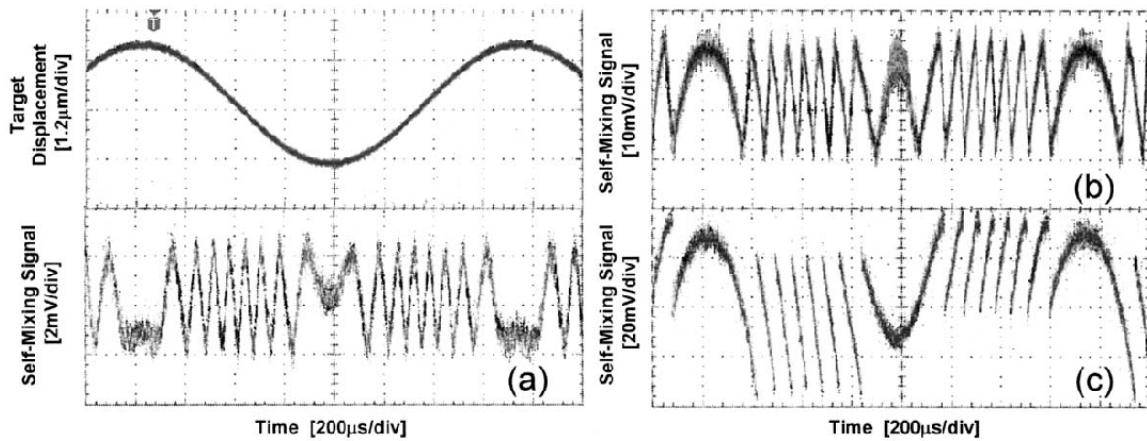


Figure 1.12. Experimental SMI signals obtained from different optical attenuation parameter corresponding to external target displacement. Upper left trace: loudspeaker drive signal at 657Hz, 1.2μm/div. (a) $A \approx 2 \times 10^8$, $C << 1$; (b) $A \approx 8 \times 10^6$, $C \approx 1$ ;(c) $A \approx 4 \times 10^5$, $C > 1$. Where $C$ is the feedback level [73].

Apart from the displacement measurement application, other applications like velocity measurement [78-80], vibration measurement [81-83], linewidth enhancement factor measurement [85,86] and so on are also well developed. Comparing with other measurement method, SMI based technique has the following advantages:
  (1) Non-contact measurement resulting in non-destruction for the specimen
  (2) No external detector needed, leading to a simple and compact set-up
  (3) High sensitivity of the scheme
  (4) Using small specimens to reduce the total cost of the experiment
Due to the superior advantages of SMI technique, this thesis proposes to use this optical

method to establish a compact physical system with low cost. The vibration from the specimen can be detected by the SMI system, from which the Young's modulus and internal friction can be determined.

## 1.3    Existing problems and objectives

Given the literature review above, the outstanding issues of measuring Young's modulus and internal friction can be summarised as following:

➢ The traditional methods of Young's modulus measurement are destructive. Among the non-destructive methods, the detector design is complicated with big size.

➢ The existing internal friction measurement has low measurement accuracy. There is a need for developing a method with high accuracy and repeatable measurement.

➢ It is desired to design a non-destructive measurement system with compact structure, low-cost and high sensitivity.

Hence, this thesis proposes to use SMI technique to achieve non-destructive measurements on Young's modulus, and internal friction simultaneously.

## 1.4    Research contributions

➢ A new method of using SMI for simultaneous measurements of material related parameters is developed. In contrast to the traditional methods such as tensile test and torsion pendulum test for Young's modulus and internal friction measurements, the proposed SMI based method is non-destructive and non-contact with high accuracy. By applying wavelet transform onto the SMI signal, the material related parameters such as resonant frequency and damping factor can be retrieved at the same time, so that to achieve the measurements of Young's modulus and internal friction of the specimen.

➢ An optical fibre coupled SMI measurement system is designed. The optical fibre is installed in the system with a fibre polarization controller to control the polarization state of the light. By installing optical fibre in the SMI system, the flexibility of the measurement is greatly improved, which makes the operation of the system easier in different circumstances in comparison with the original system without fibre. The results shows the feasibility for simultaneous measurement of material related parameters.

➢ A graphical user interface (GUI) is designed. A measurement manual of the interface is presented in the appendix. The GUI includes four separate interfaces, the start interface, the introduction interface, the main interface and the close interface. The main interface contains the function of collecting SMI signal, wavelet transform, and retrieving the material related parameters.

## 1.5   Thesis organization

This thesis consists of four chapters:

Chapter 1 presents the background of the thesis. It first presents the basic definition of Young's modulus and damping in the material. Due to the importance of these parameters in material engineering, many researches and experiments have been conducted. The measurement methods for Young's modulus and damping are discussed separately. The traditional measurement methods for Young's modulus including tensile test, flexural test and indentation test, which are destructive methods. These methods are destructive and with low accuracy. The non-destructive methods such as resonance and IET based on the principle of fundamental frequencies were developed, which have a better resolution compare to the static methods. The phenomenon of damping in the material refers to the internal friction. The measurement methods for internal friction are categorised into four groups and each method is discussed. The combined methods for measuring both parameters are presented. The SMI technique is briefly introduced. As a non-contact and non-destructive sensing technique, it is featured as high measurement resolution, compact physical configuration and low-cost. It is suitable for both Young's modulus and

internal friction measurements. In the end, a summary of existing research problems and objectives are discussed.

Chapter 2 presents the principle of the measurement. The specimen vibration model is analysed. The specimen can vibrate in the first mode by supporting at $0.224l$ points at each end. The relationship between the specimen vibration and the Young's modulus and internal friction are presented. Then the SMI model is analysed. The existing SMI model for sensing application is derived from the LK equations. A simulation of SMI signal corresponding to the specimen vibration is presented to observe the features. It shows that the material related parameters such as resonant frequency and damping factor can be retrieved from the frequency domain of SMI signal. The wavelet transform is introduced as it is suitable for the time-frequency analysis. By applying wavelet transform onto SMI signal, both resonant frequency and damping factor can be retrieved at the same time. Hence, the Young's modulus and internal friction can be measured simultaneously from SMI signal. The measurement results are discussed and compared with the method in the literature.

Chapter 3 presents the system design. The system for Young's modulus and internal friction measurements consists of two parts, IET part, SMI part. The selection of every component in each part is detailed. The requirement of experiment is discussed, which shows that it is feasible to conduct the experiment. The optical fibre is introduced to the system. Two types of optical fibres, which are single mode fibre and multimode fibre, are described. The fibre coupling for different situations are described, while for the signal mode fibre it has less supported mode and low dispersion rate, for multimode fibre it has more supported mode but high dispersion rate. The selection of optical fibre is made. The fibre polarization controller is introduced to control the polarization state of the light in the fibre. The experiments are conducted with detailed procedures for both SMI system without and with optical fibre. The measurement results from both SMI system are compared. It shows that with the installation of optical fibre in the system, the flexibility is greatly improved and the results remain the same as the results from SMI system without optical fibre. It also shows high repeatability and accuracy compare to the results

in the literature.

Chapter 4 concludes the thesis and suggested future works are discussed.

# Chapter 2    Self-mixing interferometry for measuring material parameters

In chapter 1, the different methods for Young's modulus and internal friction measurement have been reviewed. We also discussed the advantages and disadvantages of each method. The destructive methods for Young's modulus measurement often bring damage to the specimen. The non-destructive methods shows better results and has no damage to the specimen. For the internal friction measurement, the quasi-static method has low accuracy and the system for sub-resonance method is complicated and hard to implement. The resonance method such as half bandwidth method and Logarithmic decrement method are easy and accurate.

This chapter presents the system description. The system model is presented separately with specimen vibration model and SMI model. The relationship between the SMI signal and the material related parameters is discussed. The wavelet transform is applied onto the SMI signal to retrieve the material related parameters. The results of using wavelet transform to analysis SMI signal are discussed.

## 2.1    System description

The overall measuring system of using SMI technique to measure material related

parameters is shown in Figure 2.1. The whole system can be separated as two parts, the IET part and SMI part. The IET part consists of the specimen, support device and a stimulate tool. Use the stimulate tool to apply a light strike on the specimen, the specimen will be stimulated into damping vibration.

The SMI part consists of LD, PD, temperature controller, LD controller, trans-impedance amplifier, oscilloscope, DAQ card and a PC. The LD emits a laser and hits on the specimen. The temperature controller and LD controller are to ensure the LD works in a stable condition. A SMI signal can be generated corresponding to the damping vibration of the specimen, which contains the information for calculating the material related parameters such as Young's modulus, damping ratio and internal friction. The PD packaged in the rear of the LD can collect the SMI signal and pass through the trans-impedance amplifier to be amplified. The DAQ card is used to sample the digital signal. A private computer is uitilised to display the sampled signal and for further signal processing. Alternatively, an oscilloscope can also display the SMI signal.
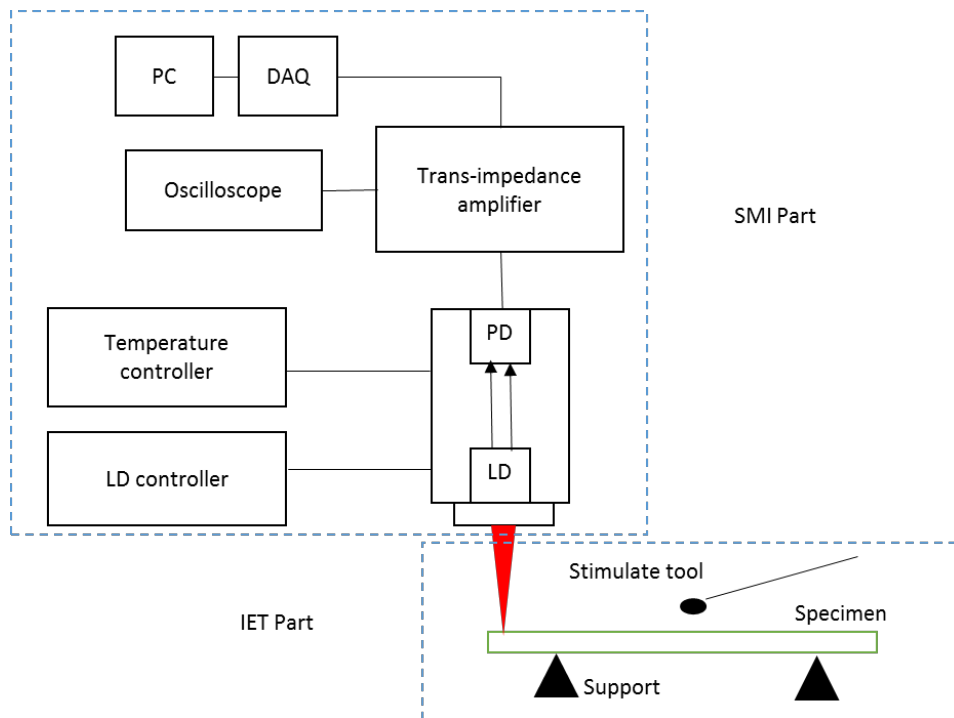


Figure 2.1. Schematic measuring system

## 2.2    System model

The system model includes specimen vibration model and SMI model. The specimen vibration model is to establish the equations of motion for the specimen. The damping vibration of the specimen The SMI model is to establish the mathematical model of SMI.

### 2.2.1  Specimen vibration model

The detection component in SMI system is a laser diode where the laser beam focus on one single point on the specimen. However, there are infinite mass reference points on the specimen, each of which comply with an equation of motion and regularly distributed along the specimen with certain rules. It is important to analysis the vibration models so that we can know what kind of vibration signal we are picking up. The following shows the process of establishing the specimen vibration model.

The vibration of a specimen is governed by the well-known Bernoulli-Euler equation [96] Considering a freely supported specimen (so-called 'free-free') in bending shown in Figure 2.2
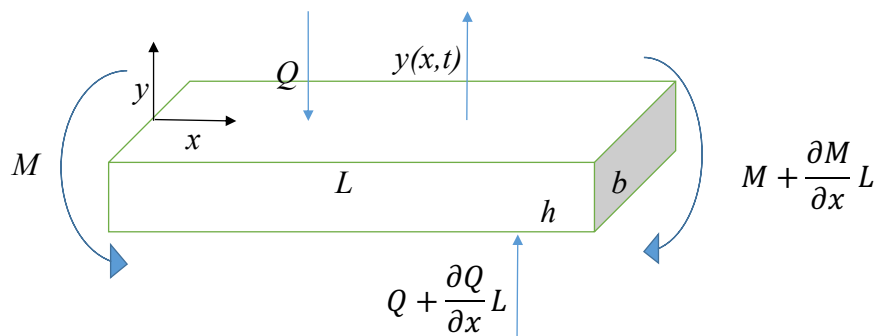


Figure 2.2. Freely supported specimen.

Where $M(x,t)$ is the bending moment, $Q(x,t)$ is the shear force, $y(x,t)$ is the displacement function of an arbitrary point with distance $x$ and at the time $t$, and $f(x,t)$ will be the external force. $L$, $b$ and $h$ are the length, width and height of the specimen.

The equation for equilibrium condition of moments can be written as

$$M + Q \delta x - \left( M + \frac{\partial M}{\partial x} \right) = 0 \qquad (2.1)$$

or

$$Q = \frac{\partial M}{\partial x} = \frac{\partial}{\partial x} \left( EI \frac{\partial^2 y}{\partial x^2} \right) = 0 \qquad (2.2)$$

Where $E$ and $I$ are the Young's modulus and second moment of area of the cross section. When the uniform specimen is not in the consideration, $I(x)$ will be variable along beam length. The equation of motion in the transverse direction for the specimen is

$$(\rho A L) \frac{\partial^2 y}{\partial t^2} = f(x,t) L + Q - \left( Q + \frac{\partial Q}{\partial x} \right) \qquad (2.3)$$

Where $\rho$ is the mass density of the specimen and $A$ is the cross section area of the specimen, equation (2.3) can be simplified as

$$\rho A \frac{\partial^2 y}{\partial t^2} + \frac{\partial Q}{\partial x} = f(x,t) \qquad (2.4)$$

The Euler-Bernoulli equation is obtained from equation (2.2) for the forced transverse vibration

$$\frac{\partial^2}{\partial x^2} \left( EI \frac{\partial^2 y}{\partial x^2} \right) + \rho A \frac{\partial^2 y}{\partial t^2} = f(x,t) \qquad (2.5)$$

When the uniform specimen is considered, equation (2.5) becomes

$$EI \frac{\partial^4 y}{\partial x^4} + \rho A \frac{\partial^2 y}{\partial t^2} = f(x,t) \qquad (2.6)$$

When the external force $f(x,t) = 0$, the specimen is in the free vibration. The motion equation becomes

$$\frac{\partial^2}{\partial x^2} \left( EI \frac{\partial^2 y}{\partial x^2} \right) + \rho A \frac{\partial^2 y}{\partial t^2} = 0 \qquad (2.7)$$

For a uniform specimen, the $EI$ is constant when the specimen is uniform. Then the motion equation in (2.7) becomes

$$c^2 \frac{\partial^2 y}{\partial x^4} + \frac{\partial^2 y}{\partial t^2} = 0 \tag{2.8}$$

Where

$$c = \sqrt{\frac{EI}{\rho A}} \tag{2.9}$$

The solution to equation (2.8) can be produced by, first obtaining the natural frequencies and mode shapes of the specimen and then expressing the general solution as a summation of modal responses. In each mode, the specimen vibrates in a fixed shape ratio which separates the displacement function $y(x,t)$ into a space only function and time only function,

$$y(x,t) = X(x)T(t) \tag{2.10}$$

Considering the free vibration of a uniform specimen, the free vibration solution will be obtained by substituting equation (2.10) into equation (2.8) and it becomes

$$\frac{c^2}{X(x)} \frac{\partial^4 X(x)}{\partial x^4} = -\frac{1}{T(t)} \frac{\partial^2 T(t)}{\partial t^2} = \omega^2 \tag{2.11}$$

Where $\omega^2$ is defined as constant. Since the first part of the equation (2.11) is only a function of space, and the middle part is only a function of time, and they both equal to a constant. The equation (2.11) can be rearranged as two separate functions, the spatial function and temporal function,

$$\frac{d^4 X(x)}{dx^4} - \beta^4 X(x) = 0$$
$$\frac{d^2 T(t)}{dt^2} + \omega^2 T(t) = 0, \beta^4 = \frac{\omega^2}{c^2} \tag{2.12}$$

The general solution of spatial function in equation (2.12) is a mode shape and given by

$$X(x) = a_1 \sin(\beta x) + a_2 \cos(\beta x) + a_3 \sinh(\beta x) + a_4 \cosh(\beta x) \tag{2.13}$$

For a free-free specimen, the boundary conditions are used to make sure the zero moment and zero force at both ends of the specimen,

$$EI \frac{\partial^2 y}{\partial x^2}\big|_{x=0} = EI \frac{\partial^2 y}{\partial x^2}\big|_{x=L} = 0 \tag{2.14}$$

$$EI \frac{\partial^3 y}{\partial x^3} |_{x=0} = EI \frac{\partial^3 y}{\partial x^3} |_{x=L} = 0 \qquad (2.15)$$

By substituting equation (2.10) into the boundary condition in equation (2.14), and taking the second spatial derivative in equation (2.13), it gives the result that

$$a_2 = a_4 \qquad (2.16)$$

and similarly we can get

$$a_1 = a_3 \qquad (2.17)$$

The boundary condition of zero moment at $x = L$ gives the result

$$a_1 \sin(\beta L) + a_2 \cos(\beta L) = a_3 \sinh(\beta L) + a_4 \cosh(\beta L) \qquad (2.18)$$

$$a_1 \cos(\beta L) + a_2 \sin(\beta L) = a_3 \cosh(\beta L) + a_4 \sinh(\beta L) \qquad (2.19)$$

Using the equation (2.16) and (2.17) the equation (2.18) and (2.19) can be arranged in matrix form

$$\begin{bmatrix} \sinh(\beta L) - \sin(\beta L) & \cosh(\beta L) - \cos(\beta L) \\ \cosh(\beta L) - \cos(\beta L) & \sin(\beta L) + \sinh(\beta L) \end{bmatrix} \begin{bmatrix} a_1 \\ a_2 \end{bmatrix} = \begin{bmatrix} 0 \\ 0 \end{bmatrix} \qquad (2.20)$$

For a nontrivial solution the determinant of the matrix has to vanish so we can get

$$\cosh(\beta L)\cos(\beta L) = 1 \qquad (2.21)$$

The transcendental equation (2.21) has infinite solutions, with the $n$ th root is denoted as $(\beta_n L)$. Table 2.1 shows the solution of the equation (2.21).

Table 2.1. Solutions of transcendental equation for a free-free specimen

| Root | Value |
|------|-------|
| $\beta_0 L$ | 0(rigid body) |
| $\beta_1 L$ | 4.73004074 |
| $\beta_2 L$ | 7.85320462 |
| $\beta_3 L$ | 10.9956078 |
| $\beta_4 L$ | 14.1371655 |
| $\beta_n L$ | (2n+1)π/2 |

Substituting equation (2.16), (2.17) and (2.20) into equation (2.13), it gives the result

$$X_n(x) = A_n \left[ \left[ \sinh(\beta_n x) + \sin(\beta_n x) \right] + \frac{\sin(\beta_n L) - \sinh(\beta_n L)}{\cosh(\beta_n L) - \cos(\beta_n L)} \left[ \cosh(\beta_n x) + \cos(\beta_n x) \right] \right] \qquad (2.22)$$

Equation (2.22) describes the $n$th mode shapes of a free-free specimen, where $A_n$ an unknown constant in general is complex, determined by the initial conditions at $t = 0$ on the velocity and displacements of the specimen. The motions of a free-free specimen are the combination of these mode shapes. Figure 2.3 shows the first 4 mode shapes of a free-free specimen.
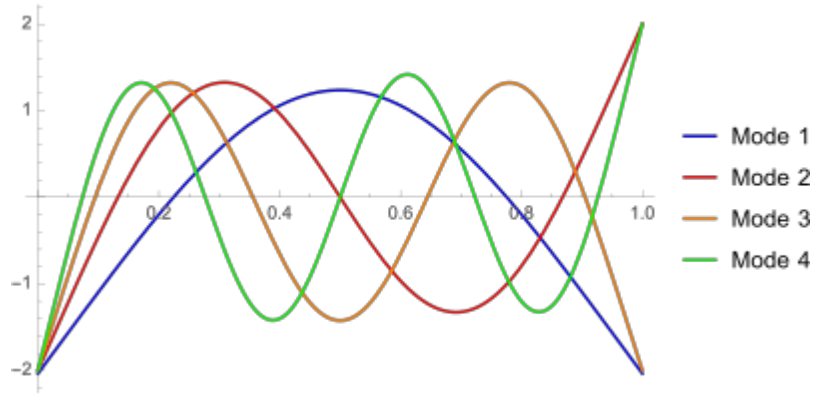


Figure 2.3. First 4 mode shapes of a free-free specimen

The general solution for the temproal function in equation (2.12) after removing the external force is

$$T_n(t) = B_n e^{-\xi \omega_n t} \cos(\omega_n \sqrt{1 - \xi^2} t + \phi_n) \qquad (2.23)$$

Where $B_n$ and $\phi_n$ are also determined by the initial conditions at $t = 0$ on the velocity and displacements of the specimen. By substituting both spatial function solution and temporal function of equation (2.12) in equation (2.10), we can get a general expression for the motion of a free-free specimen

$$y(x,t) = \sum_{n=1}^{\infty} y_n e^{-\xi \omega_n t} \cos(\omega_n \sqrt{1 - \xi^2} t + \phi_n) \qquad (2.24)$$

Where $y_n = X_n(x)$ shown in equation (2.22), damping ratio $\zeta$ and natural frequencies $\omega_n$. It shows that each mode shape has its own natural frequency. From equation (2.12),

we can get characteristic equation of $\omega_n$

$$\omega_n = \beta_n^2 c = (\beta_n L) \sqrt{\frac{EI}{\rho A L^4}}$$ (2.25)

The motion of a free-free specimen in equation (2.24) can be simplified based on the location of the supports. The specimen we use to determine Young's modulus and internal friction is in a shape of thin bar, which is very suitable for the flexural vibration. The location of supports for the specimen depends on where the nodes and anti-nodes are. Nodes are the points which are stationary and with zero amplitude in a sinusoidal wave. The opposite of nodes are anti-nodes, where the amplitudes are maximum in a sinusoidal wave. Figure 2.4 shows the node points in each mode shape of flexural vibration. At the lowest resonance frequency of a specimen, which is in mode 1 shown in Figure 2.3, the nodes are located at $0.224L$ from each end, which means that these two points have minimum amplitude 0 and the centre and two ends have the maximum amplitude.
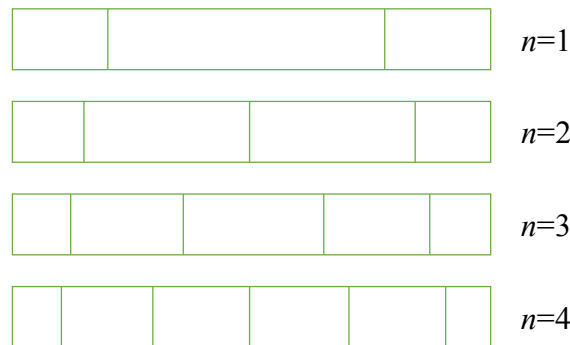


Figure 2.4. Nodes location of each mode shape of flexural vibration

The equation (2.24) can be simplified to only mode 1 where $n = 1, \beta_1 L = 4.73$, with the support locations are at $0.224L$ from each end.

$$y(t) = y_1 e^{-\xi \omega_1 t} \cos(\omega_1 \sqrt{1 - \xi^2} t + \phi_1)$$ (2.26)

Where $y_1$ is the maximum amplitude, $\omega_1$ is the natural frequency and $\phi_1$ is the phase all under the mode 1 vibration. The motion trail of the reference point can be written as

$$y(t) = A_0 e^{-kt} \cos(2\pi f_{RO} t)$$ (2.27)

Where $A_0 = y_1$ is the maximum amplitude of the vibration, $k = \dfrac{\zeta}{\sqrt{1-\zeta^2}} \cdot 2\pi f_{RO}$ is the

damping factor, $f_{RO} = \dfrac{\omega_1}{2\pi}\sqrt{1-\zeta^2}$ is the resonant frequency.

Different from destructive methods based on direct measurement of stresses and strains during the mechanical tests, non-destructive methods like IET based on resonant frequency principle measures the resonant frequency of the specimen in flexural or longitudinal mode of vibration. The Young's modulus can be determined if the geometry, mass and resonant frequency of a suitable specimen of the material can be measured. For the flexural vibration mode of a thin bar specimen, the calculation of Young's modulus follows the rule as

$$E = 0.9465 \cdot \frac{mf_{RO}^2 L^3}{bh^3} \cdot T \tag{2.28}$$

Where $T = 1 + 6.585\left(\dfrac{h}{L}\right)^2$ when $L/h \geq 20$ [97, 98]. $m$, $L$, $b$, and $h$ are the mass, length, width, and height of the specimen. The remaining value needs to be determined is $f_{RO}$, which can be found in equation (2.27). The objective of resonant frequency method is to measure $f_{RO}$ from the vibration of the specimen.

Internal friction or damping can be determined from the decay of vibration amplitude view. A specimen excited into flexural vibration, after removing the excitation the specimen vibrates in a damping vibration shown in equation (2.27). Figure 2.5 shows the simulated vibration signal of equation (2.27). The damping ratio $\zeta$ can be determined by the evolution of the damping factor $k$, where $k$ can be calculated as

$$k = \frac{\ln\left(\dfrac{y_1}{y_2}\right)}{t_2 - t_1} \tag{2.29}$$

Where $x_1$ and $x_2$ are the amplitudes at time $t_1$ and $t_2$ indicates the amplitude decrement in one period. We know that $k = \dfrac{\zeta}{\sqrt{1-\zeta^2}} \cdot 2\pi f_{RO}$ from equation (2.27) so the

damping ratio $\zeta$ can be calculated by knowing the value of $k$ and $f_{RO}$. The internal friction (denoted by $Q^{-1}$) can be calculated as

$$Q^{-1} = \frac{k}{\pi f_{RO}}$$

(2.30)
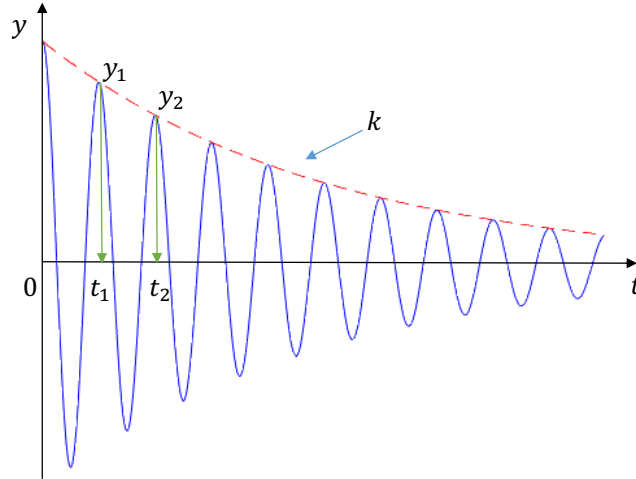


Figure 2.5. Damped vibration from equation (2.27)

In summary, the Young's modulus and internal friction can be determined once the value of resonant frequency $f_{RO}$ and damping factor $k$ are obtained from the damping vibration of the specimen. For this purpose, we can use SMI system to pick up the vibration signal from the specimen and retrieve these values.

## 2.2.2  SMI model

The mathematical model of SMI can be either derived from the three-mirror model [99] with facet reflection coefficients and the remote target reflection coefficient, or by the well-known Lang and Kobayashi (LK) equations, which are based on Lamb's equation and modified with the additional equations for the state concentration [100]. Compared to the conventional three-mirror model, LK equations describe the dynamics and stability

of a LD with optical feedback more completely which are shown as below [102]. Table 2.2 shows the physical meanings of the parameters in the equations.

$$\frac{dE(t)}{dt} = \frac{1}{2}\left\{G[N(t),E(t)] - \frac{1}{\tau_p}\right\}E(t) + \frac{\kappa}{\tau_{in}} \cdot E(t-\tau)$$
$$\cdot \cos[\omega_0\tau + \phi(t) - \phi(t-\tau)] \tag{2.31}$$

$$\frac{d\phi(t)}{dt} = \frac{1}{2}\alpha\left\{G[N(t),E(t)] - \frac{1}{\tau_p}\right\} - \frac{\kappa}{\tau_{in}} \cdot \frac{E(t-\tau)}{E(t)}$$
$$\cdot \sin[\omega_0\tau + \phi(t) - \phi(t-\tau)] \tag{2.32}$$

$$\frac{dN(t)}{dt} = \frac{J}{eV} - \frac{N(t)}{\tau_s} - G[N(t),E(t)]E^2(t) \tag{2.33}$$

Table 2.1    Physical meanings of the parameters in LK equations

| Symbol | Physical Meaning |
|--------|------------------|
| $E(t)$ | Laser electric field amplitude |
| $G_N$ | Modal gain coefficient |
| $N(t)$ | Carrier density at transparency |
| $\tau_p$ | Photon lifetime |
| $\kappa$ | Feedback parameter |
| $\tau_{in}$ | Internal cavity round trip time |
| $\tau$ | External cavity round trip time |
| $\omega_0$ | Angular frequency for the LD without feedback |
| $\phi(t)$ | Laser electric field phase |
| $\alpha$ | Linewidth enhancement factor |
| $J$ | Injection current |
| $e$ | Elementary charge |
| $V$ | Volume of active region |
| $\tau_s$ | Carrier life time |

$G_N\big[N(t),E(t)\big]$ is the modal gain per unit of time expressed as [101]

$$G\big[N(t),E(t)\big]= G_N\big[N(t)-N_0\big]\cdot\big[1-\varepsilon\Gamma E^2(t)\big]\qquad(2.34)$$

Where $\varepsilon$ and $\Gamma$ are the nonlinear gain compression coefficient and confinement factor respectively. When neglecting the nonlinear effect, the modal gain can be simplified as

$$G\big[N(t),E(t)\big]= G_N\big[N(t)-N_0\big]\qquad(2.35)$$

$\phi(t)$ is given by $\phi(t) =\big[\omega(t)-\omega_0\big]t$, where $\omega(t)$ is the angular frequency for the LD with external optical feedback. The dynamics of the SMI system are governed by the injection current $J$ and other parameters associated with external cavity, feedback parameter $\kappa$ and external cavity round trip time $\tau$. Other parameters in the LK equations relate to the property of LD often treated as constants.

The current SMI model is derived from the stationary solutions of the LK equations. When the system described by the LK equations enters into a stationary state, we have

$$\frac{dE(t)}{dt}=0$$
$$\frac{d\phi(t)}{dt}=\omega_s-\omega_0\qquad(2.36)$$
$$\frac{dN(t)}{dt}=0$$

Where $\omega_s$ is the stabled angular frequency. Substituting $E(t)$ and $N(t)$ with stabled electric field amplitude $E_s$ and carrier density $N_s$ and $\phi(t) =\big[\omega(t)-\omega_0\big]t = (\omega_s-\omega_0)t$ into LK equations, the well-known stationary solutions can be obtained as [73, 101-103]

$$\omega_s\tau = \omega_0\tau - \frac{\kappa}{\tau_{in}}\tau\sqrt{1+\alpha^2}\,\sin(\omega_s\tau+\arctan\alpha)\qquad(2.37)$$

$$N_s = N_0 + \frac{1}{\tau_p G_N} - \frac{2\kappa\cos(\omega_s\tau)}{\tau_{in}G_N}\qquad(2.38)$$

$$E_s^2 = \frac{J/(eV)-N_s/\tau_s}{G_N(N_s-N_0)}\qquad(2.39)$$

For a moving target, the external cavity length varies with time. Hence, we can replace $\omega_s\tau$ and $\omega_0\tau$ by $\phi_s$ and $\phi_0$. We also introduce $C$, the feedback level, to replace

$\dfrac{\kappa}{\tau_{in}}\tau\sqrt{1+\alpha^2}$ for the convenience. Note that $C$ in an important parameter as it characterizes the waveform of SMI signals, which is important for the later measurement analysis. The equation (2.37) can be rewritten

$$\phi_s = \phi_0 - C\sin(\phi_s + \arctan\alpha) \tag{2.40}$$

Where $\phi_0$ is associated with the external cavity length $L$

$$\phi_0 = 4\pi L/\lambda \tag{2.41}$$

Where $\lambda$ is the unperturbed laser wavelength. Equation (2.40) is called phase equation, which can also be derived from the three mirrors model [104]. This phase equation is the core part of the current SMI model. By substituting equation (2.38) into equation (2.39), the normalized variation of the LD output power can be expressed as

$$G(t) = \cos(\phi_s) \tag{2.42}$$

$$P(t) = P_0\left[1 + mG(t)\right] \tag{2.43}$$

Where $G(t)$ is the interferometric function, $P(t)$ and $P_0$ are the laser power emitted by the LD with and without external optical feedback, and $m$ is the modulation index. Equation (2.42) and equation (2.40) constitute the current SMI model that have been widely accepted to describe the waveforms of SMI signals [105-107]. The interferometric function $G(t)$ is referred as SMI signal. The external cavity length $L$ can be represented as $L = L_0 + y(t)$, where $L_0$ is the initial external cavity length, that is the distance between the LD and the external target the specimen in static state. $y(t)$ describes the vibration of the specimen which can be referred to equation (2.27) $y(t) = A_0 e^{-kt}\cos(2\pi f_{RO}t)$. Figure 2.6 shows scheme of using SMI system to pick up external target vibration information. The vibration information $y(t)$ is captured in SMI signal followed by the procedure of $y(t) \rightarrow \phi_0 \rightarrow \phi_s \rightarrow G(t)$. The retrieving of vibration information in $y(t)$ such as $k$ and $f_{RO}$ followed by the opposite procedure $G(t) \rightarrow \phi_s \rightarrow \phi_0 \rightarrow y(t)$.
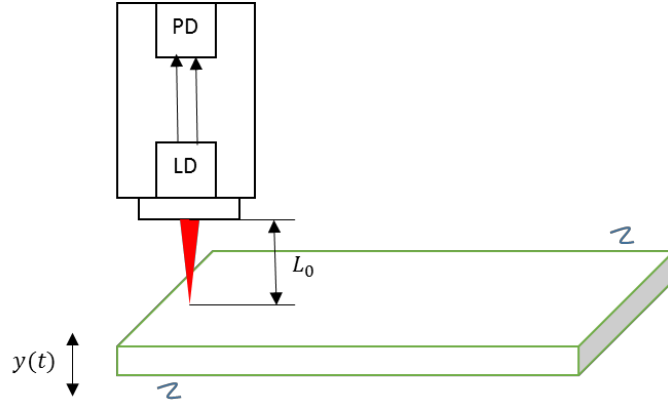
Figure 2.6. Schematic of using SMI system to pick up external target vibration information

## 2.3 Relationship between the SMI signal and the material parameters

From the literature review, we have discussed about the applications of SMI technique. The SMI technique can be used for displacement measurement. In this thesis, we use SMI technique to measure the Young's modulus and internal friction of the specimen. The principle of Young's modulus and internal friction measurement is to retrieve the resonant frequency and damping factor from vibration information of the specimen as it is mentioned in 2.2.1. By the simulation of SMI signal corresponding to specimen vibration, we can find the relationship between the SMI signal and the material related parameters. The SMI equations are relisted as below

$$\phi_0 = 4\pi L / \lambda \tag{2.44}$$

$$\phi_s = \phi_0 - C\sin(\phi_s + \arctan\alpha) \tag{2.45}$$

$$G(t) = \cos(\phi_s) \tag{2.46}$$

$$P(t) = P_0\left[1 + mG(t)\right] \tag{2.47}$$

Where $L = L_0 + y(t)$, $L_0$ is the initial external cavity length and $y(t)$ the damping vibration of the specimen. For the simulation, the values set for the parameters associated

39

to SMI system and the specimen are listed in table 2.3. The specimen in this thesis is a rectangular brass bar with dimension listed in table 2.3. Based on the literature [108], the Young's modulus of the brass specimen is estimated as 120Gpa. The resonant frequency $f_{RO}$ is calculated as 444Hz from equation (2.28). We assume the damping ratio $\zeta = 0.0015$ (for metal specimen $\zeta$ is between 0.001 and 0.002). So the damping factor $k$ can be calculated as 4.6 based on equation $k = \dfrac{\zeta}{\sqrt{1-\zeta^2}} \cdot 2\pi f_{RO}$.

Table 2.2. Simulation values for parameters in the system

| | Parameter | Value |
|---|---|---|
| | feedback level $C$ | 3 |
| | laser wavelength $\lambda$ | $7.85\times10^{-9}$m |
| SMI system related parameters | linewidth enhancement factor $\alpha$ | 6 |
| | sampling time $t$ | 1s |
| | sampling frequency $f_s$ | 100kHz |
| | initial external cavity length $L_0$ | 0.12m |
| | specimen length $L$ | 138.35mm |
| | specimen width $b$ | 12.06mm |
| | specimen height $h$ | 2.23mm |
| Specimen related parameters | specimen mass $m$ | 30.65g |
| | maximum amplitude of the vibration $A_0$ | $4.317\times10^{-6}$m |
| | damping factor $k$ | 4.6 |
| | resonant frequency $f_{RO}$ | 444Hz |

From the external vibration signal $y(t)$, we can get the SMI signal $G(t)$ through the stationary solution of SMI model equation (2.44) to equation (2.47). Figure 2.7 shows the simulation results of vibration signal $y(t)$ and its corresponding SMI signal $G(t)$. Note

that $G(t)$ can be obtained by normalizing $P(t)$ in the experiment. For clear observation, we choose two parts indicated in Figure 2.7 to zoom in and show the detail in Figure 2.8.
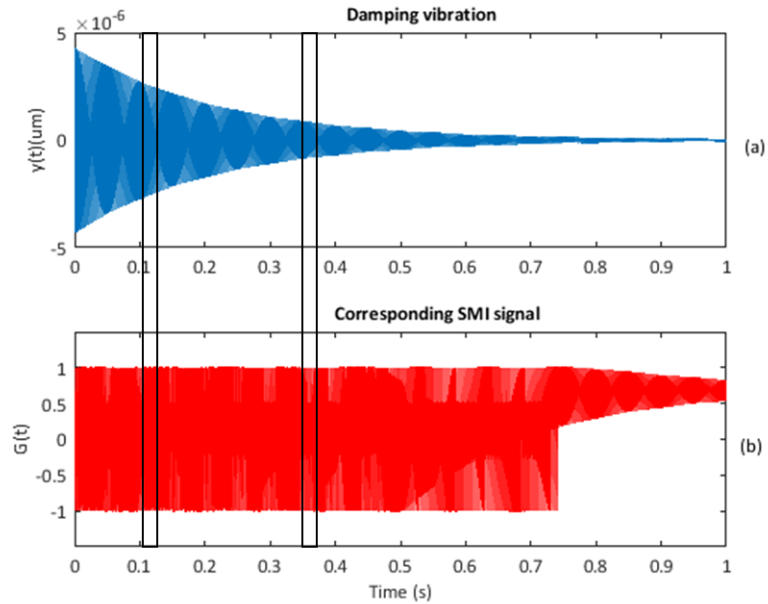


Figure 2.7. (a) External target vibration $y(t)$ and (b) its corresponding SMI signal $G(t)$ (normalised)
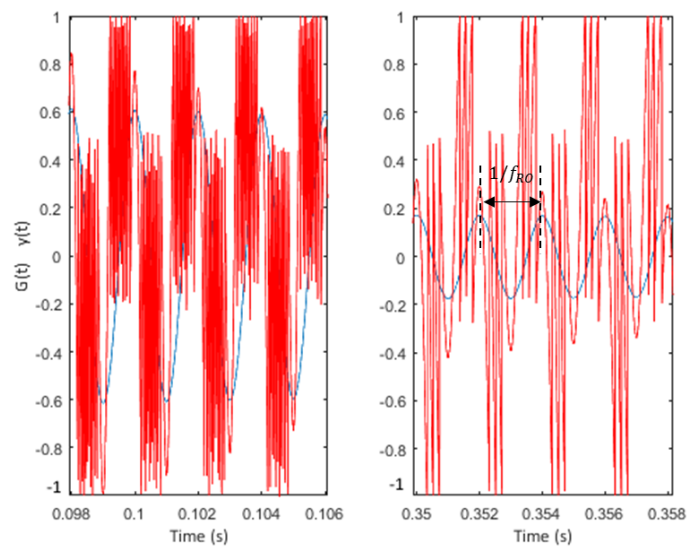


Figure 2.8. Zoomed in part from both external target vibration $y(t)$ and its corresponding SMI signal $G(t)$.

From the Figure 2.7 and 2.8 we can observe that

➢ The fundamental period of SMI signal $G(t)$ is the same as the period of the vibration signal $y(t)$ denoted by $1/f_{RO}$

➢ The SMI signal moves the same direction as the reference point on the external target moves close or away from the laser.

➢ The fringe numbers on the SMI signal $G(t)$ indicates the magnitude of the vibration of the reference point on the external target in each vibration period, where each fringe on an SMI signal corresponds to a half-wavelength shift of the external target in the stable region [71].

➢ The fringe numbers decreases as the external target vibration magnitude decreases with time.

From the features observed above, it can be found that the external target vibration information, the resonant frequency $f_{RO}$ and the damping factor $k$ are carried in the SMI signal $G(t)$. For the resonant frequency $f_{RO}$, it can be retrieved by measuring the fundamental frequency of the SMI signal $G(t)$. For the damping factor $k$, it can be retrieved by measuring the decay of the fringe numbers in the SMI signal $G(t)$. The decay of fringe numbers in the SMI signal $G(t)$ can be treated as the decay of the high frequencies component in the SMI signal $G(t)$. The external target vibration information can be found by the frequency domain analysis of the SMI signal $G(t)$. To achieve this, the continuous wavelet transform (CWT) can be applied onto the SMI signal $G(t)$.

## 2.4    Wavelet transform on SMI signal

From the last section, we have found the features of an SMI signal, the fundamental frequency of the SMI signal is the same as the resonant frequency, and the decay of fringe numbers which is also the decay of high frequencies in the SMI signal corresponding to the damping factor. The measurements of resonant frequency $f_{RO}$ and damping factor $k$

become the measurement of the fundamental frequency and the decay of high frequencies in the SMI signal. There are different ways to do frequency domain analysis such as the most common one, Fourier transform. However, in our case, the Fourier transform cannot satisfy the simultaneous measurement of both resonant frequency $f_{RO}$ and damping factor $k$, where the Fourier transform can analyse the frequency components in a SMI signal but it shows poor resolution for the time-frequency analysis. So we introduce wavelet transform, which is capable of providing better time and frequency information simultaneously [109].

## 2.4.1 Wavelet transform

As an important and powerful tool of signal representation, wavelet transform has been widely used in signal processing [110], signal denosing [111], data compression [112] and image processing [113]. In Fourier transform, the analysing functions are complex exponentials. The resulting transform is a function of a single variable, which is only the frequency information. The temporal information is lost in this process. The short time Fourier transform (STFT) were developed to do the time-frequency analyse of signals. STFT divides a long time signal into shorter windows of equal length and then compute the Fourier transform separately on each shorter window. Based on the uncertainty principle [114], it is impossible to have high resolution in both time and frequency. However, by varying the length of window, one can treat the time resolution for the frequency resolution. In continuous wavelet transform (CWT), the width of the window is changed during the transform, for more precise low frequency information it uses longer width window, for more precise time information in the high frequency it uses shorter width window. Figure 2.9 shows the segment sizes used in STFT and CWT
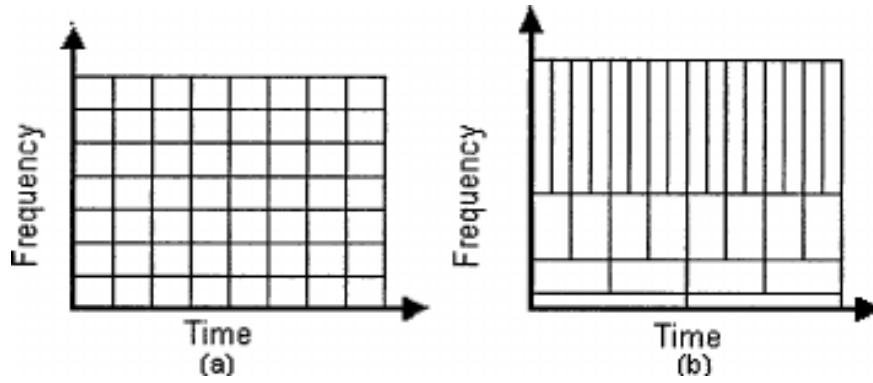
Figure 2.9. (a) STFT with fixed segment size; (b) CWT with variable segment size [115]

In the CWT, the analysing function $\psi$ is defined as localized waveform, which oscillate only for a given moment in time and rapidly decay to zero. Unlike the analysing function $e^{j\omega t}$ in Fourier transform, wavelet $\psi$ is localized in the time and frequency domains. Due to dynamic nature of SMI signals, wavelet transform is well-suited for their analysis, especially in our case both low frequency and high frequency need to be analysed. The CWT of a SMI signal can be written as [110]

$$W(a,b) = \frac{1}{\sqrt{a}} \int_{-\infty}^{+\infty} G(t)\psi\left(\frac{t-b}{a}\right) dt \qquad (2.48)$$

Where $W(a,b)$ is the coefficient of the transform, $a$ represents the scale wavelet parameter, $b$ represents the shifting wavelet parameter and $\psi\left(\frac{t-b}{a}\right)$ is the scaled and shifted version of mother wavelet $\psi(t)$. $W(a,b)$ is normalized by $\frac{1}{\sqrt{a}}$ to ensure all the wavelets have the same energy at every scale. Scale $a$ is inversely proportional to the frequency component of the analysed signal. There are different mother wavelets, the choosing of one of them depends on the nature and of the analysed signal. An SMI signal waveform is sinusoidal-like or sawtooth-like. The Morlet complex wavelet is chosen to analyse our SMI signals because it shows good results in analysing sinusoidal-like signal [116]. The Morlet wavelet is defined in the time domain as

$$\psi(t) = e^{i\omega_e t} e^{\frac{-t^2}{2}} \qquad (2.49)$$

44

In the frequency domain

$$\Psi(\omega) = \int_{-\infty}^{+\infty} \psi(t)e^{-j\omega t}\,dt = \sqrt{2\pi}e^{\frac{-(\omega-\omega_e)^2}{2}} \qquad (2.50)$$

Where $\omega_e$ is the central angular frequency of the wavelet. The admissibility condition for a wavelet is

$$\int_0^{+\infty} \frac{|\Psi(\omega)|^2}{|\omega|}\,d\omega < +\infty \qquad (2.51)$$

It requires the Fourier transform of the wavelet should be zero at zero frequency, $|\Psi(\omega)| = 0$, $\omega = 0$. Using the admissibility condition in equation (2.51), the following can be obtained

$$\Psi(0) = \sqrt{2\pi}e^{\frac{-\omega_e^2}{2}} \qquad (2.52)$$

Figure 2.10 shows the value of $\Psi(0)$ at different $\omega_e$ for Morlet wavelet. For $\omega_e \geq 5$, the admissibility condition is fulfilled. $\omega_e = 6$ is chosen for the simulation
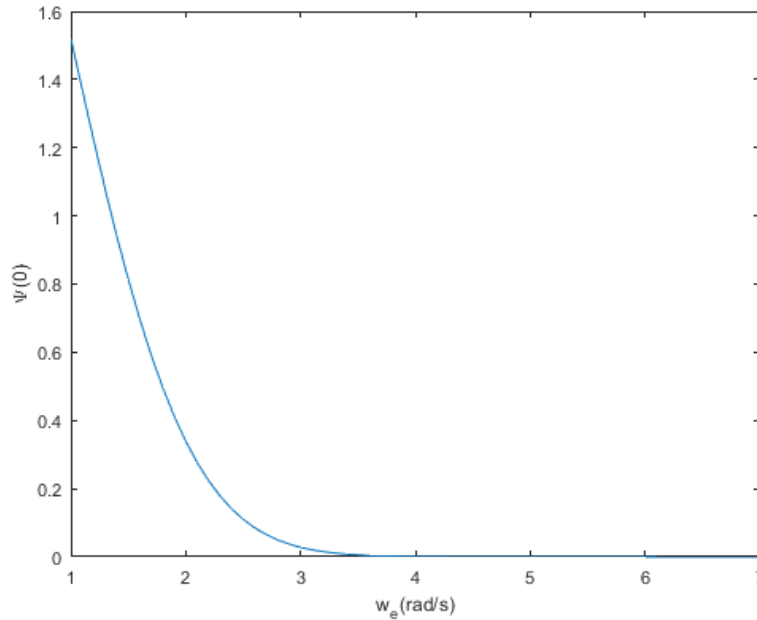


Figure 2.10. Admissibility condition for the Morlet wavelet

In wavelet analysis, the way to relate scale parameter $a$ to frequency is to determine the central frequency of the wavelet, $f_e = \omega_e/(2\pi)$, where we have set the value for $\omega_e = 6$. So $f_e = \omega_e/(2\pi) \approx 0.9549\,\text{Hz}$. The frequency content (denoted by $f_a$) is $f_a = \dfrac{f_e}{a} = \dfrac{0.9549}{a}$. Due to the dyadic nature of wavelets [117, 118], it is computationally efficient to choose scale parameter $a$ in terms of a power of 2. $a = a_0 \times 2^{jd}$, $j = 0,1,2..J-1$, where $a_0$ is the smallest resolvable scale corresponding to the Nyquist frequency which is half of the sampling frequency $f_{\max} = \dfrac{f_s}{2} = \dfrac{100kHz}{2} = 50kHz$ (the sampling frequency $f_s$ was set as $100kHz$ from previous section). Then we have $a_0 = \dfrac{f_0}{f_{\max}} = \dfrac{0.9549}{50kHz}$. $d$ is the increment in scale and it is chosen to be $1/16$ to balance the resolution and computing time. The total scale $J$ can be set based on the frequency range to be analysed, where we already have the maximum frequency $f_{\max} = 50kHz$, and we set the minimum frequency to be $f_{\min} = 1Hz$. Therefore, we will analyse the frequency range between $1Hz$ and $5 \times 10^4\,Hz$, which determines the number of octaves $N = floor\left(\log_2\left(\dfrac{f_{\max}}{f_{\min}}\right)\right) = 15$. The total number of scales are $J+1 = \dfrac{N}{d}+1 = 241$.

## 2.4.2 Retrieve the material related parameters from a SMI signal

The following flow chart in Figure 2.11 shows the procedure of determining the resonant frequency $f_{RO}$ and the damping factor $k$ of target vibration.
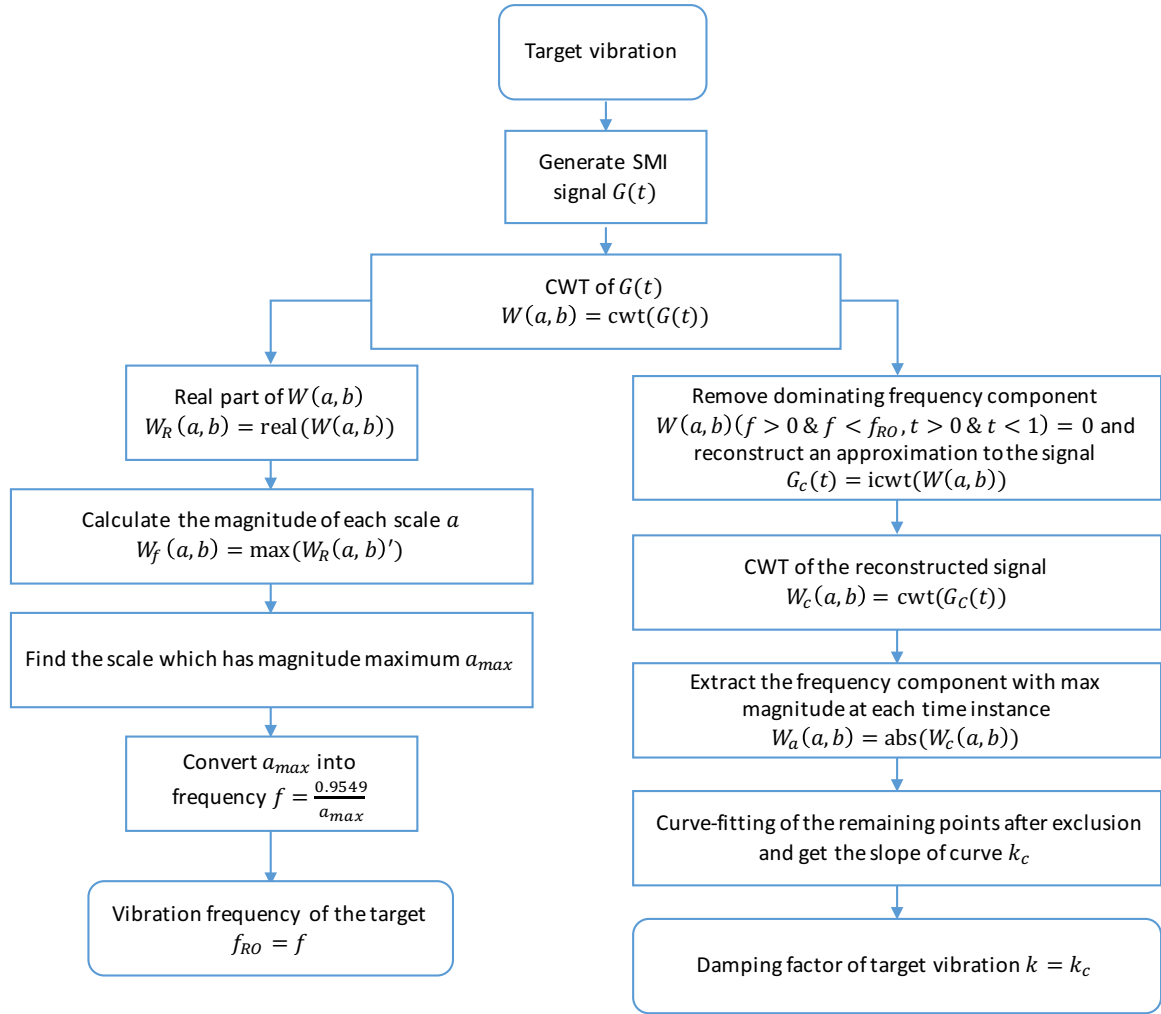
Figure 2.11. Flow chart of determining the vibration information from a SMI signal

From the section 2.3, we have set the simulation value for the vibration signal so the vibration signal can be written as below

$$y(t) = 4.317 \times 10^{-6} e^{-4.6t} \cos(2\pi(444t)) \tag{2.53}$$

We use the SMI model described by equation (2.44) to (2.47) to generate the corresponding SMI signal $G(t)$. Then compute the Morlet wavelet CWT of $G(t)$, that is $W(a,b)$ by equation (2.48). The scalogram of the real part of $W(a,b)$ is plotted to visualize the spatial and temporal components of SMI signal $G(t)$, as shown in Figure 2.12.
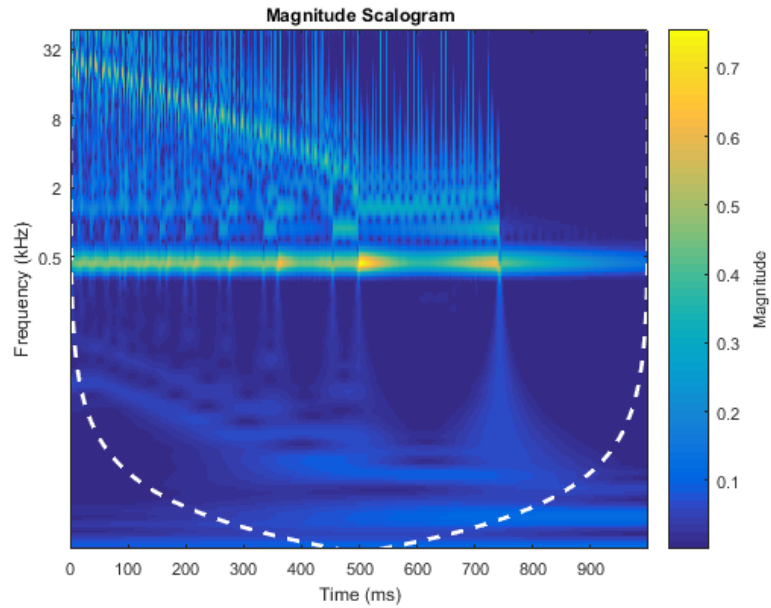
Figure 2.12. Scalogram of the CWT of SMI signal

In Figure 2.12, the horizontal axis represents the time index, the vertical axis represents the frequency index (note that the vertical axis is logarithmic) and the colour means the magnitude (from 0.1 to 0.7, blue to yellow). It can be seen that the yellow colour located at frequency around 450Hz appears in the time period from $t = 0$ ms to about $t = 700$ ms, which is the dominating frequency contained in the SMI signal. It is the same as the frequency of the target vibration. It also can be found that a yellow line in decreasing trend from $t = 0$ ms to about $t = 500$ ms with frequency varying from 32kHz to 1kHz. This decreasing trend line indicates the decreasing of the fringe numbers in each vibration period in the SMI signal $G(t)$.

First, we decide the value of the dominating frequency by extracting the frequency component with maximum magnitude from the scalogram in Figure 2.12. The frequency component with maximum magnitude is $f = 443.6$ Hz, which is shown in Figure 2.13.
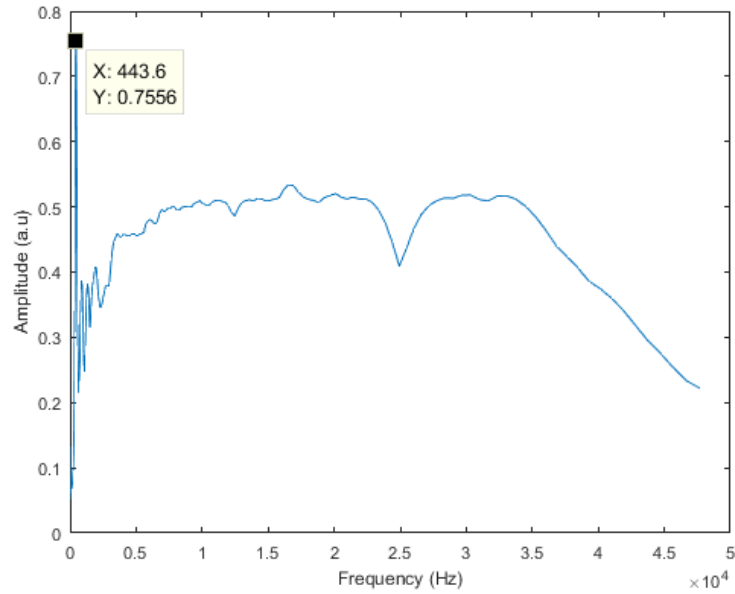
Figure 2.13. Real part of $W(a,b)$ plotted against the frequency, at $f = 443.6$ Hz, denoting the maximum frequency is 443.6Hz

Then, we decide the value of the slope of the decreasing trend, in order to do so we need to locate the high frequency component from the scalogram in Figure 2.12. The can be achieved by extracting the frequency component with maximum magnitude at each time instance. However, it can be seen that the dominating frequency, which is around 500Hz, will significantly affect the accuracy. The frequency component smaller than 750Hz from $t = 0$ ms to $t = 1000$ ms can be removed by zeroing out the CWT coefficients. Use the inverse CWT to reconstruct an approximation to the signal. The CWT of the reconstructed signal is displayed in Figure 2.14.

49
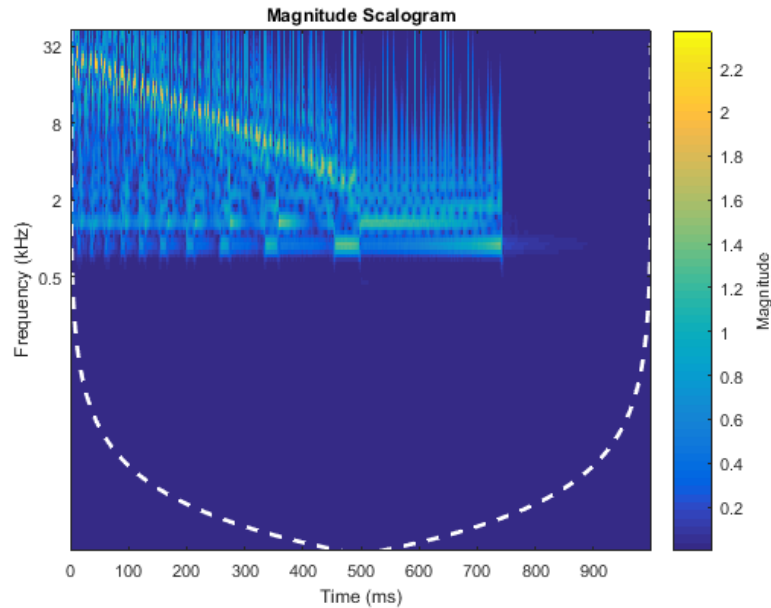
Figure 2.14. Scalogram of reconstructed SMI after removing the frequencies smaller than 750Hz from $t = 0$ ms to $t = 1000$ ms.

After removing the low frequency affect, we can extract the frequency component with maximum magnitude at each time instance from the rest of the scalogram in Figure 2.14. The extraction result is shown in Figure 2.15 (note that the vertical axis is coordinate). The highest frequency component in each time interval represents the high frequency of each fringe in SMI signal, so that the last result of each discontinued piece was extracted and the other points are set as zeros. The curve-fitting result from the rest of points, which is shown in Figure 2.16. It can be seen that the most of the points fall on the curve, which shows the curve can represent the descent trend of the high frequency component in the SMI signal (the fringe numbers). The slope of the decreasing trend is -4.69, so the measured $k_c = 4.69$.
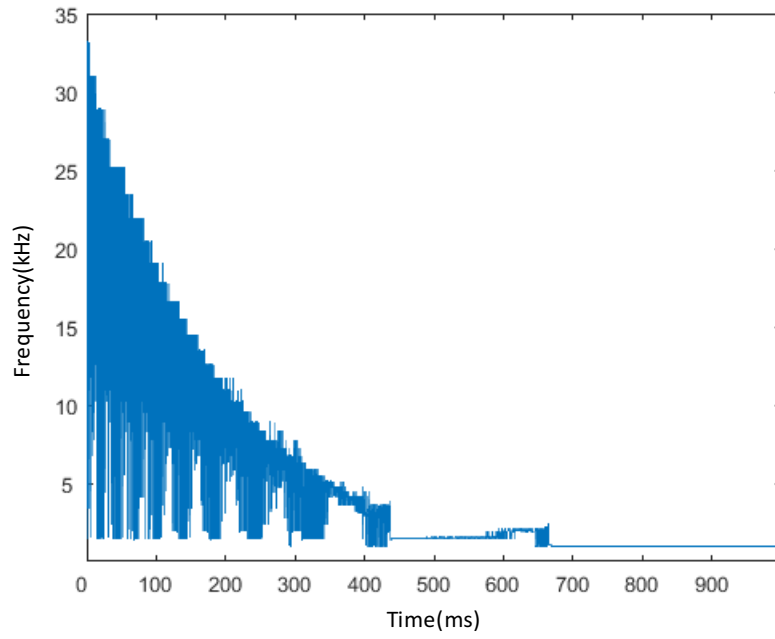
Figure 2.15. Extraction of the frequencies with maximum magnitude from $t = 0$ ms to $t = 1000$ ms.
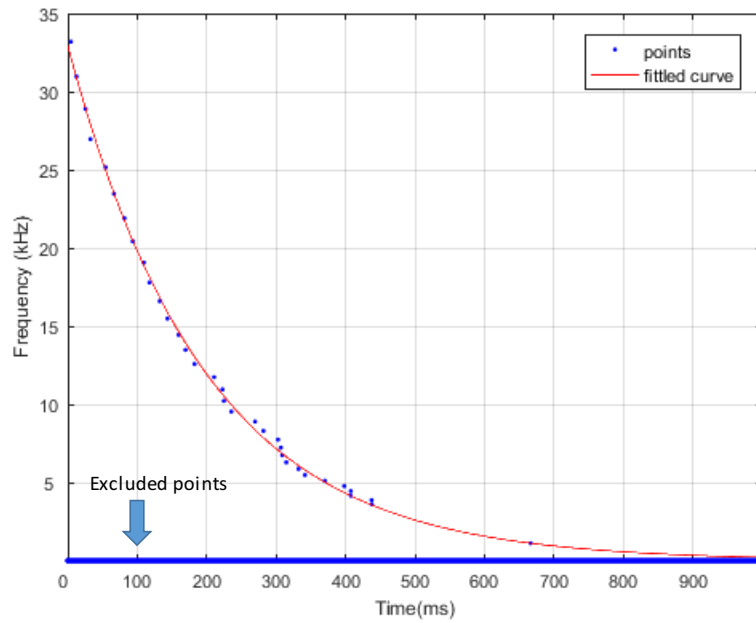


Figure 2.16. Curve-fitting result after excluding the other points

Now we have measured the dominating frequency and the slope of the decreasing trend, which are 443.6Hz and -4.69 respectively, where in our simulation the resonant frequency is 444Hz and the damping factor is -4.6. The measured results is very close to the value set for target vibration. It demonstrates that the resonant frequency and the damping factor of the external target can be simultaneously measured by SMI system. Hence, the measurement results from SMI system can be utilized for Young's modulus and internal friction calculation.

### 2.4.3  Results discussion

In the SMI system, the value of feedback level $C$ is very important to characterize the SMI signals. The SMI signals can be classified into three different regimes [73]. Regime 1 (weak feedback): where $C < 1$. In this situation, the vibration of external target results in the SMI signal waveform with a fringe structure similar to the traditional interference fringe and each fringe period corresponding to a phase shift equals to a displacement of half wavelength of the external target. Regime 2 (moderate feedback): where $1 \leq C < 4.6$. In this situation, the SMI signal of the external target vibration shows asymmetric hysteresis and produces sawtooth-like fringes. The slope of the fringe corresponding to the moving direction of the external target, where the a negative slope indicates the target moving toward the LD, and a positive slope indicates the target moving away from the LD. Regime 3 (strong feedback): where $4.6 \leq C$. In this situation, the SMI signal still shows asymmetric hysteresis and produces sawtooth-like fringes which is similar to Regime 2. However, there are some missing fringes, which is due to the strong hysteresis occurred while the feedback is strong. For the observation purpose, we assume the vibration of external target to be

$$y(t) = 3.925 \times 10^{-6} \cdot e^{-5t} \cos(2\pi(500t)) \qquad (2.54)$$

Where the vibraion frequency $f_{RO} = 500\,\text{Hz}$, damping factor $k = 5$. Figure 2.17 shows the corresponding normalised SMI signal with different feedback leve $C = 0.5, 3.8, 7$ and CWT coefficients, while $\alpha$ is set to be 6.
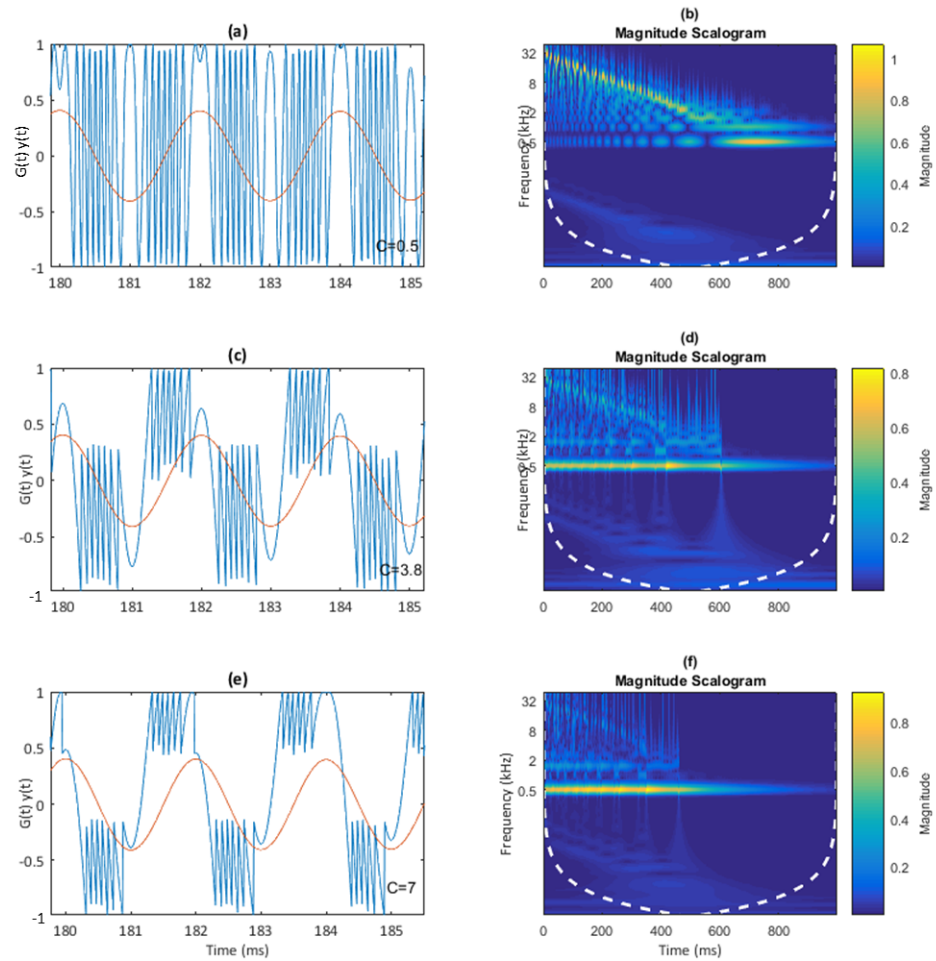
Figure 2.17. (a), (c), (e) normalised target vibration $y(t)$ with zoomed in corresponding SMI signal $G(t)$ when $C = 0.5, 3.8, 7$ , (b), (d), (f) CWT coefficient of SMI signal when $C = 0.5, 3.8, 7$

From section 2.3 we have already found that the fundamental frequency of SMI signal $G(t)$ is the same as the period of the vibration signal $y(t)$. In Figure 2.17, we can observe that the magnitude of this fundamental frequency is similar with the magnitude of fringe frequency when the SMI signal is in Regime 1, where $C < 1$. The magnitude of the fundamental frequency in SMI signal becomes larger and larger compare to the

53

magnitude of fringe frequency when the feedback level $C$ increases, shown in the Figure 2.17 (c) and (e), which is Regime 2 $C = 3.8$ and Regime 3 $C = 7$. This feature can also be found from the scolgram of CWT of SMI signals, where the magnitude of frequency around 500Hz getting larger with the yellow colour getting deeper, and the magnitude of high frequency component from around 32kHz to 1kHz getting smaller with the colour turning from yellow to blue. To demonstrate if the result from proposed method will be affect from the change of the feedback level $C$. We follow the same process as section 2.4.2. We first extract the fundamental frequency of SMI signal from the CWT scolgram, as shown in Figure 2.18. The extracted resonant frequency from the SMI signal is $f = 505.2$ Hz.

It is found that in Regime 1 where $C < 1$, the resonant frequency component is not the dominating frequency in SMI signal, where the magnitude of high frequencies is the same or larger than the magnitude of resonant frequency. In Regime 2 or 3, where $C > 1$, the resonant frequency is the dominating frequency in the SMI signal. It shows that the requirement for resonant frequency measurement from a SMI signal is to make sure the feedback level $C > 1$.

For the damping factor $k$ measurement, similar to the process in section 2.4.2, we can remove the low frequency component by zeroing out the CWT coefficients. Use the inverse CWT to reconstruct an approximation to the signal then get the new CWT coefficients of the reconstructed signal shown in Figure 2.19. After removing the low frequency affect, we can extract the frequency component with maximum magnitude at each time instance. Figure 2.20 shows the extraction from the scolgram and the curve-fitting result after eliminate other points. The curve fitting results for three SMI signals with different feedback level $C$ are $k_1 = 5.04$, $k_2 = 5.10$ and $k_3 = 5.06$ for $C = 0.5$, $C = 3.8$ and $C = 7$ respectively. It shows that the measurement of damping factor $k$ is feasible with the feedback level $C$ varies from weak feedback regime to strong feedback regime.
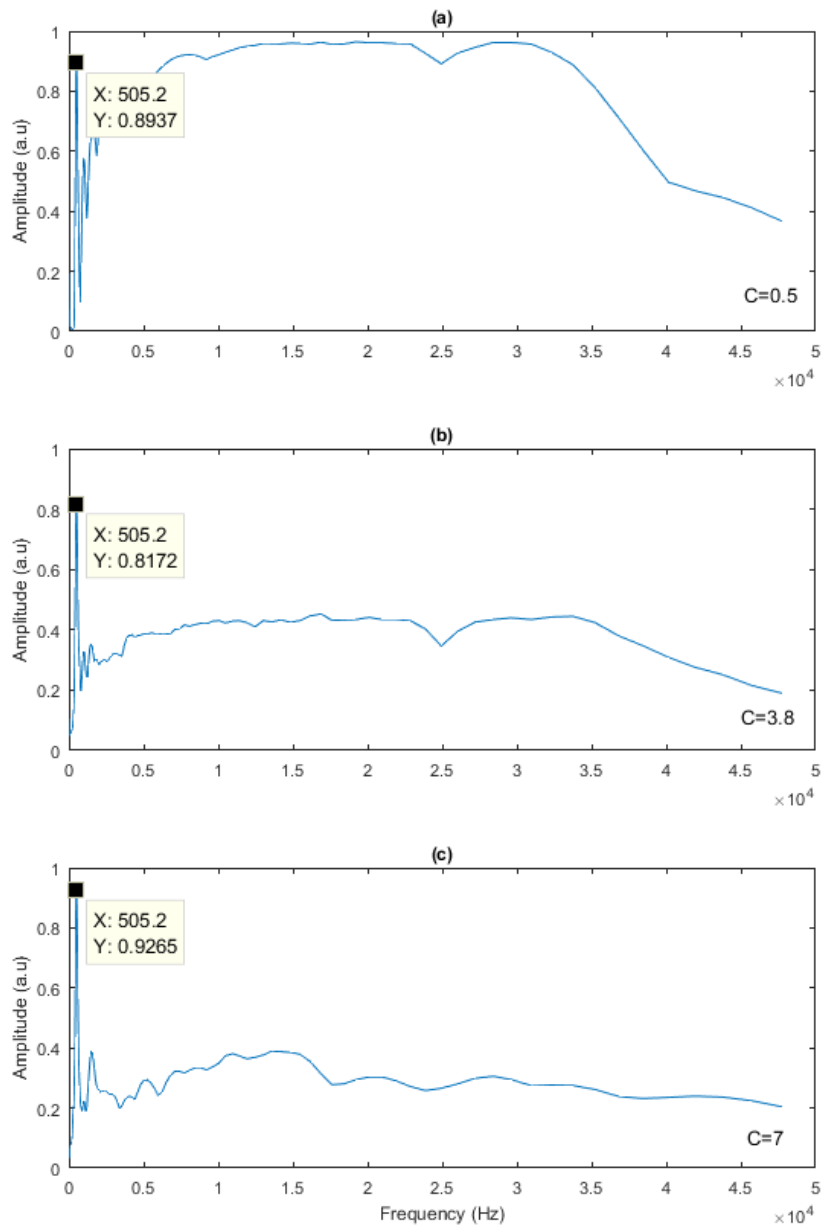
Figure 2.18. Extraction of resonant frequency from SMI signals with different feedback level, (a) $C = 0.5$ (b) $C = 3.8$, and (c) $C = 7$
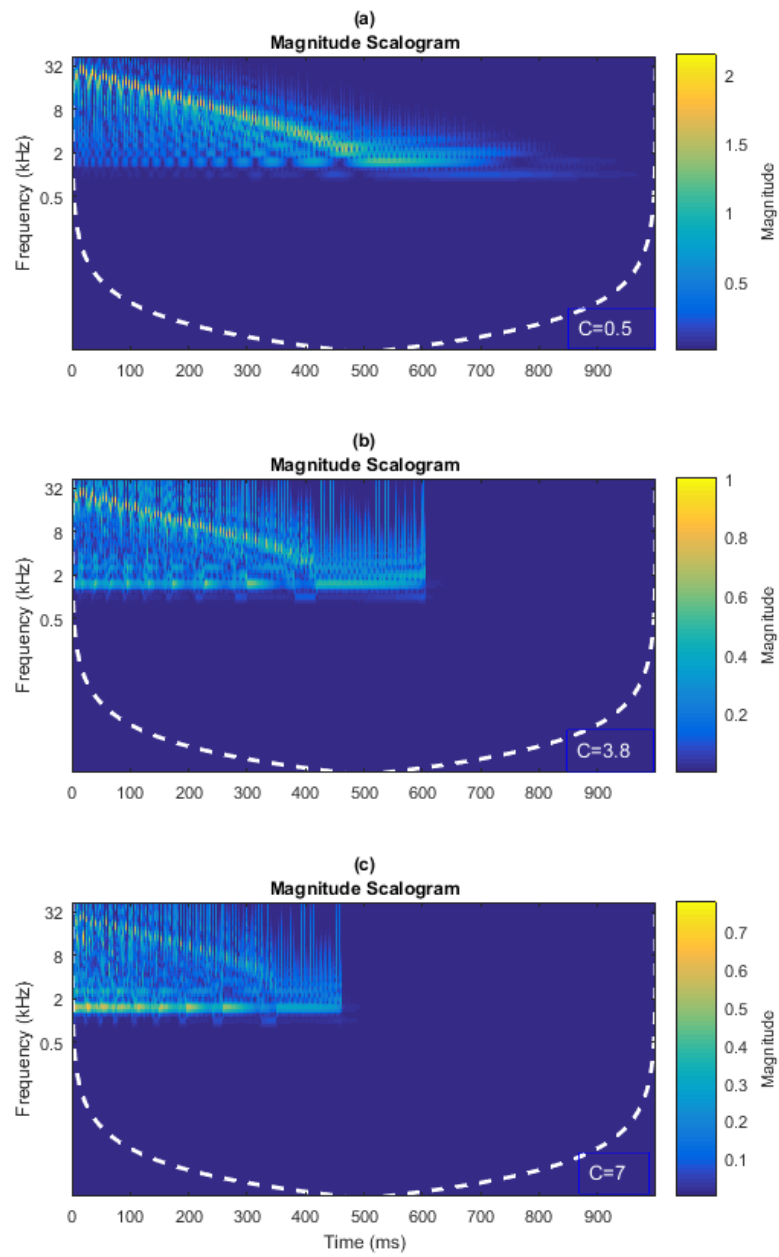
Figure 2.19. CWT of reconstructed SMI signal after zeroing out low frequencies, (a) $C = 0.5$, (b) $C = 3.8$, and (c) $C = 7$
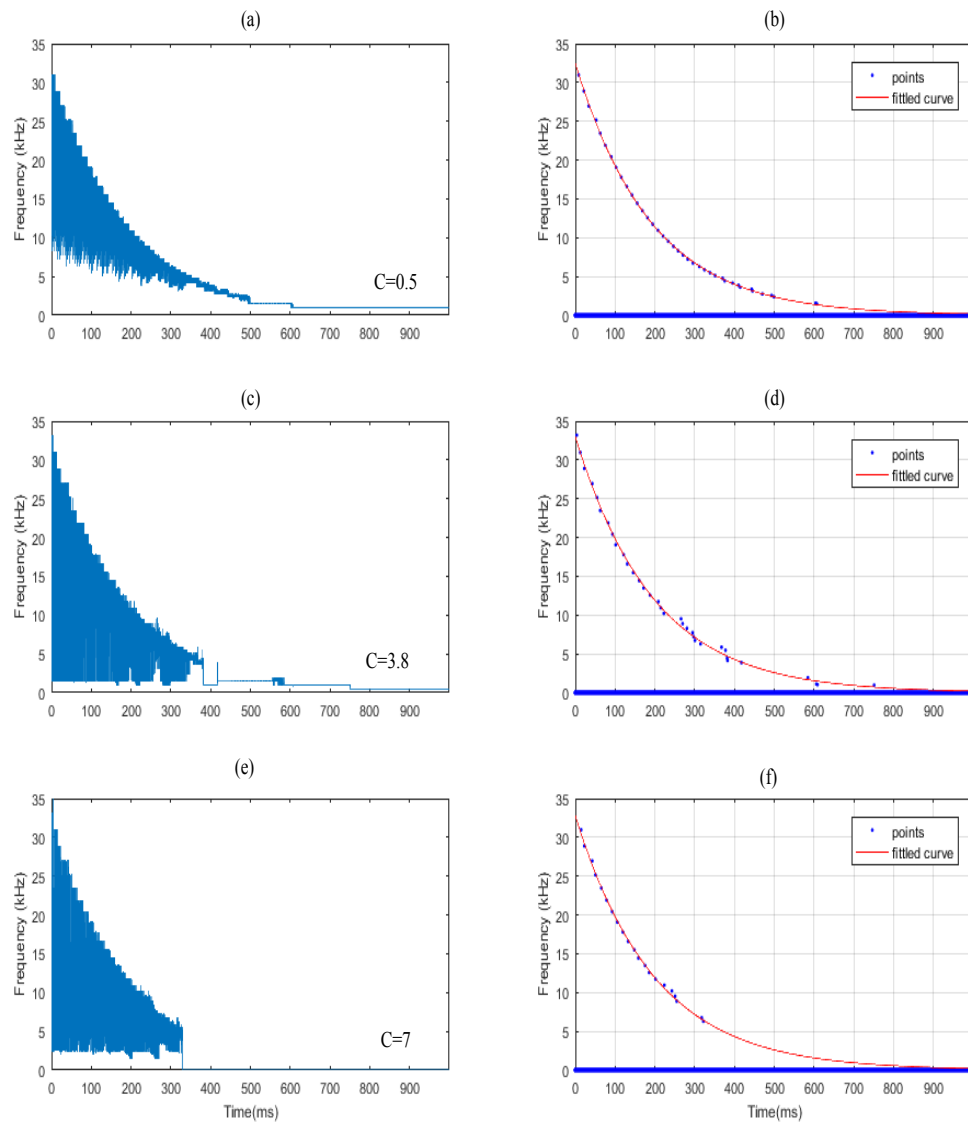
Figure 2.20. (a), (c), (e) Extraction of frequencies have maximum magnitude at each time instance, (b) (d) (f) curve-fitting results after excluding other points, where in (a) $C = 0.5$ , (b) $C = 3.8$ ,(c) $C = 7$

The proposed method is suitable for simultaneous measurement of material related parameters, resonant frequency $f_{RO}$ and damping factor $k$. Furthermore, the fringe

counting method for damping factor measurement described in [119] is compared with the proposed method and the results are shown in table 2.4.

Table 2.3. Comparison of measurement results of proposed method with method in [119]

| Simulation value $k = 5$ and $f_{RO} = 500\,\mathrm{Hz}$ | | Method in [119] | | Proposed method | |
|---|---|---|---|---|---|
| | | Damping factor $k$ | Resonant frequency $f_{RO}$ (Hz) | Damping factor $k$ | Resonant frequency $f_{RO}$ (Hz) |
| $C < 1$ | $C = 0.01$ | 5.02 | N/A | 5.12 | N/A |
| | $C = 0.1$ | 5.04 | N/A | 5.13 | N/A |
| | $C = 0.2$ | 5.09 | N/A | 5.09 | N/A |
| | $C = 0.3$ | 5.14 | N/A | 5.10 | N/A |
| $1 \le C < 4.6$ | $C = 2$ | N/A | N/A | 5.04 | 505.2 |
| | $C = 2.5$ | N/A | N/A | 5.08 | 505.2 |
| | $C = 3$ | N/A | N/A | 5.06 | 505.2 |
| | $C = 4$ | N/A | N/A | 5.12 | 505.2 |
| $4.6 \le C$ | $C = 5$ | N/A | N/A | 5.15 | 505.2 |
| | $C = 6$ | N/A | N/A | 5.14 | 505.2 |
| | $C = 7$ | N/A | N/A | 5.06 | 505.2 |
| | $C = 9$ | N/A | N/A | 4.96 | 505.2 |

From the table 2.4, it can be seen that the method in [119] can only measure the damping factor $k$ when $C < 1$, and it cannot measure the resonant frequency $f_{RO}$. The proposed method gives reliable measurement results for both damping factor and resonant frequency in a broad range of $C$. In fact, the feedback level $C$ affects the reverse point in the SMI signal, which causes the error of damping factor. Also, according to the equation (2.45), the larger $C$ leads to larger phase shift between $\phi_s$ and $\phi_0$. This is why fringe counting method in [119] only works when $C$ is very small (close to 0). In

the proposed method, where we measure the damping factor based on the decrease of fringe frequencies, even with larger $C$ we can use the wavelet transform to zeroing out the dominating frequency in the SMI signal then extract the high frequency components for the damping factor measurement. When $C$ is larger than 1, we can also extract the target resonant frequency from the real part of the wavelet transform coefficients. By applying wavelet transform, both resonant frequency and damping factor of the target vibration can be obtained at the same time, from which, we can calculate the material related parameters such as Young's modulus and internal friction. The C should be chosen within the range between 1 and 4.6, where it is in the moderate feedback regime [121], for the Young's modulus and internal friction measurement.

In practical, the feedback level $C$ relates to the reflectivity of the target surface, variable attenuator, and external cavity length. To maintain the feasibility of the simultaneous measurement, $C$ can be controlled to be larger than 1 by adjusting the related variables.

## 2.5    Summary

This chapter presents the measurement principle including SMI generation, wavelet transform onto SMI signal to retrieve the material parameters to be measured. Firstly, section 2.2.1 presents the specimen vibration model. The mode of vibration depends on the support locations on the specimen. When $n = 1$, $\beta_1 L = 4.73$ with the support locations at $0.224L$ from each end, the specimen can only vibrates in the first mode. The damping vibration of the specimen is $y(t) = A_0 e^{-kt} \cos(2\pi f_{RO} t)$ after removing the external force. The Young's modulus $E$ can be calculated by knowing the resonant frequency $f_{RO}$, and the internal friction $Q^{-1}$ can be calculated by knowing both resonant frequency $f_{RO}$ and damping factor $k$. The signal detection part, SMI model, is introduced in section 2.2.2 with the analysis of its mathematical, the derivation of existing SMI model from LK equations. The relationship between the SMI signal and the material related parameters is presented

in section 2.3. It is found that the resonant frequency can be retrieved from the dominating frequency in the SMI signal and the damping information is also obtained in the SMI where the decrease of fringe numbers indicates the decay of vibration magnitude. Section 2.4 is the process of retrieving the vibration information from a SMI signal. The wavelet transform is introduced as it shows better results than Fourier transform in time-frequency analyse. From the scalgram of wavelet transform on SMI signal, both dominating frequency component and the fringe frequencies can be extracted separately. The results show that the resonant frequency and damping factor can be simultaneously measured by the proposed method. In section 2.4, we discuss the measurement results, It is found that the SMI signal needs to work in the moderate or strong feedback regime to measure the resonant frequency, where the damping factor can be measured in different regimes from weak feedback level to strong feedback level. The proposed method is compared with the method in [119]. The proposed method is better because the SMI system can work in a larger range of feedback level and both resonant frequency and damping factor can be retrieved.

# Chapter 3  Implementation of the SMI measurement system

In chapter 2, the specimen vibration model and the SMI model are analysed. The relationship between Young's modulus and internal friction and target vibration is also presented. The wavelet transform method for retrieving material related parameters from a SMI signal and the results are discussed.

This chapter presents the experimental measurement system. The design for both IET part and SMI part are presented. The selection of every component in each part is detailed. The optical fibre is installed into the system. The experiment is conducted for both SMI system without and with fibre.

## 3.1  System structure

As it is mentioned in Chapter 2, the system structure for the experiment can be separated into two parts, IET part and SMI part. The IET part is to generate the damping vibration of the specimen and the SMI part is to generate the corresponding SMI signal and to be processed to retrieve the material related parameters of the specimen. The overall system is shown in Figure 3.1.

This chapter presents the system description. The system model is presented separately with specimen vibration model and SMI model. The relationship between the SMI signal and the material related parameters is discussed. The wavelet transform is

applied onto the SMI signal to retrieve the material related parameters. The results of using wavelet transform to analysis SMI signal are discussed.
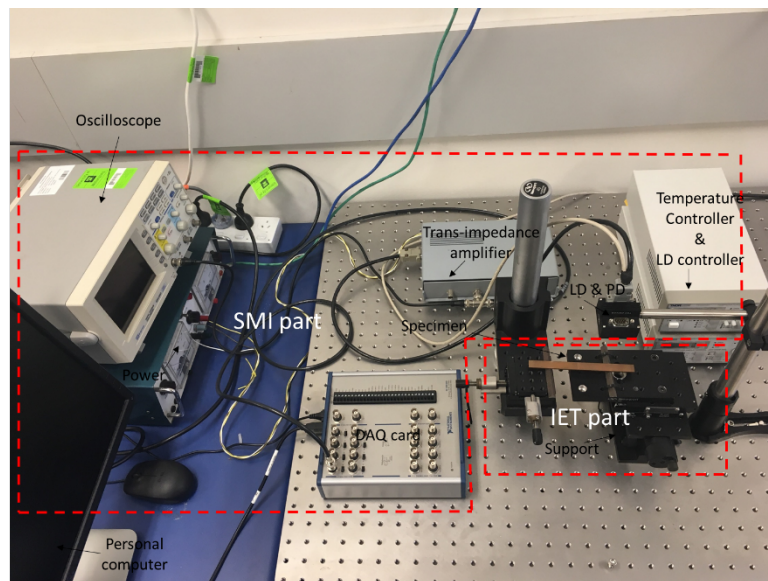


Figure 3.1. Schematic measuring system

The IET part contains three components: specimen, support and stimulation tool. The specimen shall be prepared to be rectangular in the cross section with a proper geometry. The dimensions of the specimen should be selected based on the relationship that the resonant frequency are functions of specimen dimensions. The support for the specimen should isolate the specimen from extraneous vibration without restricting the desired mode of specimen vibration. The materials of the support can be soft or rigid for ambient conditions. For the rigid materials, such as metal or ceramic, should have sharp edges or cylindrical surface where the specimen rest on. The specimen should be supported appropriately along the node lines for the desired vibration. A stimulation tool is utilised for producing the exciting impulse by striking the specimen. The stimulation tool should have the most of its mass concentrated at the point of impact and have mass sufficient to induce a measurable mechanical vibration for the measuring system but not too large as to displace or damage the specimen physically. The main purpose of the IET part is to produce the desired vibration so that it can be picked up by the SMI system.

The SMI part is the core part in the whole system. It provides a medium for carrying the desired vibration information from the specimen. The SMI part need to be designed elaborately to achieve a stable SMI signal as well as suitable the feedback level for the resonant frequency and damping factor measurement. The main SMI part consists of a LD, PD, LD controller, and temperature controller. When the specimen is stimulated into vibration, a small portion of light will be reflected by the specimen and re-enter the LD, which is controlled by the LD controller and temperature controller. The laser intensity emitted by the LD will be modulated by the specimen's vibration. The modulated laser intensity is treated as SMI signal, which can be detected by a PD packaged in the rear of the LD. The other SMI part includes three components: the trans-impedance amplifier, data acquisition card, oscilloscope and a personal computer. The trans-impedance amplifier is to transform the current signal from PD to voltage signal and have it amplified for data processing. Data acquisition is the process of sampling the signal from the trans-impedance amplifier and converting the samples into digital signal. This digital signal will be displaced on the screen of the oscilloscope. A personal computer will also be used for the signal processing, in this thesis the wavelet transform will be applied onto the signal to retrieve the resonant frequency and damping factor of the specimen.

The procedure of these three parts in the system is from generating vibration signal to picking up the vibration signal and generating SMI signal to finally analysing the SMI signal to retrieve the vibration information. The following section will present the design of these parts in the system.

## 3.2    System design

### 3.2.1  IET part

• Specimen preparation

The mechanical part design is based on IET. The relationship between resonant frequency and Young's modulus in this technique is specifically appropriate for materials

that are elastic, homogeneous and isotropic [29]. For the composite and inhomogeneous materials, the effect of inhomogeneities and anisotropy need to be carefully considered. The volume fraction, size , moraphology, distribution, orientation, elastic properties and interfacial bonding of the reinforcement and inhomogeneities in the specimens can have a direct effect on the Young's modulus of the specimen. The surface treatments such as coating and grinding can also change the elastic properties of the near-surface materials, which causes accentuated effects for the Young's modulus measurement from IET.

In the measurement system based on IET, equation (2.28) has described the relationship between Young's modulus and specimen's resonant frequency, dimensions and mass, which is rewritten as below

$$E = 0.9465 \cdot \frac{m f_{RO}^2 l^3}{b h^3} \cdot T \qquad (3.1)$$

There are several requirements to satisfy this analytical equation.

➢ The dimensions and mass of the specimen must be regular as for a rectangular specimen must be parallelepiped.

➢ The specimen for the test should not have chamfered or rounded edges as the edge treatments can introduce error into the determination of the resonant frequency of the specimen.

➢ The surface of the specimen should be even and smooth otherwise it can cause significant effect in the calculation. It can be seen that the Young's modulus is inversely proportional to the thickness of the specimen in the equation.

➢ The length of the specimen need to be 20 times or more longer than the thickness for the rectification of the correction factor, while when $l \leq 20h$

$$T = 1 + 6.585(1 + 0.075\mu + 0.8109\mu^2)(h/l)^2 - 0.868(h/l)^4$$
$$- \left[ \frac{8.340(1 + 0.2023\mu + 2.173\mu^2)(h/l)^4}{1.000 + 6.338(1 + 0.1408\mu + 1.536\mu^2)(h/l)^2} \right] \qquad , \mu \text{ is the Poisson's}$$

ratio need to be predetermined, when $l \geq 20h$, $T = \left[ 1.000 + 6.585(h/l)^2 \right]^2$ and the Young's modulus can be calculated directly without the pre-

knowledge of Poisson's ratio.

The specimen to be tested in this experiment is a rectangular shaped brass bar with the $l = 138.10$ mm, $b = 12.01$ mm, $h = 2.08$ mm and $m = 29.84$ g. Figure 3.2 shows the picture of the specimen.
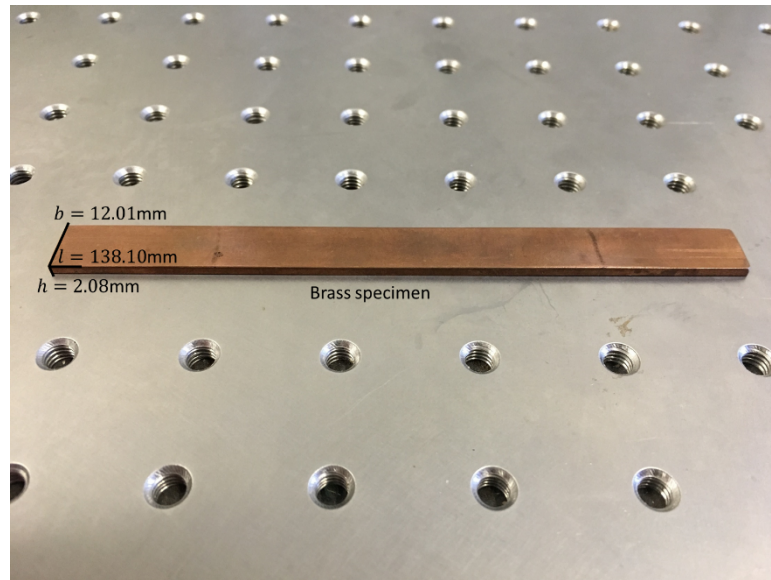


Figure 3.2. Brass specimen

- Supporting device

Supporting device is important in IET as it should be capable of supporting the specimen in the correct position so that the vibration of the location on the specimen is detectable for SMI system, and that the extraneous vibration is negligible compare to the vibration from the specimen. In addition, the supporting points should be adjustable to obtain the desired vibration mode.

As it was discussed in section 2.2.1, in mode 1, where $n = 1$, $\beta_1 L = 4.73$, the specimen vibration is at the lowest resonant frequency . The nodes are located at $0.224l$ from each end of the specimen, which means that these two points have minimum amplitude 0 and the centre and two ends have the maximum amplitude as shown in Figure 3.3. The laser beam from SMI system will focus on the anti-node point to maximum the measurement performance.
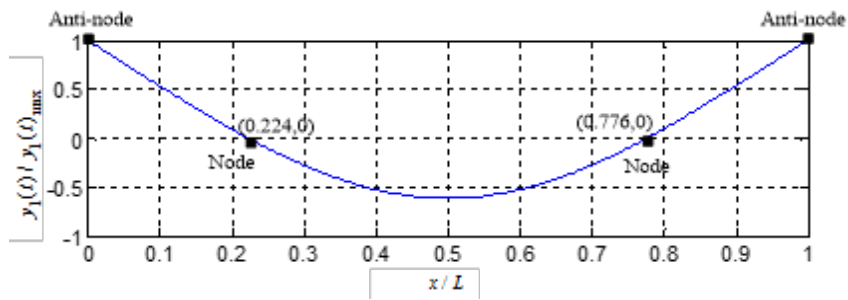
Figure 3.3. Normalized mode 1 vibration of a free-free rectangular specimen

In our experiment, the platform for support is Newport 426 series extended platform with crossed-roller bearings. Two triangular prism are placed and fixed on the platform. Figure 3.4 shows the vertical and horizontal views of the support device. The left side platform can be adjusted laterally to locate the node points on the specimen. The right side platform can be adjusted vertically to alter the cavity length for the SMI system, so that makes it applicable of focusing the laser beam and varying the feedback level. The whole support device is immobilized onto a pneumatized vibration isolation table to exclude the undesirable vibration interference.
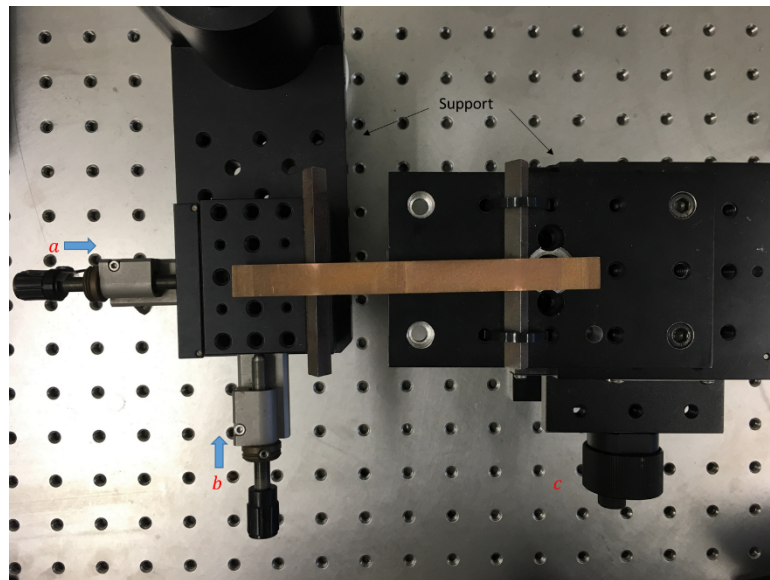


(a)
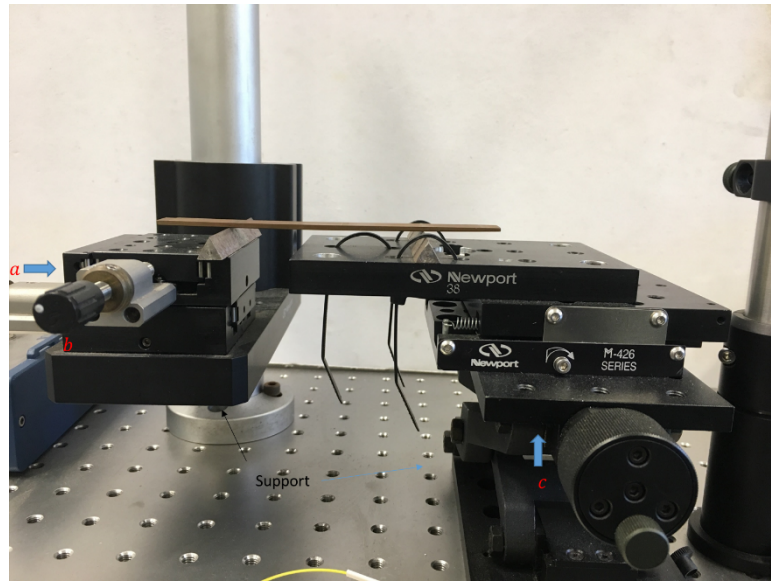
(b)

Figure 3.4. (a) Vertical view of the support system and (b) horizontal view of the support system, where a and b bearings are for lateral adjustment, and c is for vertical adjustment.

- Excitation generation

A stimulation tool is an equipment that applies an impact on the specimen to generate the desired vibration without damaging it. It can be a polymer stick with a steel ball glued to one end of it. For commonly tested geometries, the size of the steel ball would be 0.5cm in diameter and the length of polymer rod would be 10cm [28]. Figure 3.5 shows the stimulation tool used in the experiment.
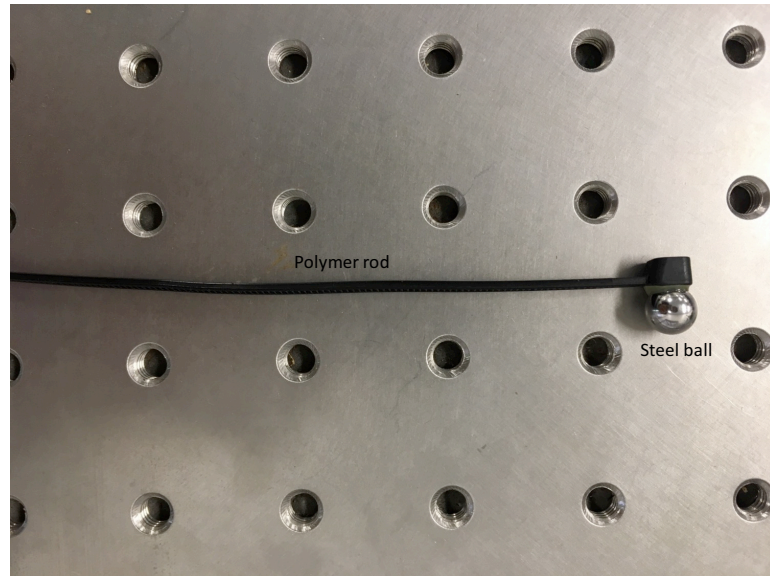
Figure 3.5. Stimulation tool

The stimulation tool in the experiment is a polymer stick with a steel ball glued to one end of it. The impulsive force is applied through the steel ball at the centre of the specimen. The force can be transferred from vertical direction while the force act on the horizontal direction can be neglected. Due to the elastic property of the material, the deflection of each end of on the specimen will be maximum at initial time. The specimen together with the support device can be treated as a simply supported beam. The bending moment and shear force distributions can be calculated along the beam by using the free body diagram technique. The function block diagram (FBD) of a simply supported beam is shown in Figure 3.6
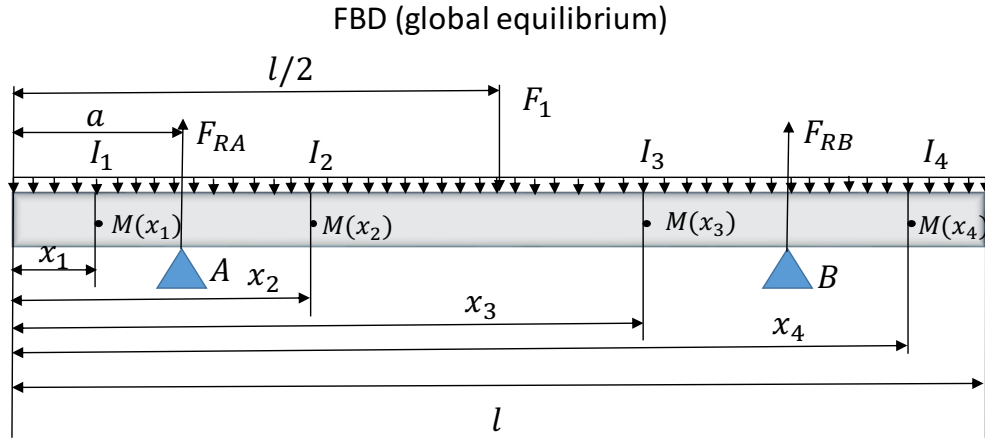
Figure 3.6. FBD of a simply supported beam

Equate the equilibrium of the whole beam from the vertical equilibrium, we can get

$$+\uparrow \sum F_{Ay} = F_I + ql - F_{RA} - F_{RB} = 0 \tag{3.2}$$

Taking the moments of points at support $A$:

$$\sum M_A = qa \cdot \frac{a}{2} + F_{RB}(l - 2a) - F_I(\frac{l}{2} - a) - \frac{1}{2}q(l-a)^2 = 0 \tag{3.3}$$

Gives

$$F_{RA} = F_{RB} = (ql + F_I)/2 \tag{3.4}$$

Where $q = m_b g/l_b$, $m_b$, $g$ and $l_b$ are the mass, gravitational acceleration, and the length of the beam respectively. $F_{RA}$ and $F_{RB}$ are the ground reactions on $A$ point and $B$ point respectively.

The beam is cut into four separate portions as indicated by $I_1, I_2, I_3, I_4$. The equation of bending moments for each separate portion can be determined as below.

$$M(x_1) = -\frac{q}{2}x_1^2 \, (0 \le x_1 \le a) \tag{3.5}$$

$$M(x_2) = -\frac{q}{2}x_2^2 + \frac{F_1 + ql}{2}x_2 - \frac{(F_1 + ql)a}{2} \, (a \le x_2 \le \frac{l}{2}) \tag{3.6}$$

$$M(x_3) = -\frac{q}{2}x_3^2 + \frac{ql - F_1}{2}x_3 + \frac{F_1 l - (F_1 + ql)a}{2} \, (\frac{l}{2} \le x_3 \le l - a) \tag{3.7}$$

$$M(x_4) = -\frac{q}{2}x_4^2 + qlx_4 + \frac{ql^2}{2}(l - a \le x_4 \le l) \tag{3.8}$$

These bending moments' equations of the specimen can be utilised to determine the vibration of the reference point on the specimen. The deflection equation of the specimen is shown as below

$$\frac{d^2w}{dx^2} = \frac{M}{EI_z} \tag{3.9}$$

Where $w$ is the deflection curve of the beam, $E$ is the Young's modulus, and $I_z$ is the inertia moment of the beam. $EI_z$ is constant for a straight beam. Then equation (3.9) can be rewritten as

$$EI_z w'' = M(x) \tag{3.10}$$

After first order integration

$$EI_z \theta = EI_z w' = \int M(x)dx + C \tag{3.11}$$

Where $\theta$ is the rotation angle while the beam is under pressure.

After second order integration

$$EI_z y = EI_z w = \int(\int M(x)dx)dx + Cx + D \tag{3.12}$$

The equation (3.10) to (3.12) can be utilised to determine the initial deflection of the reference point, which located on the left side of at portion $I_1$ on the specimen. The equation of the deflection curve of the portion $I_1$ can be calculated as

$$M(x_1) = EI_z w_1'' = -\frac{q}{2}x_1^2 \tag{3.13}$$

$$EI_z \theta_1 = EI_z w_1' = -\frac{q}{6}x_1^3 + C_1 \tag{3.14}$$

$$EI_z y_1 = EI_z w_1 = -\frac{q}{24}x_1^4 + C_1 x_1 + D_1 \tag{3.15}$$

Similar to portion $I_1$, we can also get the equations for portion $I_2, I_3, I_4$, which all have the corresponding unknown parameters $C_2, D_2, C_3, D_3, C_4, D_4$. The eight boundary conditions are required to solve the equations. $C_1$ and $D_1$ can be solved as

$$C_1 = \frac{1}{4}F_1al - \frac{1}{16}F_1l^2 - \frac{1}{24}ql^3 - \frac{1}{4}F_1a^2 + \frac{1}{4}aql^2 - \frac{1}{8}a^2 \qquad (3.16)$$

$$D_1 = \frac{1}{24}qa^4 + \frac{1}{4}a^3ql + \frac{1}{4}F_1a^3 - \frac{1}{4}a^2ql^2 - \frac{1}{4}F_1a^2l + \frac{1}{24}qal^3 + \frac{1}{16}F_1al^2 \qquad (3.17)$$

Substituting equation (3.16) and (3.17) into equation (3.15)

$$EI_z y_1 = -\frac{q}{24}x_1^4 + (\frac{1}{4}F_1al - \frac{1}{16}F_1l^2 - \frac{1}{24}ql^3 - \frac{1}{4}F_1a^2 + \frac{1}{4}aql^2 - \frac{1}{8}a^2)x_1$$
$$+ \frac{1}{24}qa^4 + \frac{1}{4}a^3ql + \frac{1}{4}F_1a^3 - \frac{1}{4}a^2ql^2 - \frac{1}{4}F_1a^2l + \frac{1}{24}qal^3 + \frac{1}{16}F_1a \qquad (3.18)$$

The specimen used in the experiment is a brass bar with the $l = 138.01$ mm, $b = 12.01$ mm, $h = 2.08$ mm and $m = 29.05$ g, the density is $\rho = 8.43$ mg/mm$^3$. $q$ and $a$ can be calculated by $q = mg/l = 233.02$g/m and $a = 0.224l = 30.93$ mm. When there is no impact on the specimen ($F_1 = 0$), the deflection of the reference point on the specimen in rest is $y_{rest} = -10.30$ μm. The resolution of the SMI is half of the wavelength, which is $655/2 = 327.5$ nm. The initial vibration magnitude must be larger than 327.5nm, so $y_1 > -9.97$ μm. From equation (3.18) we can get $F_1 > 0.016$N. The force of a falling ball can be calculated as $F = \frac{m_{ball}V_{ball}}{t} + m_{ball}g$, where $V_{ball} = \sqrt{2gh}$. For a steel ball with 0.5cm diameter and 7.85g/cm$^3$ density , $m_{ball} = 0.5$g, falling from 50cm high, $h = 0.5$ m, the duration of time that equivalent average force was acting is 0.001s, $t = 0.001$s, it can generate a force $F = 0.16$ N, which is much larger than 0.016N. In practice, it only needs a very small impulse from the stimulation tool then the initial vibration magnitude of the reference point will be much larger than 327.5nm.

### 3.2.2  SMI part

- Laser diode and photodiode

In design of the optical part, the performance of the LD is highly related to the system sensing performance. The LD model used in the experiment is RLD65MZT2. It is single mode with optimized strained multi quantum well and suitable for DVD-ROM,

combination drive and sensors. It shows good temperature characteristic and has low threshold current. Table 3.1 shows the electrical and optical characteristics of it. Figure 3.7 shows the electrical and optical characteristics curve.

Table 3.1. Optical and electrical characteristics of RLD65MZT2 [120]

| Parameter | Min | Typ | Max | Conditions |
|---|---|---|---|---|
| Threshold current ($I_{th}, mA$) | - | 25 | 60 | - |
| Operating current ($I_{op}, mA$) | - | 35 | 70 | $P_0 = 5mW$ |
| Operating voltage ($V_{op}, V$) | - | 2.3 | 2.6 | $P_0 = 5mW$ |
| Differential efficiency ($\eta, mW/mA$) | 0.2 | 0.4 | 0.8 | - |
| Monitor current ($I_m, mA$) | 0.1 | 0.2 | 0.5 | $P_0 = 5mW$ |
| Peak emission wavelength ($\lambda, nm$) | 645 | 655 | 660 | $P_0 = 5mW$ |
| Astigmatism ($A_S, \mu m$) | - | - | 10 | $P_0 = 5mW$ |
| Operating temperature ($^0C$) | -40 | - | +85 | - |
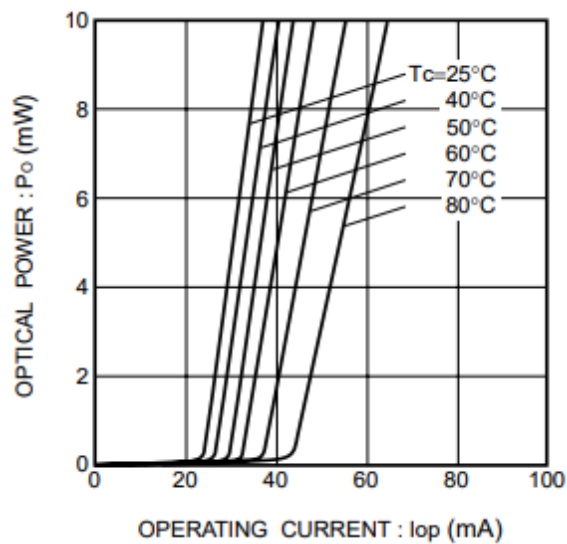
Figure 3.7. Optical output vs. operating current at different temperature.

It can be seen the ratio between operating current and optical power is maximalised when the temperature is at $25\,^{0}C$. A temperature controller can be applied to control the temperature in this value.

The PD is packaged at the rear of the laser diode to convert the light to current under photodiode mode. The pin diagram for the equivalent circuit of signal converting is shown in Figure 3.8.



Figure 3.8. Structure of RLD65MZT2 and its equivalent circuit pin diagram

Laser mount LDM21 is utilised to operate the LD. The laser installation is conducted by determining the laser pin configuration from the RLD65MZT2 manufacturer's data sheets (shown in Figure 3.7) and set the LD and PD switches located on the inside of the laser mount according to the polarity switch settings from the user guide of laser mount. After installing the LD into the laser mount, a collimating optics is necessary due to the highly divergent output of the LD. Aspheric lenses are the most commonly used optics owing to its excellent ability to correct spherical aberration. Normally, the collimated beam waist is desired to be between one and five millimetres. The aspheric lens C240TME-B is installed at the front of the laser mount. Figure 3.9 shows the laser mount after installing LD and lens.
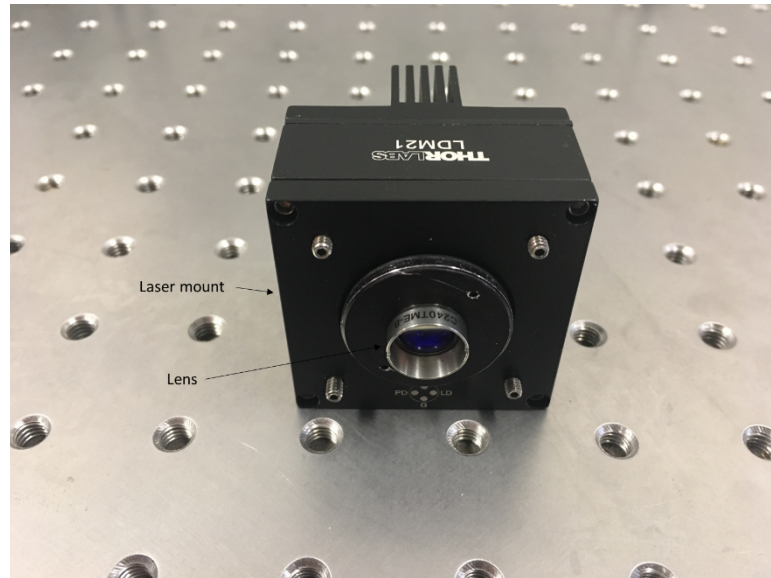
Figure 3.9. Laser mount after installing the LD and lens


- Laser controllers

It is important to use laser controllers to stabilize the operation of the LD as the injection current and temperature can significantly affect the laser performance. The LDC205C LD controller and TED200C temperature controller are chosen to control the LD shown in Figure 3.10. The LDC205C is part of Thorlabs LDC200C series, which are high accuracy precise injection current for LD. The TED200C temperature controller is a precise temperature controller, which is suitable for wavelength stabilization of LD. Together with a LDC205C LD controller a stable operation of the connected laser diode can be achieved.

Figure 3.10. LD controller and temperature controller

For the sensing application, it is desired that the SMI system operates in a stable mode. The SMI signal shows sinusoidal-like or sawtooth-like fringes depending on the feedback level $C$ as it is mentioned in section 2.4.3. However, the stability of the SMI is affected by the operational conditions, such as injection current and the external cavity length [121]. The stable condition for a LD with an external target was derived from LK equations in [101]

$$-\alpha\kappa\sin(\phi_s)+\kappa\cos(\phi_s)\left[1-2\left(\frac{\Omega}{\omega_R}\right)^2\right]<\left(\frac{\Omega}{\omega_R}\right)^2\frac{\tau_{in}}{2\tau_R\sin^2(\Omega\tau/2)} \qquad (3.19)$$

Where $\Omega$ is defined as the imaginary part for a complex number in Laplace transform domain, which satisfies

$$\Omega^2-\omega_R^2=\frac{\Omega}{\tau_R}\cot(\frac{\Omega\tau}{2}) \qquad (3.20)$$

Where

$$\omega_R=\sqrt{\frac{G_N}{\tau_p}}E_{s0}, \frac{1}{\tau_R}=\frac{1}{\tau_s}+\left(\tau_p+\frac{\varepsilon\Gamma}{G_N}\right)\omega_R^2 \qquad (3.21)$$

$E_{s0}$ is the stationary electric field amplitude of the solitary laser, which is determined by the injection current $J$. $\omega_R$ and $\tau_R$ are the relaxation oscillation frequency and the

damping time of the solitary laser. The other parameters were previously defined in section 2.2.2. The external cavity round trip time $\tau$ is determined by the external cavity length $L$, where $\tau = 2L/c$. We can replace $\kappa$ by $C$ (via $C = \dfrac{\kappa}{\tau_{in}} \tau \sqrt{1+\alpha^2}$ ) to explore the stable boundary for the feedback level $C$. Then stable condition in equation (3.19) can be rewritten as

$$C\left\{\cos(\phi_s)\left[1-2\left(\frac{\Omega}{\omega_R}\right)^2\right]-\alpha\sin(\phi_s)\right\} < \left(\frac{\Omega}{\omega_R}\right)^2 \frac{\tau\sqrt{1+\alpha^2}}{2\tau_R\sin^2(\Omega\tau/2)} \qquad (3.22)$$

Where $\alpha$ is normally treated as constant, $\phi_s$ is related to $\phi_0$ from equation (2.40), both $\omega_R$ and $\tau_R$ are dependent on the injection current $J$ via $E_{s0}$ in equation (3.21), $\Omega$ is related to both $J$ and $\tau$. Hence, the injection current $J$ and the external cavity round trip time $\tau$ are two governing parameters that determine the stable condition of the SMI system described by feedback level $C$. The influence of injection current and external cavity length on feedback level were investigated in the literature [121]. Figure 3.11 shows the relationship between an estimated value of critical feedback level, the injection current and external cavity length.
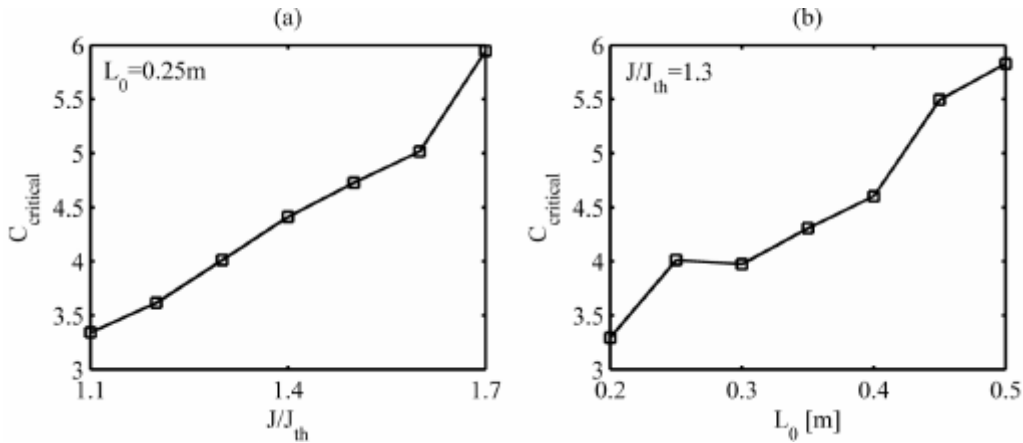


Figure 3.11. Value of critical feedback level $C_{citical}$ (a) for a fixed external cavity length $L_0 = 0.25$ m, (b) for a fixed injection current $J/J_{th} = 1.3$ [121].

As it was discussed in section 2.4.3, the requirement of Young's modulus

measurement is to make sure the SMI system operates in a moderate or strong feedback level regime. From the figure 3.11, it can be seen that the feedback level can be increased by either increasing the injection current for a fixed external length or increasing the external cavity length for a fixed injection current. In practise, this is not hard to achieve as we can adjust both parameters in a suitable range.

- Trans-impedance circuits

The current signal acquired through PD is not suitable for the data processing purpose. Hence, the trans-impedance circuits can be applied to transfer the current signal from PD to voltage signal and have it amplified. The voltage signal can be generated through using a resister realizing the process of trans-impedance.

In SMI signal, the fringe frequencies varies fast along the time so that an AC amplifying module is need. A high-pass filter circuit is designed to solve the problem as well as preventing the distortion in SMI signal. A mean filtering can be used for de-noise. Figure 3.12 shows the scheme of the high-pass filtering circuit and the physical designed amplifier circuits.
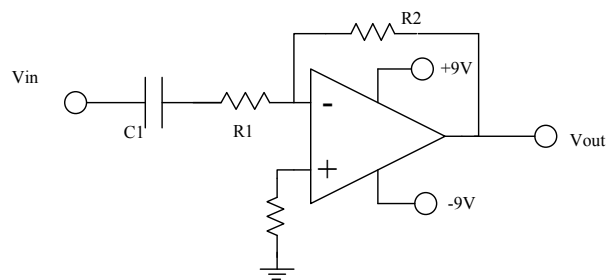


(a)
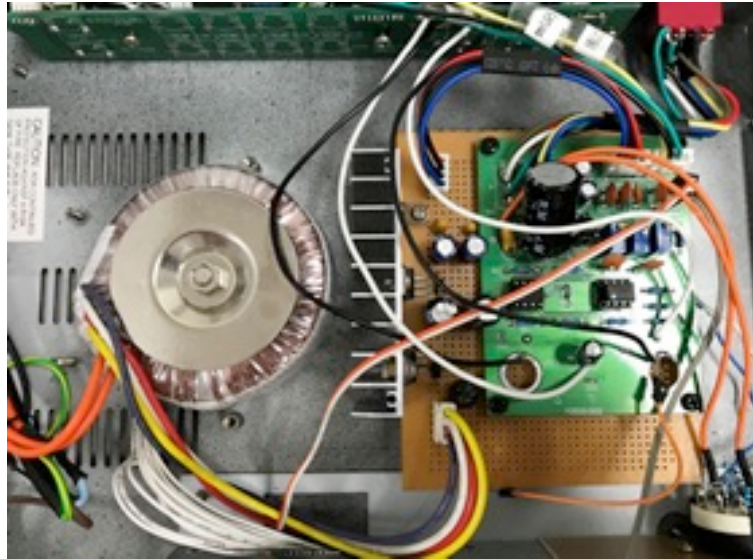
(b)

Figure 3.12. (a) High pass filtering circuit scheme. (b) The physical designed amplifier circuits.

- Signal acquisition and processing

The current signal passes through the trans-impedance circuits to become a voltage signal and be amplified. The voltage signal must be converted into digital signal before it is analysed by digital equipment such as a computer. The analog-to-digital converter can provide a digital representation of an analog signal at an instant time. In practice, analog signal continuously varies over time and the analog-to-digital converter takes periodic samples of the signal at a predefined rate. These samples are transferred to computer where the original signal is reconstructed. A DAQ card NI USB-6361 from national instruments, where the analog input resolution is 16 bits and the sampling rate is 200kHz, is used in the experiment shown in figure 3.13. It is suited for a broad range of applications, from basic data logging to control and test automation.

Figure 3.13. NI USB-6361 DAQ card

After sampling the signal through DAQ card, a private computer is utilised to display the sampled signal and for further signal processing through the software installed in the computer. Alternatively, we can use an oscilloscope to display the signal and observe the features. The overall system with IET part and SMI part is shown in Figure 3.1.

### 3.2.3 Fibre coupled SMI system

• Fibre optics overview

The history of fibre can go back to Roman times, when the glass was drawn into fibres. The development of fibres did not have much progress for centuries. Until 17$^{th}$ century, the French invented the first 'optical telegraph', a system that comprised of a series of lights mounted on towers where operators would send messages from one tower to the other. Great strides were made over the next century. In the 1840s, the physicists Daniel Collodon and Jacques Babinet discovered that light could be directed along jets of water for fountain displays. Heinrich Lamm first found to transmit an image through a bundle of

optical fibres in 1930s. Later a cladded fibre system was invented to greatly reduce the signal interference and crosstalk between fibres. In the same year, the 'maser' stands for 'microwave amplification by stimulated emission of radiation' was developed. Laser was first introduced as an efficient source of light in 1958. It was found that 'maser' could be made to operate in optical and infrared regions. A theoretical description of single mode fibres whose core would be small enough to carry light with only one wave-guide mode was published. Later, it was found that the light loss in glass fibres could be decreased by removing impurities. After many years of development on fibre, the first all-optic fibre cable was laid across the Pacific Ocean in 1996. Now, a broad range of applications such as medical, military, telecommunication and sensing are able to use fibre optic.

Many kinds of fibre optic sensing systems using optical fibres as sensing elements or transmission line have been developed around the world. The principle of fibre optic sensors are based on the conversion of input physical variables into modulated light signals. The advantages of optical fibres for sensing systems including good resistance to electromagnetic interference, safety from explosive environments, high information capacity, low signal attenuation, flexibility and lightness. Hence, optical fibres are well-suited to a sensing system such as SMI system.

The optical fibres vary in specifications, mainly depending on the applications that they are designed for. A typical optical fibre has five layers including core, cladding, coating, strength member, and outer jacket shown in Figure 3.14. The core is made of glass or plastic that provides the path for light propagation. The size of core is between 8 and 63 microns decides how much light can enter. The cladding prevents the light from exiting the core and being absorbed by the rest of the cable. The coating protects the core and cladding. The strength number is a layer that provides strength to the cable and helps prevent damage due to stress. The outer jacket is the last layer that provides protection and also adds strength to the fibre.
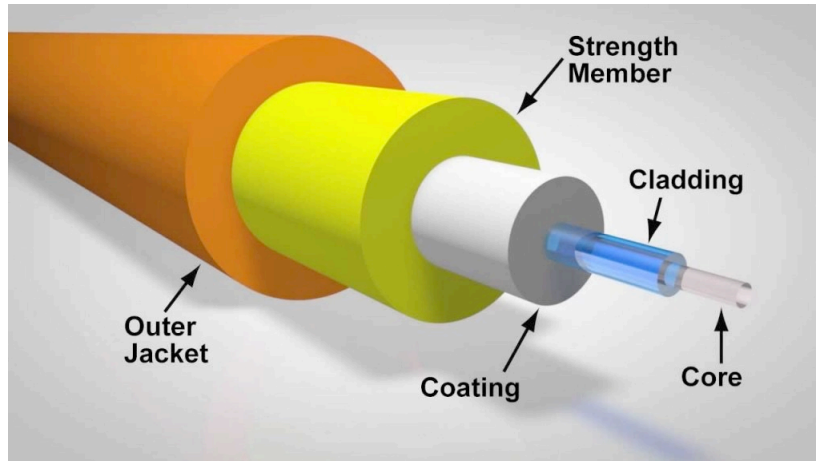
Figure 3.14. Structure of the optical fibre cable [120].

There are different types of optical fibre cables, mainly are single mode fibre and multimode fibre. The single mode fibre has a smaller core diameter of 8 microns and only allows a signal wavelength and pathway for light to travel, which greatly decreases light reflections and lowers attenuation. The multimode fibre has a larger core diameter, which allows multiple pathways and several wavelength of light to travel through. The two common sizes for multimode fibre are 50 microns and 62.5 microns. It is common for short distance transmission as the light attenuation is much larger than the single mode. Figure 3.15 shows the two types of fibres.
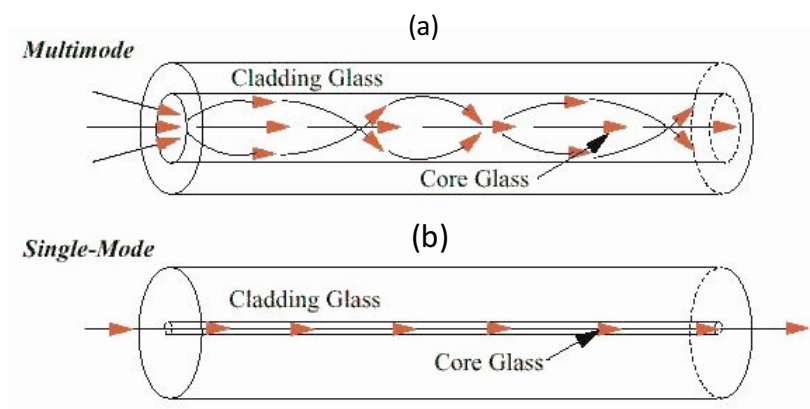


Figure 3.15. (a) single mode fibre and (b) multimode fibre

- Fibre optics coupling

As part of optical components, optical fibres use total internal reflection to confine and guide light within a solid or liquid structure. The situation of coupling light into an optical fibre is different for coupling into multimode fibres and single mode fibres. For coupling light into multimode fibres, it is about the angle of the incidence of light launched into the fibre. Optical fibres have an inner core made from a material with a certain refractive index that is higher than the surrounding cladding layer. There is a critical angle of incidence $\theta_{crit}$ such that light can reflect off the core and cladding interface rather than refract into the surrounding medium. The angle of incidence of the light launched into the fibre must be less than a certain acceptance angle $\theta_{acc}$ to fulfil the conditions for the total internal reflection in the fibre. By applying Snell's law,

$$\sin\theta_{crit} = \frac{n_{clad}}{n_{core}} = \cos\theta_t \tag{3.23}$$

$$n\sin\theta_{acc} = n_{core}\sqrt{1-\cos^2\theta_t} = \sqrt{n_{core}^2 - n_{clad}^2} \tag{3.24}$$

Where $n_{core}$ is the refractive index of the fibre core, $n_{clad}$ is the refractive index of the fibre cladding, $n$ is the refractive index of the outside medium. Figure 3.16 shows the total internal reflection in an optical fibre.
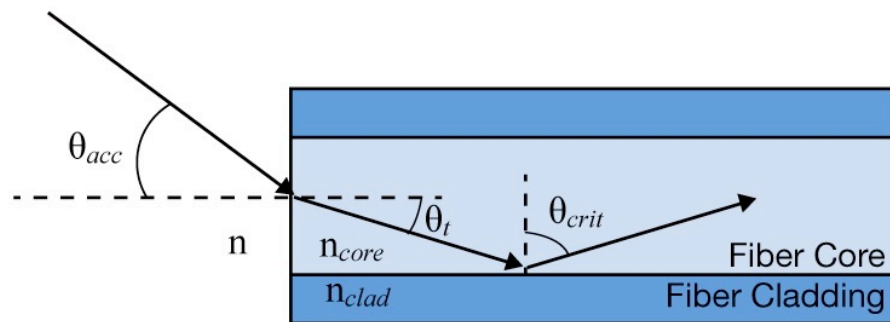


Figure 3.16. Total internal reflection in an optical fibre [120]

The numerical aperture ($NA$) is a dimensionless quantity to specify the acceptance angle of an optical fibre, defined as,

$$NA = n \sin \theta_{acc} = \sqrt{n_{core}^2 - n_{clad}^2}$$ (3.25)

For a multimode fibre, the $NA$ can be calculated by equation (3.25). Alternatively, it can be determined in experiment by tracing the far-field beam profile and measuring the angle between the centre of the beam and the point at which the beam intensity is 5% of the maximum.

The main difference between a multimode fibre and a single mode fibre is the number of the modes supported by the optical fibre. This number of modes depends on the physical dimension of the core and cladding, refractive index, and wavelength. The normalized optical frequency (denoted as $V$ numbers) is a dimensionless quantity, which is proportional to the free space optical frequency, defined as,

$$V = \frac{2\pi a}{\lambda} NA$$ (3.26)

Where $a$ is the radius of the fibre core and $\lambda$ is the free space wavelength. The number of modes supported by multimode fibre can be estimated with the following relationship,

$$M \approx \frac{V^2}{2}$$ (3.27)

- Fibre optics in the SMI system

The light source in the SMI system is the LD, which is installed inside the laser mount. For the measurement of the specimen vibration, the laser mount is fixed on top of the specimen with very limited adjustable movement. The optical fibre is introduced for the system, where the light source from LD is coupled into an optical fibre. The LD used in the system is THORLAB RLD65MZT2 with 655nm wavelength. First, a THORLAB M94L02 multimode fibre is chosen to extend the light source. It has a wavelength range between 400 to 2100nm, so the LD with 655nm wavelength can be coupled into it. The diameter of the core is $105\mu m$ and the $NA$ is 0.1. Based on equation (3.26), at a wavelength of 655nm, the fibre has a V number of 50.4. The number of modes supported by the fibre is approximately 1268 different modes from equation (3.27). A THORLAB PAF-X-11-PC-C

fibre port is utilized to couple the light into the fibre. Unfortunately, due to the high dispersion and attenuation rate, the quality of optical signal is greatly reduced. The feedback from the specimen is very weak result in difficult to obtain good SMI signal. It is better to use the single mode fibre, which has a low dispersion and attenuation rate compare to the multimode fibre. The commonly used single mode fibre wavelength is 1310nm and 1550nm. The LD used in the system is 655nm, which is hard to find a match single mode fibre. The THORLAB LP1550-SFD2 single mode fibre-pigtailed laser diode is installed in the system to replace the RLD65MZT2 laser diode. The electrical and optical characteristics of it is shown in Table 4.1

Table 3.2. Electrical and optical characteristics of LP1550-SFD2 [120]

| Parameter | Min | Typ | Max |
|---|---|---|---|
| Fibre output power ($P_{op}, mW$) | - | 2.0 | 2.5 |
| Operating current ($I_{op}, mA$) | - | 20.1 | 25 |
| Operating voltage ($V_{op}, V$) | - | 0.91 | 2.6 |
| Monitor current ($I_{mon}, mA$) | - | 0.324 | - |
| Threshold current ($I_{th}, mA$) | - | 6.2 | - |
| Peak emission wavelength ($\lambda, nm$) | - | 1550 | - |
| Storage temperature ($^{0}C$) | -10 | - | +65 |
| Case temperature ($^{0}C$) | 0 | - | +50 |

The PD is also packaged at the rear of the laser diode to convert the light to current under photodiode mode. The pin diagram for the equivalent circuit of signal converting is shown in Figure 3.17.

Figure 3.17. Structure of LP1550-SFD2 and its equivalent circuit pin diagram

A special laser mount LDM9LP is utilised to operate the LD. The laser installation is conducted by determining the laser pin configuration from the LP1550-SFD2 manufacturer's data sheets (shown in Figure 3.17) and set the LD and PD switches located on the inside of the laser mount according to the polarity switch settings from the user guide of laser mount LDM9LP. Figure 3.18 shows the laser mount after installing the fibre-pigtailed laser diode.



Figure 3.18. Laser mount with fibre-pigtailed laser diode

Ideally, the core of an optical fibre is perfectly circular. However, in reality, due to the mechanical stresses such as bending and twisting, the core is not perfectly circular. The birefringence is introduced in the fibre because of the external stress applied on the fibre. The phenomenon of birefringence often occurs in certain types of materials. The different materials have different indices of refraction leads to different polarization direction of light. The light travel in a single mode fibre consists of two orthogonal polarization modes. The effect of birefringence causes one of the orthogonal polarization modes travel faster than the other. In result, the light transmitted in the fibre experiences dispersion. This can also affect the SMI system, where the change of light polarization may result in no SMI effect. A fibre polarization controller can be utilised to control the polarization state in the optical fibre. The fibre polarization controller uses stress-induced birefringence to alter the polarization in a single mode fibre, which is looped around two or three independent spools. The birefringence in a fibre depends on the cladding diameter, the spool diameter, the number of fibre loops per spool, and the wavelength of the light. The transmitted polarization vector in the fibre looped around the spools can be adjust by rotating the paddles. A three paddles polarization controller consists of two quarter-wave plates on the side and one half-wave plate in the middle. The first quarter-wave plate transforms the input polarization state into a linear polarization state, the lf-wave plate rotates the linear polarization state, and the last quarter-wave plate transforms the linear state into an arbitrary polarization state. Figure 3.19 shows the schematic of fibre polarization controller.
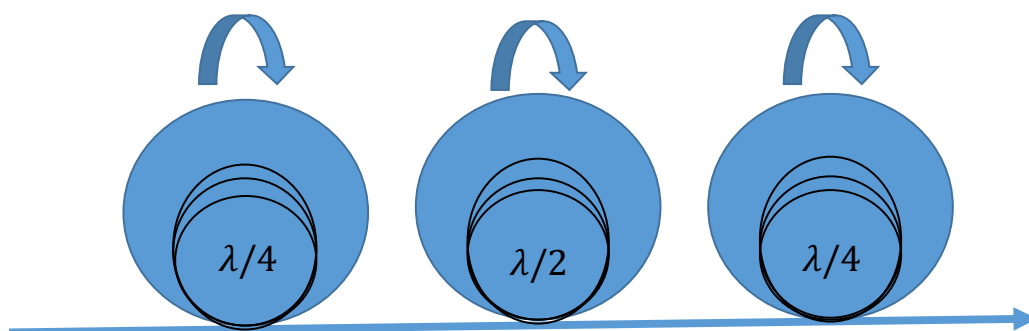


Figure 3.19. Schematic of fibre polarization controller, with two $\lambda/4$ plates on the side

and one $\lambda/2$ plate in the middle

The retardance of each paddle can be estimated by following equations,

$$\varphi(Radians) = \frac{2\pi^2 aNd^2}{\lambda D}$$ (3.28)

$$\varphi(Waves) = \frac{\pi aNd^2}{\lambda D}$$ (3.29)

Where $\varphi$ is the retardance, $a$ is constant as 0.133 for silica fibre, $N$ is the number of loops around the spool, $d$ is the fibre cladding diameter, $\lambda$ is the wavelength, and $D$ is the loop diameter. The THORLAB FPC561 fibre polarization controller is used in the system for the polarization of the light. The fibre used in the FPC561 is SMF-28-J9 and the core diameter is 8.2 $\mu m$. The wavelength of the light is 1550nm from the laser diode and the loop diameter is 56 $mm$. The retardance varies wavelength with different loops shows in Figure 3.20. The number of loops for each spool is 3, 6, and 3 respectively for the operation purpose.
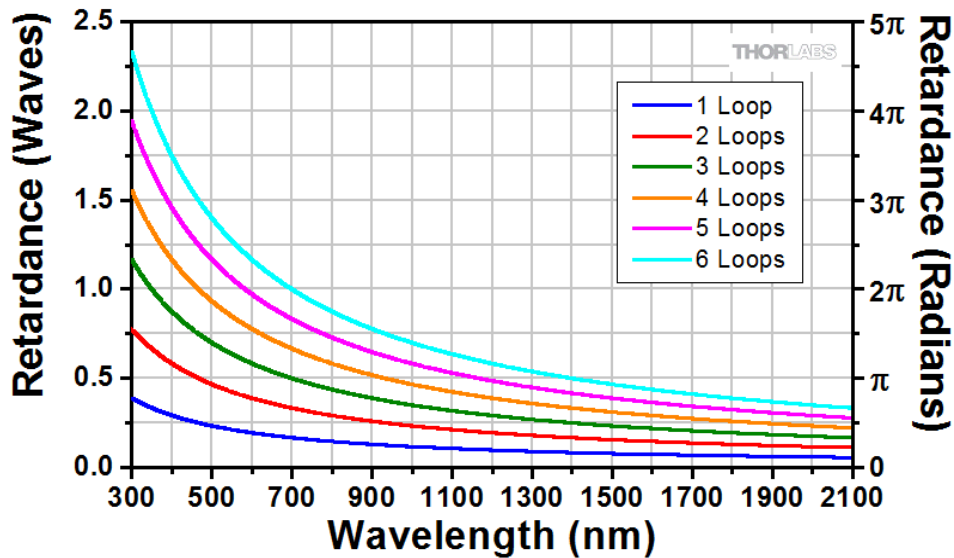


Figure 3.20. Retardance varies wavelength with different loops [120]

The SMI system with optical fibre is shown in Figure 3.21
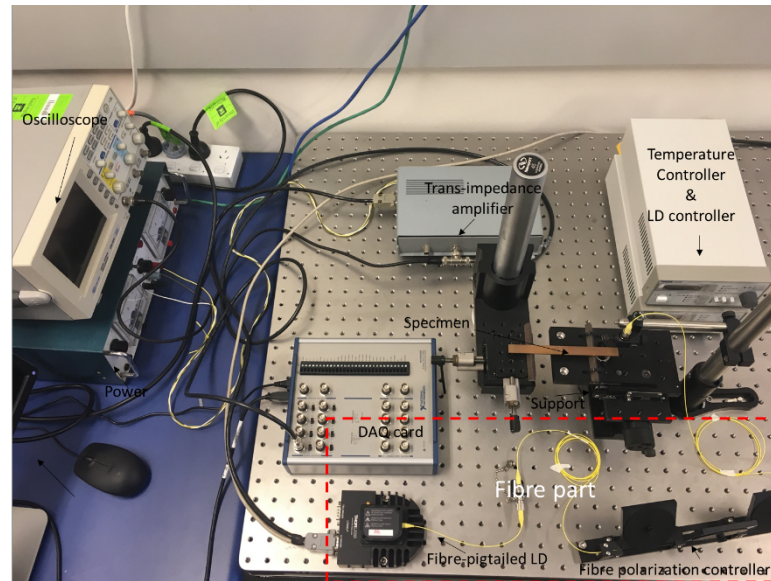


Figure 3.21. Overall system with optical fibre

## 3.3   Experimental results

The experiments are conducted separately for the system without and with fibre. The IET parts consist of a brass bar specimen with $l = 138.10\,\text{mm}$, $b = 12.01\,\text{mm}$, $h = 2.08\,\text{mm}$ and $m = 29.84\,\text{g}$, a Newport 426 series extended platform with two triangular prism fixed on top of it, and a polymer stick with a steel ball glued to the end. For the SMI system without fibre, it consists of a THORLABS RLD65MZT2 laser diode installed inside a THORLABS LDM21 Laser mount, an adjustable THORLABS C240TME-B aspheric lens. For the SMI system with fibre, it consists of a THORLAB LP1550-SFD2 single mode fibre-pigtailed laser diode, installed in a LDM9LP laser mount, a THORLAB FPC561 fibre polarization controller. Both systems are connected to a THORLABS LDC205C laser controller, a THORLABS TED200C temperature controller, the trans-impedance circuits, an NI USB-6361 DAQ card, an oscilloscope, and a private computer The procedure of the experiment is shown as below

- IET part
  - ➤ Install the support platform on the pneumatized vibration isolation table and fix the two triangular prism on the top of the platform.
  - ➤ Carefully place the brass bar specimen on the two triangular prism, and then adjust the lateral bearings on the platform to make the two supporting points at $0.224l$ on each side.
- SMI part without fibre
  - ➤ Follow the pin diagram to install the THORLABS RLD65MZT2 laser diode into the LDM9LP laser mount and install the aspheric lens from the outside of the laser mount.
  - ➤ Turn on the laser controller and temperature controller to stabilize the laser, set the current as 29mA and the temperature as $25^0$C.
  - ➤ Adjust the aspheric lens to focus the beam on the reference point at the end of the specimen, or adjust the vertical lateral bearings on the platform to form an external cavity with the length about 0.5m.
- SMI part with fibre
  - ➤ Follow the pin diagram to install the THORLAB LP1550-SFD2 single mode fibre-pigtailed laser diode into the LDM9LP laser mount and connect the THORLAB FPC561 fibre polarization controller with the laser diode.
  - ➤ Turn on the laser controller and temperature controller to stabilize the laser, set the current as 14mA and the temperature as $25^0$C.
  - ➤ Installed the collimator on the other side of the extended fibre to collimate the light onto the specimen. Rotate the plates on the fibre polarization controller to control the polarization state in the fibre.

With a light strike on the specimen, the specimen is stimulated into damping vibration. This damping vibration signal is captured by the SMI system and a corresponding SMI signal is generated. The SMI signal is sampled by the DAQ card and a MATLAB program script is ready to process the signal and export the measurement results. A graphical user interface (GUI) is designed to display the measurement results. The detail

description of the GUI is in the Appendix A.

- Result without fibre

Figure 3.22 shows the experimental SMI signal from the system without fibre. The sampling rates are 200kHz and the data length for each signal is 1s.



Figure 3.22. Experimental SMI signal of brass specimen. (a),(b) zoomed in parts of (c) SMI signal.

In Figure 3.22, the top two figures (a) and (b) are the zoomed in parts of the SMI signal. It is clear to see that the fringe numbers decrease with the time, from which we can retrieve the damping factor and we can retrieve the resonant frequency from the SMI signal as well. Figure 3.23 shows the scalogram of the wavelet transform result of the SMI signal.
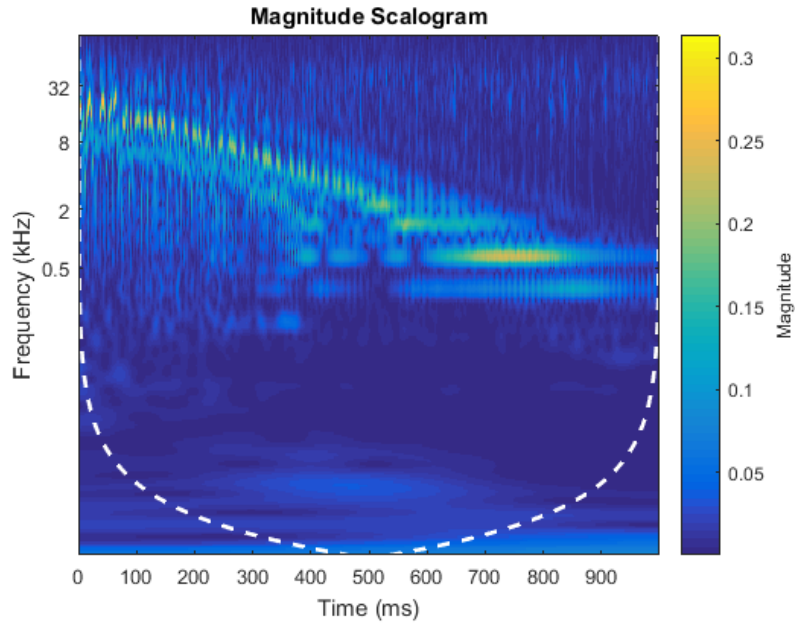
Figure 3.23. Scalogram of the CWT of the experimental SMI signal.

Follow the steps in section 2.4.2 of retrieving the resonant frequency and damping factor of the target vibration, we can first get the real part of the wavelet coefficient plotted against the frequency shown in Figure 3.24. The dominating frequency in the SMI signal is 424.8Hz, which means the resonant frequency of the specimen is 424.8Hz. The damping factor can be retrieved by extracting the frequencies with maximum amplitude along the time. Figure 3.25 shows the extraction and curve-fitting results. The descent slope of the curve in Figure 3.25 (b) is $-2.26 \times 10^{-5}$. The sampling frequency is 200kHz so the real value of the descent slope is -4.52, which is the measured damping factor of the specimen.

Figure 3.24. Real part of wavelet coefficient plotted against frequency



Figure 3.25. (a) Frequency with maximum amplitude against time. (b) curve-fitting result after excluding other points.

Based on equation (2.28) $E = 0.9465 \cdot \dfrac{mf_{RO}^2 L^3}{bh^3} \cdot T$, where $T = 1 + 6.585\left(\dfrac{h}{L}\right)^2$, the

92

measured Young's modulus is 120.88GPa. Based on equation (2.30) $Q^{-1} = \dfrac{k}{\pi f_{RO}}$, the

measured internal friction is $3.45 \times 10^{-3}$.

- Result with fibre

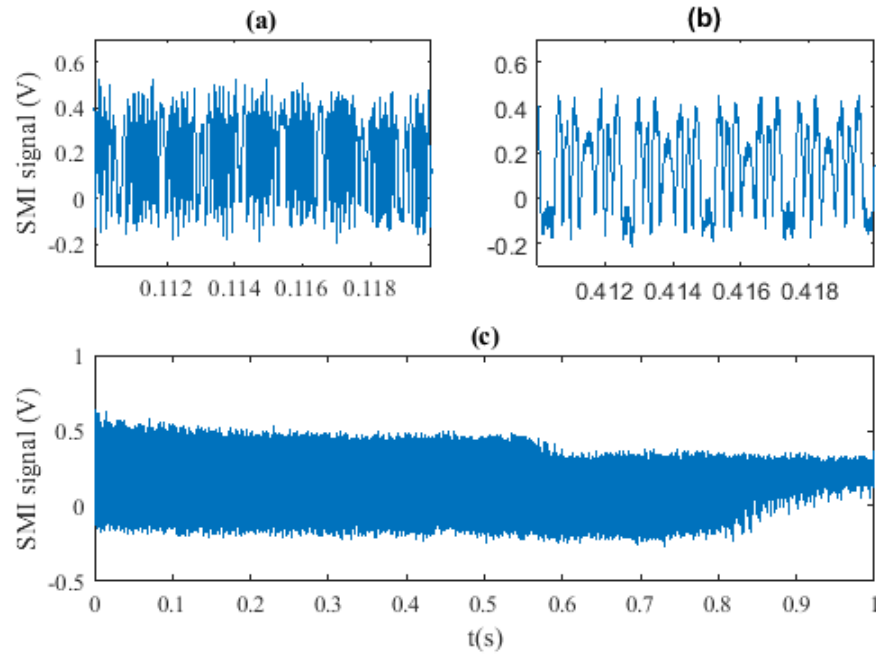Figure 3.26 shows the experimental SMI signal from the system with fibre. The sampling rates are 200kHz and the data length for each signal is 1s. Figure 3.27 shows the scalogram of the wavelet transform result of the experimental SMI signal.
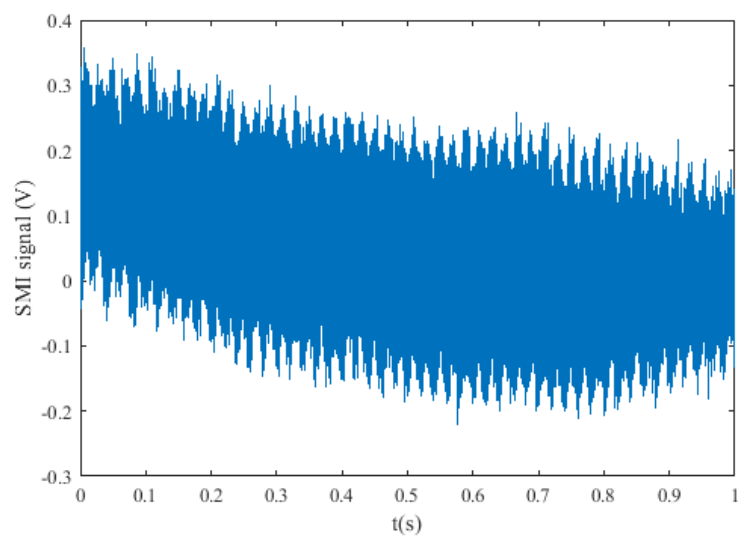


Figure 3.26. Experimental SMI signal from the system with optical fibre
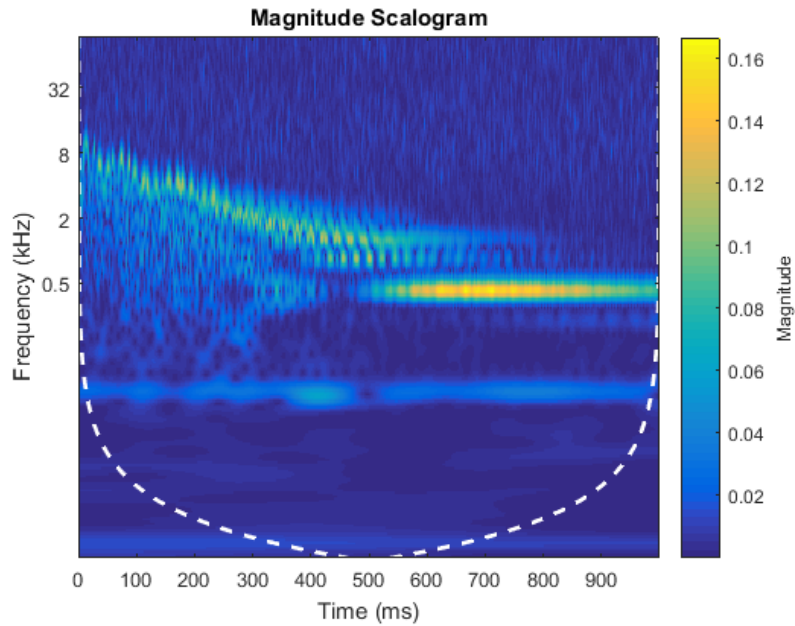
Figure 3.27. Scalogram of the CWT of the experimental SMI signal

The real part of wavelet coefficient plotted against frequency is shown in Figure 3.28. The dominating frequency is 424.8Hz. The measured Young's modulus is 120.88GPa. Figure 3.29 shows the extraction of the frequencies with maximum amplitude along the time and the curve-fitting results. The descent slope of the curve is $-2.30 \times 10^{-5}$. The sampling rates are 200kHz so the measured damping factor is -4.60. The measured internal friction is $3.45 \times 10^{-3}$.
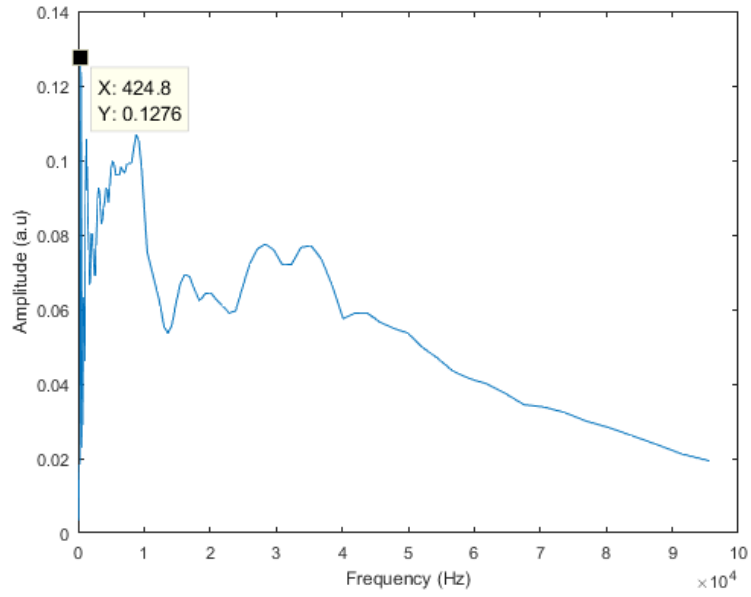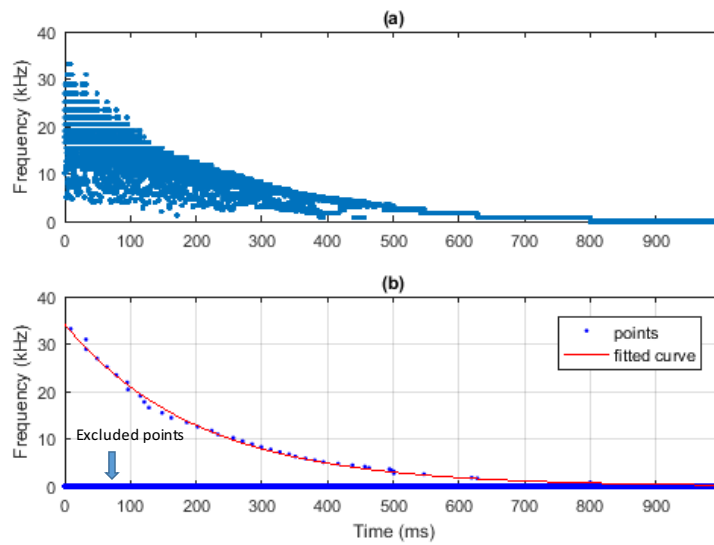
Figure 3.28. Real part of wavelet coefficient plotted against frequency



Figure 3.29. (a) Frequency with maximum amplitude against time. (b) curve-fitting result after excluding other points

The experiments are repeated 10 times for each SMI system without and with fibre. The measurement results of resonant frequency, Young's modulus, damping factor and

internal friction are presented in Table 3.3.

Table 3.3. Measurement results of two brass specimens

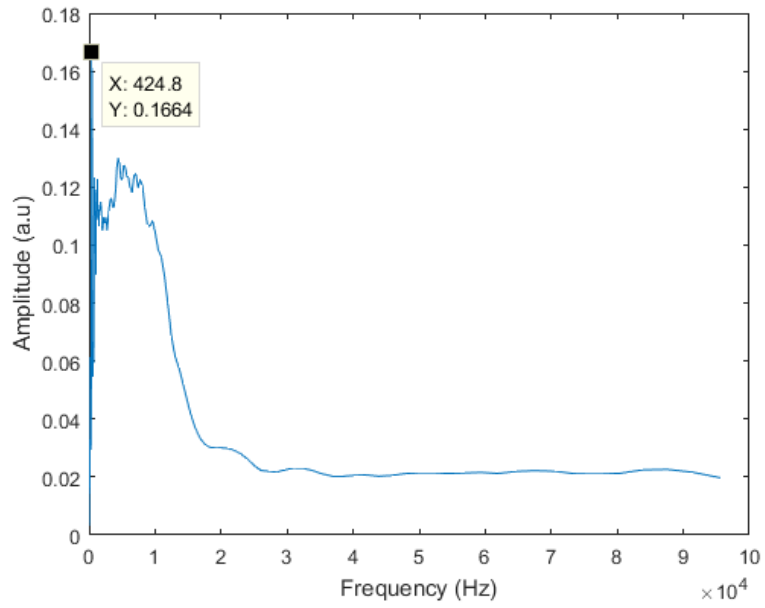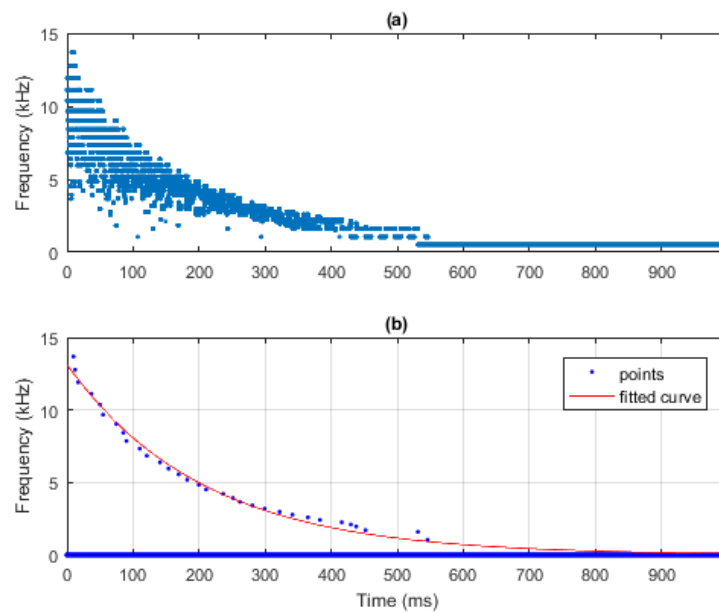| System type / Times | SMI system without fibre | | | | SMI system with fibre | | | |
|---|---|---|---|---|---|---|---|---|
| | $f_{RO}$ (Hz) | $E$ (GPa) | $k$ | $Q^{-1}$ | $f_{RO}$ (Hz) | $E$ (GPa) | $k$ | $Q^{-1}$ |
| 1 | 424.79 | 120.88 | 4.52 | $3.39 \times 10^{-3}$ | 424.79 | 120.88 | 4.61 | $3.45 \times 10^{-3}$ |
| 2 | 424.79 | 120.88 | 4.47 | $3.35 \times 10^{-3}$ | 424.79 | 120.88 | 4.53 | $3.39 \times 10^{-3}$ |
| 3 | 424.79 | 120.88 | 4.50 | $3.37 \times 10^{-3}$ | 424.79 | 120.88 | 4.56 | $3.42 \times 10^{-3}$ |
| 4 | 424.79 | 120.88 | 4.49 | $3.36 \times 10^{-3}$ | 424.79 | 120.88 | 4.50 | $3.37 \times 10^{-3}$ |
| 5 | 424.79 | 120.88 | 4.53 | $3.39 \times 10^{-3}$ | 424.79 | 120.88 | 4.61 | $3.45 \times 10^{-3}$ |
| 6 | 424.79 | 120.88 | 4.63 | $3.47 \times 10^{-3}$ | 424.79 | 120.88 | 4.58 | $3.43 \times 10^{-3}$ |
| 7 | 424.79 | 120.88 | 4.59 | $3.43 \times 10^{-3}$ | 424.79 | 120.88 | 4.52 | $3.39 \times 10^{-3}$ |
| 8 | 424.79 | 120.88 | 4.50 | $3.37 \times 10^{-3}$ | 424.79 | 120.88 | 4.53 | $3.39 \times 10^{-3}$ |
| 9 | 424.79 | 120.88 | 4.48 | $3.36 \times 10^{-3}$ | 424.79 | 120.88 | 4.48 | $3.36 \times 10^{-3}$ |
| 10 | 424.79 | 120.88 | 4.52 | $3.39 \times 10^{-3}$ | 424.79 | 120.88 | 4.54 | $3.40 \times 10^{-3}$ |

The average measured value of Young's modulus and internal friction for specimen are 120.88GPa and $3.39 \times 10^{-3}$ with a small standard derivation of $\sigma = 0.03$. The equation of standard derivation is shown as below, $N = 20$, $x_i$ refers to each measured value of $Q^{-1}$, and $\mu$ is the mean value over the measured 20 values.

$$\sigma = \sqrt{\frac{1}{N} \sum_{i=1}^{N} (x_i - \mu)^2} \qquad (3.30)$$

It can be seen that the Young's modulus and internal friction measured by our system shows high repeatability with very low standard derivation for both SMI system without and with fibre. The measured value of Young's modulus for brass specimen are also very close to the value between 102 and 125GPa reported in the literature [108]. There are several advantages of the proposed measurement system compare to the traditional

method.

> ➤ By the using the proposed system, both Young's modulus and internal friction can be measured at the same time.
> ➤ The measured values for Young's modulus fall in the ranges reported in other method while in the proposed system the measurement results have low standard derivation
> ➤ The measurement in the proposed system has no damage to the specimen, which shows high repeatability of the measurement.

## 3.4   Summary

This chapter presents the implementation for the measurements of material related parameters including the overall system structure, system design, and experimental results.

Firstly, the overall system structure is presented in section 3.1

In section 3.2, it separates the whole system into two parts, IET part, SMI part. IET part contains specimen, support device and stimulation tool. SMI part contains laser diode and laser controllers, trans-impedance circuits, DAQ card, oscilloscope and a private computer. The selection of the components in each part is specified in detail. Then the optical fibre is introduced to the SMI part. The fibre extends the external cavity length so that the stability of the SMI system is improved. It also makes it easier to adjust the angle of the laser beam on the specimen.

Lastly, in section 3.3, the procedure of the experiment is presented and the experimental results from both SMI system without and with fibre are compared with the results in the literature. The results measured from the proposed system shows high accuracy and repeatability for both Young's modulus and internal friction measurement. The proposed method of simultaneously measuring material related parameters using self-mixing system based on wavelet transform is feasible.

# Chapter 4　　Conclusion

As a promising sensing technique, SMI has been extensively studies during the recent decades. The non-contact and non-destructive advantage of this technique makes it popular for the high accuracy and sensitivity measurement. By combining SMI technique with impulse excitation technique, a new method for simultaneous measurement of material related parameters is proposed. The material related parameters such as Young's modulus and internal friction can be retrieved from the SMI signal by applying wavelet transform onto it.

In this chapter, the research contributions are summarised in section 5.1, the suggested future work based on the study in this thesis is proposed in section 5.2

## 4.1　　Suggested future work

In future work on using SMI system for the material related parameters measurement, the following topics will be useful:

- Simultaneous measurements for more material related parameters such as shear modulus and poisson's ratio. The support device for the specimen needs to be modified to meet the measurement requirement for other material related parameters. Ideally, more parameters can be measured because of the high sensitivity and accuracy of SMI technique.

- Wavelet design for SMI signal. The wavelet used in the analysis of SMI signal is Morlet wavelet, which was developed many years ago. It is not specially designed for SMI signal analysis. A better suited wavelet can be designed based on the features of SMI signal, which will be useful not only for external target related parameters measurement but also for laser related parameters such as

linewidth enhancement factor $\alpha$ and feedback level $C$.

- Measurement with different materials. The specimen used in this thesis is brass bar, which is the metal type. Other materials such as rubber, glass, or polyester, that have different features of properties are also very interesting research targets.

# Appendix A: GUI manual

The GUI consists of four parts, the initial interface, the introduction interface, the main interface and the close interface. Figure 1 shows the initial interface. It shows the title of the GUI and gives a system picture of the whole system.
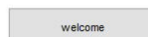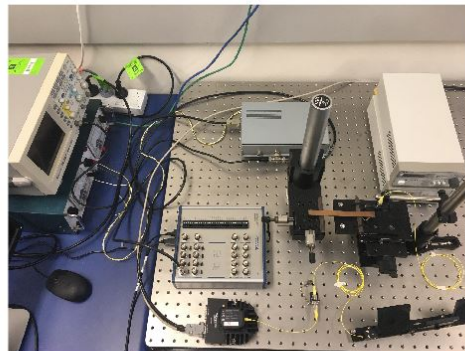


Figure.1    The initial interface.

Click the 'welcome' button on the initial interface, shown in Figure 2. The introduction interface will show up, shown in Figure 3.
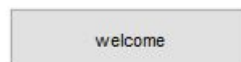


Figure.2    'Welcome' button.

**_Introduction_**

This measurement interface measures the material related parameters:

Resonant frequency $f$

Young's modulus $E$

damping factor $k$

internal friction $Q^{-1}$

$$E = 0.9465 \cdot \frac{m f^2 L^3}{b h^3} \cdot T \qquad Q^{-1} = \frac{k}{\pi f}$$

Where $T = 1 + 6.585(h/L)^2$ is the correction factor, $m$ is the mass, $L$ is the length, $b$ is the width and $h$ is the height.
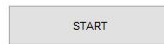
START

Figure.3    The introduction interface.

The introduction interface introduces the material related parameters that can be measured by the GUI and the fundamental measurement principle. Click the 'START' button on the introduction interface, shown in Figure 4. The main interface will show up, shown in Figure 5.

START

Figure.4    'START' button.

101
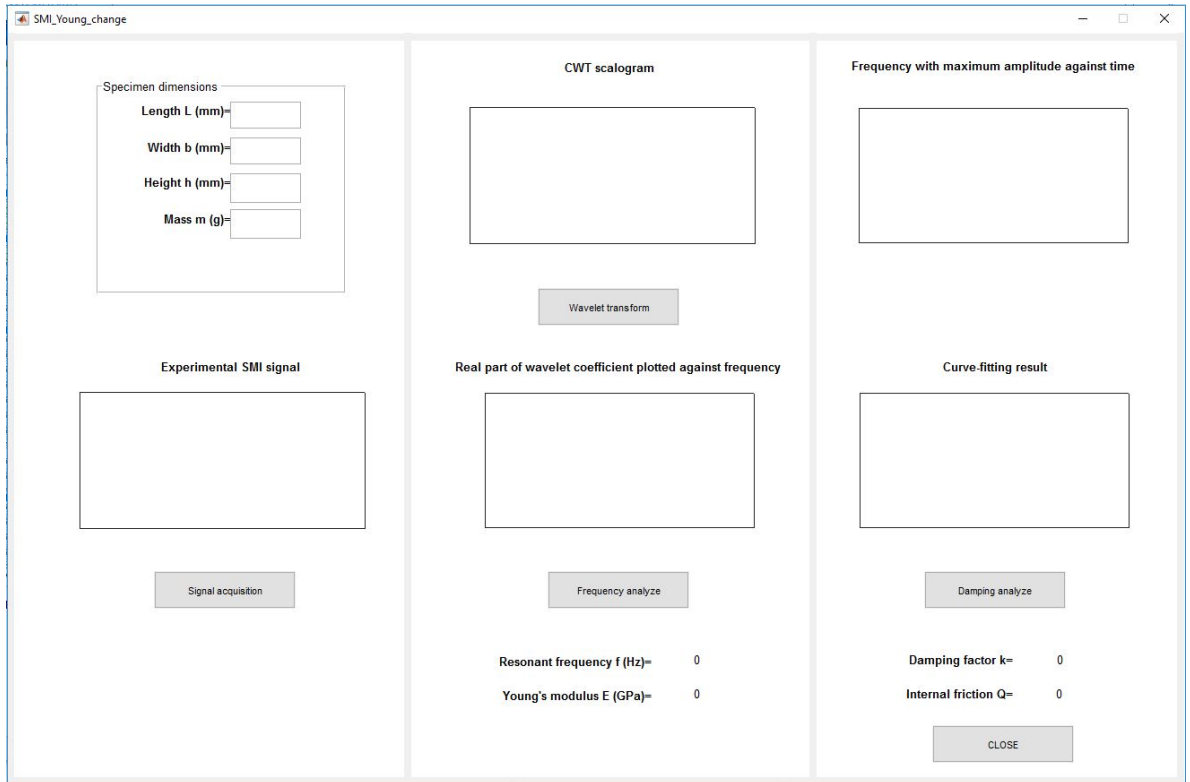
Figure.5    The Main interface.


The operation procedure of the main interface is shown as below

1.  Enter the specimen dimensions in the panel, shown in Figure 6.



Figure.6    Specimen dimensions panel

2.  Click the 'signal acquisition' button, the experimental SMI signal will show in the Figure 7 as below.

**Experimental SMI signal**



Signal acquisition
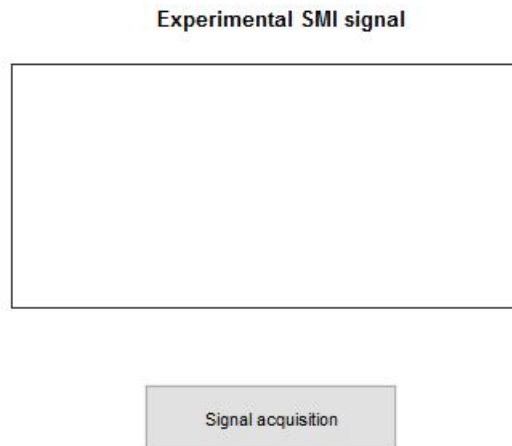
Figure.7    Signal acquisition.

3.  Click the 'wavelet transform' button, the CWT results of the experimental SMI signal will show in the Figure 8 as below.

**CWT scalogram**
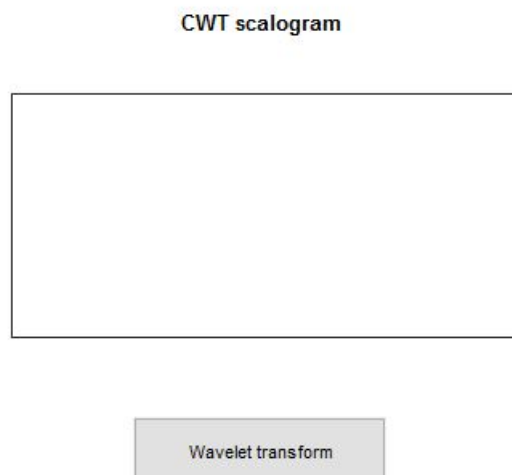


Wavelet transform

Figure.8    Wavelet transform.

4. Click the 'Frequency analyze' button, the frequency components in the SMI signal will show in the Figure 9 as below. The resonant frequency of the specimen will show in the output next to 'Resonant frequency f (Hz)' and the calculated Young's modulus will show in the output next to 'Young's modulus E (GPa)'.

**Real part of wavelet coefficient plotted against frequency**

Frequency analyze

Resonant frequency f (Hz)=          0

Young's modulus E (GPa)=          0

Figure.9      Frequency analyze.

5. Click the 'Damping analyze' button, the frequency with maximum amplitude against time and the curve-fitting result will show in the Figure 10 as below. The damping factor will show in the output next to 'Damping factor k' and the calculated internal friction will show in the output next to 'Internal friction Q'.

**Frequency with maximum amplitude against time**
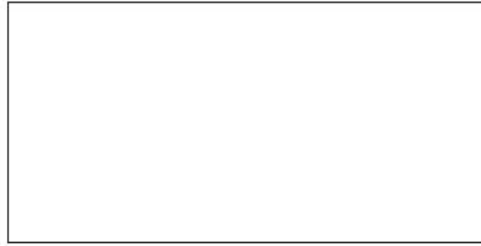
**Curve-fitting result**

Damping analyze

**Damping factor k=**      0

**Internal friction Q=**      0

Figure.10      Damping analyze

6.  Close the main interface by clicking the 'CLOSE' button, shown in Figure 11.

CLOSE

Figure.11      'CLOSE' button.

Figure 12 shows the example of the main interface.
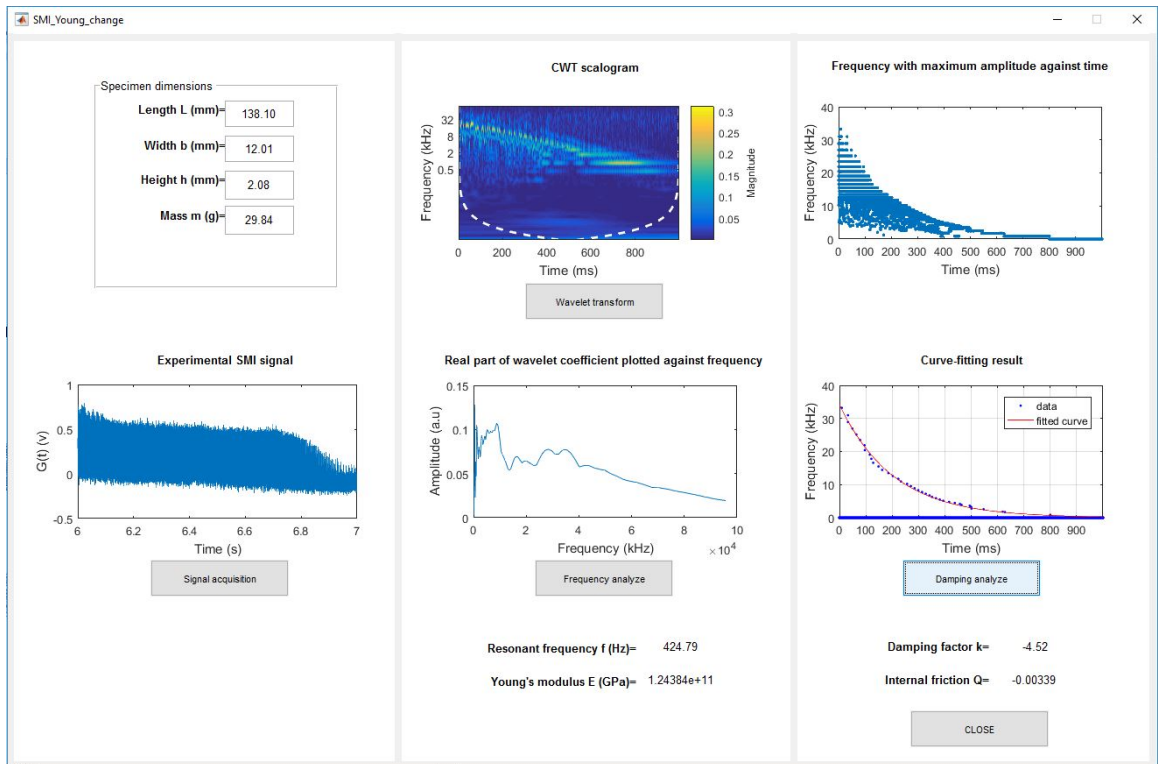
Figure.12    Example of the main interface.

The close interface will show up after clicking the 'CLOSE' button, shown in Figure 13.



Figure.13    The close interface.

# Appendix B: References

[1]     B. J. Lazan, Damping of materials and members in structural mechanics. Pergamon press Oxford, 1968.

[2]     L. Zhang, D. Uttamchandani, B. Culshaw, and P. Dobson, "Measurement of Young's modulus and internal stress in silicon microresonators using a resonant frequency technique," Measurement science and technology, vol. 1, no. 12, p. 1343, 1990.

[3]     T. E. o. E. Britannica, "Young's modulus," in Young's modulus, ed: Encyclopædia Britannica, inc., 2017.

[4]     M. S. Blanter, I. Golovin, H. Neuhauser, and H. Sinning, "Internal friction in metallic materials," A Handbook. Springer Verlag, p. 540, 2007.

[5]     N. Suansuwan, "Determination of elastic properties of metal alloys and dental porcelains," Journal of Oral Rehabilitation, vol. 28, no. 2, pp. 133-139, 2001.

[6]     A. K. Swarnakar, O. van der Biest, and B. Baufeld, "Young's modulus and damping in dependence on temperature of Ti–6Al–4V components fabricated by shaped metal deposition," Journal of Materials Science, journal article vol. 46, no. 11, pp. 3802-3811, June 01 2011.

[7]     W. T. Chu, "A comparison of two test methods for measuring Young's modulus of building materials," Canadian Acoustics, vol. 24, no. 3, pp. 11-11, 1996.

[8]     G. Li, Y. Zhao, S.-S. Pang, and Y. Li, "Effective Young's modulus estimation of concrete," Cement and Concrete Research, vol. 29, no. 9, pp. 1455-1462, 1999.

[9]     M. Asmani, C. Kermel, A. Leriche, and M. Ourak, "Influence of porosity on Young's modulus and Poisson's ratio in alumina ceramics," Journal of the European ceramic society, vol. 21, no. 8, pp. 1081-1086, 2001.

[10]    J. Wachtman and D. Lam, "Young's modulus of various refractory materials as a function of temperature," Journal of the American Ceramic Society, vol. 42, no. 5, pp. 254-260, 1959.

[11]    C. W. De Silva, Vibration damping, control, and design. CRC Press, 2007.

[12]    T. L. Gilbert, "A phenomenological theory of damping in ferromagnetic materials," IEEE Transactions on Magnetics, vol. 40, no. 6, pp. 3443-3449, 2004.

[13]    A. Luz, T. Santos Jr, J. Medeiros, and V. Pandolfelli, "Thermal shock damage evaluation of refractory castables via hot elastic modulus measurements," Ceramics International, vol. 39, no. 6, pp. 6189-6197, 2013.

[14]    F. J. Weber and E. R. Burke, "Cushion for absorbing shock, damping vibration and distributing pressure," ed: Google Patents, 1994.

[15]    D. Sinclair, "A bending method for measurement of the tensile strength and

Young's modulus of glass fibers," Journal of Applied Physics, vol. 21, no. 5, pp. 380-386, 1950.

[16]    B. Demczyk et al., "Direct mechanical measurement of the tensile strength and elastic modulus of multiwalled carbon nanotubes," Materials Science and Engineering: A, vol. 334, no. 1-2, pp. 173-178, 2002.

[17]    E. ARCHIVES. (8 May). Tensile Test. Available: http://www.engineeringarchives.com/les_mom_tensiletest.html

[18]    B. Liu, R. Villavicencio, and C. G. Soares, "Failure characteristics of strength-equivalent aluminium and steel plates in impact conditions," Analysis and Design of Marine Structures, p. 167, 2013.

[19]    C. S. Lynch, "The effect of uniaxial stress on the electro-mechanical response of 8/65/35 PLZT," Acta materialia, vol. 44, no. 10, pp. 4137-4148, 1996.

[20]    D. K. Shetty, A. R. Rosenfield, P. McGuire, G. K. Bansal, and W. H. Duckworth, "Biaxial flexure tests for ceramics," American Ceramic Society Bulletin, vol. 59, no. 12, pp. 1193-1197, 1980.

[21]    F. Mujika, N. Carbajal, A. Arrese, and I. Mondragon, "Determination of tensile and compressive moduli by flexural tests," Polymer testing, vol. 25, no. 6, pp. 766-771, 2006.

[22]    P. DeHoff, K. Anusavice, and P. Hathcock, "Materials Science: An Evaluation of the Four-point Flexural Test for Metal-Ceramic Bond Strength," Journal of dental research, vol. 61, no. 9, pp. 1066-1069, 1982.

[23]    L. Ćurković, A. Bakić, J. Kodvanj, and T. Haramina, "Flexural strength of alumina ceramics: Weibull analysis," Transactions of FAMENA, vol. 34, no. 1, pp. 13-18, 2010.

[24]    A. Bhattacharya and W. Nix, "Analysis of elastic and plastic deformation associated with indentation testing of thin films on substrates," International Journal of Solids and Structures, vol. 24, no. 12, pp. 1287-1298, 1988.

[25]    G. Pharr and W. Oliver, "Measurement of thin film mechanical properties using nanoindentation," Mrs Bulletin, vol. 17, no. 7, pp. 28-33, 1992.

[26]    A. Ivankovic et al., "Development of fast and easy methods for measuring the Young's modulus of molding compounds for IC packages," in Thermal, Mechanical & Multi-Physics Simulation, and Experiments in Microelectronics and Microsystems (EuroSimE), 2010 11th International Conference on, 2010, pp. 1-7: IEEE.

[27]    J. Lord and R. Morrell, "Comparison of static and dynamic methods for measuring stiffness of high modulus steels and metal composites," Canadian Metallurgical Quarterly, vol. 53, no. 3, pp. 292-299, 2014.

[28]    E. ASTM, "Standard test method for dynamic young's modulus, shear modulus, and poisson's ratio by impulse excitation of vibration," Annual Book of ASTM Standards, vol. 3, 1876.

[29]    R. Colwell and H. Hardy, "LXXXIX. The frequencies and nodal systems of circular plates," The London, Edinburgh, and Dublin Philosophical Magazine and Journal of Science, vol. 24, no. 165, pp. 1041-1055, 1937.

[30]    L. Kiesewetter, J.-M. Zhang, D. Houdeau, and A. Steckenborn, "Determination of

Young's moduli of micromechanical thin films using the resonance method," Sensors and Actuators A: Physical, vol. 35, no. 2, pp. 153-159, 1992.

[31]  D. Ramos, J. Tamayo, J. Mertens, and M. Calleja, "Photothermal excitation of microcantilevers in liquids," Journal of Applied Physics, vol. 99, no. 12, p. 124904, 2006.

[32]  V. Pini, B. Tiribilli, C. M. C. Gambi, and M. Vassalli, "Dynamical characterization of vibrating AFM cantilevers forced by photothermal excitation," Physical Review B, vol. 81, no. 5, p. 054302, 2010.

[33]  S. Nishida, D. Kobayashi, T. Sakurada, T. Nakazawa, Y. Hoshi, and H. Kawakatsu, "Photothermal excitation and laser Doppler velocimetry of higher cantilever vibration modes for dynamic atomic force microscopy in liquid," Review of scientific instruments, vol. 79, no. 12, p. 123703, 2008.

[34]  A. Yoshinaka, Y. Yuasa, S. Hiroshima, T. Arie, and S. Akita, "Photothermal excitation of cantilevered carbon nanotube resonators," Applied Physics Express, vol. 5, no. 7, p. 075101, 2012.

[35]  Y. Song, B. Cretin, D. M. Todorovic, and P. Vairac, "Study of photothermal vibrations of semiconductor cantilevers near the resonant frequency," Journal of Physics D: Applied Physics, vol. 41, no. 15, p. 155106, 2008.

[36]  B. A. Bircher, L. Duempelmann, H. P. Lang, C. Gerber, and T. Braun, "Photothermal excitation of microcantilevers in liquid: effect of the excitation laser position on temperature and vibrational amplitude," IET Micro & Nano Letters, vol. 8, no. 11, pp. 770-774, 2013.

[37]  J. Bass, "A review of electro-optic beam deflection techniques," Radio and Electronic Engineer, vol. 34, no. 6, pp. 345-352, 1967.

[38]  C. A. Putman, B. G. De Grooth, N. F. Van Hulst, and J. Greve, "A detailed analysis of the optical beam deflection technique for use in atomic force microscopy," Journal of Applied Physics, vol. 72, no. 1, pp. 6-12, 1992.

[39]  C. V. Ramachandra Reddy, N. Ganesan, B. V. A. Rao, and S. Narayanan, "Response of plates with unconstrained layer damping treatment to random acoustic excitation, part II: Response evaluation," Journal of Sound and Vibration, vol. 69, no. 1, pp. 45-57, 1980/03/08 1980.

[40]  B. Kemps et al., "Development of a Methodology for the Calculation of Young's Modulus of Eggshell using Vibration Measurements," Biosystems engineering, vol. 89, no. 2, pp. 215-221, 2004.

[41]  J. Ricci and C. Cetinkaya, "Air-coupled acoustic method for testing and evaluation of microscale structures," Review of scientific instruments, vol. 78, no. 5, p. 055105, 2007.

[42]  M. Bamber, K. Cooke, A. Mann, and B. Derby, "Accurate determination of Young's modulus and Poisson's ratio of thin films by a combination of acoustic microscopy and nanoindentation," Thin Solid Films, vol. 398, pp. 299-305, 2001.

[43]  M. Fatemi and J. F. Greenleaf, "Application of radiation force in noncontact measurement of the elastic parameters," Ultrasonic Imaging, vol. 21, no. 2, pp. 147-154, 1999.

[44]  I. Akseli, D. C. Becker, and C. Cetinkaya, "Ultrasonic determination of Young's

moduli of the coat and core materials of a drug tablet," International journal of pharmaceutics, vol. 370, no. 1, pp. 17-25, 2009.

[45]    X. Ma et al., "Determination of elastic modulus for hollow spherical shells via resonant ultrasound spectroscopy," Fusion Engineering and Design, vol. 117, pp. 74-78, 2017.

[46]    X. Ye, Z. Zhou, Y. Yang, J. Zhang, and J. Yao, "Determination of the mechanical properties of microstructures," Sensors and Actuators A: Physical, vol. 54, no. 1-3, pp. 750-754, 1996.

[47]    R. Caracciolo, A. Gasparetto, and M. Giovagnoni, "MEASUREMENT OF THE ISOTROPIC DYNAMIC YOUNG'S MODULUS IN A SEISMICALLY EXCITED CANTILEVER BEAM USING A LASER SENSOR," Journal of Sound and Vibration, vol. 231, no. 5, pp. 1339-1353, 2000/04/13 2000.

[48]    F. M. Guillot and D. Trivett, "A dynamic Young's modulus measurement system for highly compliant polymers," The Journal of the Acoustical Society of America, vol. 114, no. 3, pp. 1334-1345, 2003.

[49]    R. Atri, K. Ravichandran, and S. Jha, "Elastic properties of in-situ processed Ti–TiB composites measured by impulse excitation of vibration," Materials Science and Engineering: A, vol. 271, no. 1, pp. 150-159, 1999.

[50]    S. Tognana, W. Salgueiro, A. Somoza, and A. Marzocca, "Measurement of the Young's modulus in particulate epoxy composites using the impulse excitation technique," Materials Science and Engineering: A, vol. 527, no. 18, pp. 4619-4623, 2010.

[51]    "Standard Test Method for Dynamic Young's Modulus, Shear Modulus, and Poisson's Ratio for Advanced Ceramics by Sonic Resonance," ed, 2009.

[52]    O. Bahr, P. Schaumann, B. Bollen, and J. Bracke, "Young's modulus and Poisson's ratio of concrete at high temperatures: Experimental investigations," Materials & Design, vol. 45, pp. 421-429, 2013.

[53]    S. Montecinos, S. Tognana, and W. Salgueiro, "Determination of the Young's modulus in CuAlBe shape memory alloys with different microstructures by impulse excitation technique," Materials Science and Engineering: A, vol. 676, pp. 121-127, 2016.

[54]    M. Slim, A. Alhussein, F. Sanchette, B. Guelorget, and M. François, "An enhanced formulation to determine Young's and shear moduli of thin films by means of Impulse Excitation Technique," Thin Solid Films, 2017.

[55]    Y.-l. Liu, X. Xiao, X.-m. Shan, and S.-c. Fu, "Young's Modulus Detection for the Low-k Film by Laser-Generated SAWs," in Photonics and Optoelectronics, 2009. SOPO 2009. Symposium on, 2009, pp. 1-4: IEEE.

[56]    C. Jin, J. Luttmer, D. M. Smith, and T. A. Ramos, "Nanoporous silica as an ultralow-k dielectric," MRS Bulletin, vol. 22, no. 10, pp. 39-42, 1997.

[57]    L. Zhiguo, X. Xia, Z. Xinhui, and Y. Suying, "Dispersive Characteristics of Surface Acoustic Waves for Measuring Mechanical Properties of Low-k Dielectrics Used in ULSI," CHINESE JOURNAL OF SEMICONDUCTORS-CHINESE EDITION-, vol. 26, no. 10, p. 2032, 2005.

[58]    F. Orban, "Damping of materials and members in structures," in Journal of Physics:

Conference Series, 2011, vol. 268, no. 1, p. 012022: IOP Publishing.

[59]    A. Puškár, Internal friction of materials. Cambridge Int Science Publishing, 2001.

[60]    T. i.-S. Kê, "Experimental evidence of the viscous behavior of grain boundaries in metals," Phys. Rev., vol. 71, pp. 533-546, 1947.

[61]    R. S. Lakes, "Viscoelastic measurement techniques," Review of scientific instruments, vol. 75, no. 4, pp. 797-810, 2004.

[62]    L. Stavnitser and G. Nikitaeva, "Resonance method of determining the damping characteristics of soils," Soil Mechanics and Foundation Engineering, vol. 45, no. 1, pp. 9-12, 2008.

[63]    C. W. Bert, "Material damping: An introductory review of mathematic measures and experimental technique," Journal of Sound and Vibration, vol. 29, no. 2, pp. 129-153, 1973.

[64]    H. Mevada and D. Patel, "Experimental determination of structural damping of different materials," Procedia Engineering, vol. 144, pp. 110-115, 2016.

[65]    H. Ogi, M. Fukunaga, M. Hirao, and H. Ledbetter, "Elastic constants, internal friction, and piezoelectric coefficient of $\alpha-$ TeO 2," Physical Review B, vol. 69, no. 2, p. 024104, 2004.

[66]    T. V. Roszhart, "The effect of thermoelastic internal friction on the Q of micromachined silicon resonators," in Solid-State Sensor and Actuator Workshop, 1990. 4th Technical Digest., IEEE, 1990, pp. 13-16: IEEE.

[67]    H. Qiu, A. Ababneh, D. Feili, X. Wu, and H. Seidel, "Analysis of intrinsic damping in vibrating piezoelectric microcantilevers," Microsystem Technologies, vol. 22, no. 8, pp. 2017-2025, 2016.

[68]    M. Barmatz and H. Chen, "Young's modulus and internal friction in metallic glass alloys from 1.5 to 300 K," Physical Review B, vol. 9, no. 10, p. 4073, 1974.

[69]    T. Ono and M. Norimoto, "Study on Young's modulus and internal friction of wood in relation to the evaluation of wood for musical instruments," Japanese journal of Applied physics, vol. 22, no. 4R, p. 611, 1983.

[70]    Z. Wang, L. Li, and M. Gong, "Measurement of dynamic modulus of elasticity and damping ratio of wood-based composites using the cantilever beam vibration technique," Construction and Building Materials, vol. 28, no. 1, pp. 831-834, 2012.

[71]    Y. Yu, J. Xi, E. Li, and J. F. Chicharo, "Measuring the linewidth enhancement factor of semiconductor lasers based on weak optical feedback effect," in Photonics Asia 2004, 2005, pp. 34-39: International Society for Optics and Photonics.

[72]    M. Wang and G. Lai, "Displacement measurement based on Fourier transform method with external laser cavity modulation," Review of Scientific Instruments, vol. 72, no. 8, pp. 3440-3445, 2001.

[73]    G. Giuliani, M. Norgia, S. Donati, and T. Bosch, "Laser diode self-mixing technique for sensing applications," Journal of Optics A: Pure and Applied Optics, vol. 4, no. 6, p. S283, 2002.

[74]    S. Donati, G. Giuliani, and S. Merlo, "Laser diode feedback interferometer for measurement of displacements without ambiguity," IEEE journal of quantum electronics, vol. 31, no. 1, pp. 113-119, 1995.

[75]    V. Srinivasan and R. Lumia, "A pseudo-interferometric laser range finder for robot

applications," IEEE Transactions on Robotics and Automation, vol. 5, no. 1, pp. 98-105, 1989.

[76]   S. Ottonelli, M. Dabbicco, F. De Lucia, M. Di Vietro, and G. Scamarcio, "Laser‑self‑mixing interferometry for mechatronics applications," Sensors, vol. 9, no. 5, pp. 3527-3548, 2009.

[77]   Z. Duan, Y. Yu, B. Gao, and C. Jiang, "Absolute distance measurement based on multiple self-mixing interferometry," Optics Communications, vol. 389, no. Supplement C, pp. 270-274, 2017/04/15/ 2017.

[78]   L. Scalise, Y. Yu, G. Giuliani, G. Plantier, and T. Bosch, "Self-mixing laser diode velocimetry: application to vibration and velocity measurement," IEEE Transactions on Instrumentation and Measurement, vol. 53, no. 1, pp. 223-232, 2004.

[79]   J. Perchoux, L. Campagnolo, Y. L. Lim, and A. D. Rakic, ""Lens-free" self-mixing sensor for velocity and vibrations measurements," in Optoelectronic and Microelectronic Materials and Devices (COMMAD), 2010 Conference on, 2010, pp. 43-44: IEEE.

[80]   Y. Zhao et al., "Self-mixing fiber ring laser velocimeter with orthogonal-beam incident system," IEEE Photonics Journal, vol. 6, no. 2, pp. 1-11, 2014.

[81]   T. Bosch, N. Servagent, and F. Boyer, "Vibrations measurements with a self-mixing type laser displacement sensor for modal analysis," in Instrumentation and Measurement Technology Conference, 1996. IMTC-96. Conference Proceedings. Quality Measurements: The Indispensable Bridge between Theory and Reality., IEEE, 1996, vol. 1, pp. 648-653: IEEE.

[82]   L. Scalise and N. Paone, "Laser Doppler vibrometry based on self-mixing effect," Optics and lasers in Engineering, vol. 38, no. 3, pp. 173-184, 2002.

[83]   L. L. H. Y. Y. Benli, "Cantilever Vibration Characteristics Based on Laser Self-Mixing Interference Effect [J]," Chinese Journal of Lasers, vol. 2, p. 034, 2012.

[84]   Y. Yu, J. Xi, and J. F. Chicharo, "Measuring the feedback parameter of a semiconductor laser with external optical feedback," Optics express, vol. 19, no. 10, pp. 9582-9593, 2011.

[85]   Y. Yu, J. Xi, J. F. Chicharo, and Y. Zhao, "A new approach for measuring the line-width enhancement factor," in Intelligent Sensors, Sensor Networks and Information Processing, 2008. ISSNIP 2008. International Conference on, 2008, pp. 471-474: IEEE.

[86]   Y. Fan, Y. Yu, J. Xi, G. Rajan, Q. Guo, and J. Tong, "Simple method for measuring the linewidth enhancement factor of semiconductor lasers," Applied optics, vol. 54, no. 34, pp. 10295-10298, 2015.

[87]   Y. Fan, Y. Yu, J. Xi, and J. F. Chicharo, "An estimation method for feedback level factor C of a self-mixing interferometry system," in Photonics Asia 2010, 2010, pp. 78530E-78530E-7: International Society for Optics and Photonics.

[88]   T. Taimre, M. Nikolić, K. Bertling, Y. L. Lim, T. Bosch, and A. D. Rakić, "Laser feedback interferometry: a tutorial on the self-mixing effect for coherent sensing," Advances in Optics and Photonics, vol. 7, no. 3, pp. 570-631, 2015.

[89]   S. Donati, "Photodetectors: devices, circuits, and applications," ed: IOP Publishing,

2001.

[90]     S. Donati, "Laser interferometry by induced modulation of cavity field," Journal of Applied Physics, vol. 49, no. 2, pp. 495-497, 1978.

[91]     N. Servagent, T. Bosch, and M. Lescure, "A laser displacement sensor using the self-mixing effect for modal analysis and defect detection," IEEE transactions on instrumentation and measurement, vol. 46, no. 4, pp. 847-850, 1997.

[92]     R. Ocaña and T. Molina, "Mapping a vibrating surface by using laser self-mixing interferometry," in Optical Micro-and Nanometrology V, 2014, vol. 9132, p. 913213: International Society for Optics and Photonics.

[93]     B. Liu, Y. Yu, J. Xi, Q. Guo, J. Tong, and R. A. Lewis, "Displacement sensing using the relaxation oscillation frequency of a laser diode with optical feedback," Applied optics, vol. 56, no. 24, pp. 6962-6966, 2017.

[94]     N. Servagent, F. Gouaux, and T. Bosch, "Measurements of displacement using the self-mixing interference in a laser diode Mesures de déplacements basées sur le phénomène de self-mixing dans une diode laser," Journal of optics, vol. 29, no. 3, p. 168, 1998.

[95]     Y. Yu, Y. Fan, and B. Liu, "Self-mixing interferometry and its applications," 2016, vol. 10021, pp. 100210U-100210U-13.

[96]     S. B. Coşkun, B. Öztürk, and M. T. Atay, Transverse vibration analysis of euler-bernoulli beams using analytical approximate techniques. INTECH Open Access Publisher, 2011.

[97]     S. Spinner, T. Reichard, and W. Tefft, "A comparison of experimental and theoretical relations between Young's modulus and the flexural and longitudinal resonance frequencies of uniform bars," J. Res. Natl. Bur. Stand., Sect. A, vol. 64, pp. 147-155, 1960.

[98]     A. Standard, "Standard Test Method for Dynamic Young's Modulus, Shear Modulus, and Poisson's Ratio for Advanced Ceramics by Impulse Excitation of Vibration," 2001.

[99]     K. Petermann, Laser diode modulation and noise. Springer Science & Business Media, 2012.

[100]    S. Donati, "Developing self‐mixing interferometry for instrumentation and measurements," Laser & Photonics Reviews, vol. 6, no. 3, pp. 393-417, 2012.

[101]    J. Mork, B. Tromborg, and J. Mark, "Chaos in semiconductor lasers with optical feedback: Theory and experiment," IEEE Journal of Quantum Electronics, vol. 28, no. 1, pp. 93-108, 1992.

[102]    R. Lang and K. Kobayashi, "External optical feedback effects on semiconductor injection laser properties," IEEE journal of Quantum Electronics, vol. 16, no. 3, pp. 347-355, 1980.

[103]    G. Plantier, C. Bes, and T. Bosch, "Behavioral model of a self-mixing laser diode sensor," IEEE Journal of Quantum Electronics, vol. 41, no. 9, pp. 1157-1167, 2005.

[104]    G. Mourat, N. Servagent, and T. Bosch, "Optical feedback effects on the spectral linewidth of semiconductor laser sensors using self-mixing interference," IEEE journal of quantum electronics, vol. 34, no. 9, pp. 1717-1721, 1998.

[105]    Y. Yu, J. Xi, J. F. Chicharo, and T. M. Bosch, "Optical Feedback Self-Mixing

Interferometry With a Large Feedback Factor $ C $: Behavior Studies," IEEE Journal of Quantum Electronics, vol. 45, no. 7, pp. 840-848, 2009.

[106]   Y. Fan, Y. Yu, J. Xi, and J. F. Chicharo, "Improving the measurement performance for a self-mixing interferometry-based displacement sensing system," Applied Optics, vol. 50, no. 26, pp. 5064-5072, 2011.

[107]   T. Bosch, "An overview of self-mixing sensing applications," in Optoelectronic and Microelectronic Materials and Devices, 2004 Conference on, 2004, pp. 385-392: IEEE.

[108]   R. M. Digilov and H. Abramovich, "Flexural vibration test of a beam elastically restrained at one end: a new approach for Young's modulus determination," Advances in Materials Science and Engineering, vol. 2013, 2013.

[109]   S. Mallat, A wavelet tour of signal processing: the sparse way. Academic press, 2008.

[110]   O. Rioul and M. Vetterli, "Wavelets and signal processing," IEEE signal processing magazine, vol. 8, no. 4, pp. 14-38, 1991.

[111]   M. Alfaouri and K. Daqrouq, "ECG signal denoising by wavelet transform thresholding," American Journal of applied sciences, vol. 5, no. 3, pp. 276-281, 2008.

[112]   S. Santoso, E. J. Powers, and W. Grady, "Power quality disturbance data compression using wavelet transform methods," IEEE Transactions on Power Delivery, vol. 12, no. 3, pp. 1250-1257, 1997.

[113]   A. S. Lewis and G. Knowles, "Image compression using the 2-D wavelet transform," IEEE Transactions on image Processing, vol. 1, no. 2, pp. 244-250, 1992.

[114]   H. P. Robertson, "The uncertainty principle," Physical Review, vol. 34, no. 1, p. 163, 1929.

[115]   R. Ganesan, T. K. Das, and V. Venkataraman, "Wavelet-based multiscale statistical process monitoring: A literature review," IIE transactions, vol. 36, no. 9, pp. 787-806, 2004.

[116]   W. K. Ngui, M. S. Leong, L. M. Hee, and A. M. Abdelrhman, "Wavelet analysis: Mother wavelet selection methods," in Applied mechanics and materials, 2013, vol. 393, pp. 953-958: Trans Tech Publ.

[117]   D. S. G. Pollock, "Dyadic Wavelets Analysis."

[118]   P. Goupillaud, A. Grossmann, and J. Morlet, "Cycle-octave and related transforms in seismic signal analysis," Geoexploration, vol. 23, no. 1, pp. 85-102, 1984.

[119]   M. Chen, Y. Zhang, C. Chen, L. Wang, and W. Huang, "Damping microvibration measurement using laser diode self-mixing interference," IEEE Photonics Journal, vol. 6, no. 3, pp. 1-8, 2014.

[120]   Thorlabs. https://www.thorlabs.com/index.cfm.

[121]   Y. Fan, Y. Yu, J. Xi, and Q. Guo, "Dynamic stability analysis for a self-mixing interferometry system," Optics express, vol. 22, no. 23, pp. 29260-29269, 2014.